I
I
I
I
I
T

403 146

Vidya Technical Report No. 63-95
January 9, 1963

THEORETICAL INVESTIGATION OF DYNAMIC STABILITY DERIVATIVES OF DUCTED PROPELLERS

by
A. R. Kriebel
A. H. Sacks
J. N. Nielsen

Prepared Under Navy, Bureau of Naval Weapons
Contract NOw 62-0129-c

Vidya Project No. 167/C

CATALOGED BY ASTIA
AS AD No. ____

ASTIA

MAY 6 1963

TISIA D

RESEARCH DEVELOPMENT
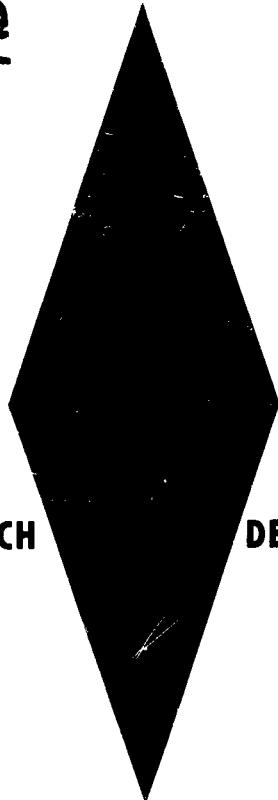
A DIVISION OF Itek CORPORATION

Qualified requesters may obtain copies of this report direct from ASTIA

व **VIDYA**

The word Vidya, taken from the Vedanta philosophy of the Hindus,
means knowledge. The symbol used to denote the Vidya organization
is the letter "V" from Sanskrit, the ancient language of India.
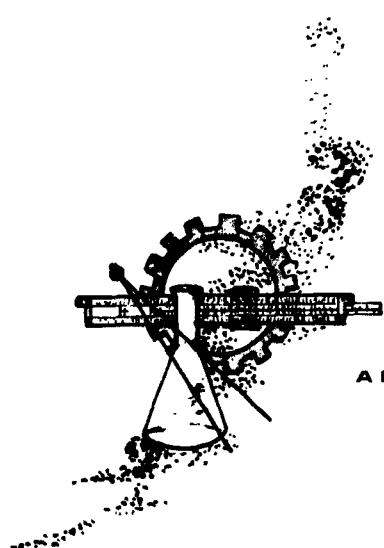
APPLIED MECHANICS....PHYSICS....ANALYSES

THEORETICAL INVESTIGATION OF DYNAMIC STABILITY
DERIVATIVES OF DUCTED PROPELLERS

by

A. R. Kriebel

A. H. Sacks

J. N. Nielsen
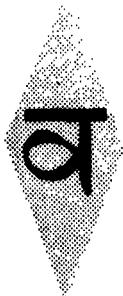
V I D Y A

A DIVISION OF Itek CORPORATION

SUMMARY

The static and dynamic stability derivatives of a ducted pro-
peller are predicted by theoretical analysis. The analysis is based
on the theory presented in Reference 1, and the ducted propeller is
initially represented by a short, straight, thin ring surrounding a
uniformly loaded actuator disk. Then the interference effect of the
ring duct on an actual propeller with finite number of blades is
calculated in order to determine the contribution of the propeller
to the stability derivatives of the ducted propeller.

The analysis is applied to the case of a torpedo-like config-
uration consisting of a body of revolution with a rear-mounted ducted
propeller in axial flow. The natural frequency and damping of the
configuration is calculated, and the individual contributions of
the duct, the propeller, the hull, and a fin (added for static sta-
bility) are determined. It is found that the ducted propeller is
a more effective oscillation damper than is a fin of the same pro-
jected area and that the effectiveness increases with propeller disk
loading. The contribution of the ducted propeller to the dynamic
stability of the torpedo is found to be dominated by the static sta-
bility derivative C_{N_α} of the isolated ducted propeller.

The theory for the ducted propeller is compared with available
experimental data in hovering, steady axial flow, and steady flow
at angle of attack. It is found that the important derivative C_{N_α}
is predicted well for small angles of attack by the present theory.

The division of thrust between duct and propeller is predicted moderately well for ducts of small chord/diameter ratios with no flow separation. Experimental data suitable for comparison with experiment are extremely sparse since flow separation is generally present at the duct leading edge.

A method for reducing ducted propeller data is presented and shown to give better agreement with theory than conventional methods. A qualitative analysis of real slipstream effects is presented, and an experimental program is outlined for obtaining some badly needed data on ducted propellers without leading-edge flow separation.

TABLE OF CONTENTS

v

a   distance from hull nose to hull center of pressure (Fig. 5)

A   disk area of actuator disk or propeller, $(\pi/4)D^2$

b   propeller blade chord

B   number of propeller blades

c   chord of duct

C   stability derivative defined in Section 2,

$$e.g., \quad C_{m_\alpha} = \frac{\partial C_m}{\partial \alpha} , \quad C_{m_q} = \frac{\partial C_m}{\partial (Dq/V_o)} , \quad m_{\dot{\alpha}} = \frac{\partial C_m}{\partial (D\dot{\alpha}/V_o)}$$

(all stability derivatives are evaluated at $q = \dot{\alpha} = 0$)

c_{l_α} lift curve slope of a propeller blade section, per radian

C_m pitching moment coefficient, $2M/DAq_o$

C_N normal force coefficient, N/Aq_o

$(c_{n*})_P$ propeller yawing moment coefficient, $2N_P^*/DAq_o$

C_T thrust coefficient, T/Aq_o

$(c_Y)_P$ propeller side force coefficient, Y_P/Aq_o

D   diameter of duct or propeller

E   complete elliptic integral of second kind,

$$\int_0^{\pi/2} \sqrt{1 - k^2 \sin^2 \chi} \, d\chi$$

F   complex potential function, $F(z) = \Phi + i\psi = F'(\zeta)$, Equation (A.17)

h   camber (Sketch A.7, p. A-26)

i	$\sqrt{-1}$
Im	imaginary part
K	complete elliptic integral of first kind, $$\int_{0}^{\pi/2} \frac{d\chi}{\sqrt{1 - k^2 \sin^2 \chi}}$$
$K_y{}', K_y{}''$	radius of gyration of hull about pitching axis through hull centroid and through hull center of gravity, respectively
L	length of hull (Fig. 4)
M_h	figure of merit for hovering flight, $\dfrac{T_{(DP)_h}}{P} \sqrt{\dfrac{T_{(DP)_h}}{2\rho A}}$
m_H	mass of hull
$M_{(\ )}$	aerodynamic pitching moment (positive clockwise in Fig. 1) about: midchord diameter of duct for M_D, propeller diameter for M_P, and centroid of hull for M_H
$M'_{(\ )}$	pitching moment about hull centroid due to subscripted configuration component
$M''_{(\ )}$	pitching moment about vehicle center of gravity due to subscripted configuration component
n	propeller rotational speed, revolutions per second
N_P^*	yawing moment on isolated propeller
$N_{(\ )}$	normal force on subscripted configuration component (Fig. 1)
$N'_{(\ )}$	normal force on subscripted component for pitching about the hull centroid
$N''_{(\ )}$	normal force on subscripted component for pitching about the vehicle center of gravity
p	static pressure
P	propeller power, $\tau\omega$

q	pitching rate, rad/sec (Fig. 2)
q_o	free-stream dynamic pressure $(1/2)\rho V_o^2$
r	radial coordinate (Fig. 1)
R	$D/2$
R_a	equivalent arm radius in pure pitch $= V_o/q$ (Fig. 2)
Re	length Reynolds number for the hull
r_H	local hull radius (Fig. 5)
r_j	radial coordinate in jet cross section (Fig. 6)
r_L	hull base radius
r_m	maximum hull radius (Fig. 5)
t	time, sec
$T_{(\ )}$	thrust (or axial) component of force on subscripted configuration component (Fig. 1)
u_{F_s}, v_{F_s}	x_s, y velocity components induced by complex potential F at duct surface (Sketch A.1, p. A-3)
u_{h_s}, v_{h_s}	axial and radial velocity components induced at duct surface by a vortex ring of constant strength (Sketch A.2, p. A-12)
u_α, v_α	axial and radial velocity components induced by a vortex ring of variable strength Γ_α (Sketch A.4, p. A-19)
u_γ, v_γ	axial and radial velocity components induced by γ (or actuator disk) (Sketch A.1)
$u_{\gamma_h}, u_{\gamma_\alpha}, u_{\gamma_q}$	axial velocity components induced by duct bound vorticity components γ_h, γ_α, and γ_q, Equations (42), (50), and (57), respectively
V	instantaneous value of free-stream velocity (Fig. 1)
V_j	jet velocity far downstream in propeller slipstream (Fig. 1)

ix

V_o	mean free-stream velocity (Fig. 1)
Vol	volume of hull
Vol*	volume of hull including its boundary-layer displacement thickness
V_s	local swirl velocity component generated by propeller (Fig. 6)
v_{w_s}	radial velocity component induced by duct wake at duct surface (Sketch A.3, p. A-16)
W	relative local fluid velocity on duct surface (Fig. 2) and Equation (7)
w_{F_s}, w_{γ_s}	duct surface velocity components due to F and γ, respectively (Section A.1.3)
w_h, w_α, w_q	component of velocity W on duct surface due to actuator disk, angle of attack of free stream, and pitching motion of duct, respectively (Fig. 2)
$w_{h_i}, w_{\alpha_i}, w_{q_i}$	component of velocity W on duct surface self induced by bound vorticity γ_h, γ_α, and γ_q, respectively (Fig. 2)
W_j	mass flow rate through duct
$w_{q_1}, w_{q_2}, w_{q_3}$	components of w_q due to duct rotation, translation, and wake, respectively
$\bar{w}_{(\ )_i}$	value of $w_{(\ )_i}$ averaged over duct chord
X	hull drag force
x_c, y_c	orthogonal coordinates of cambered plate (Sketch A.7, p. A-26)
x_f, y_f	orthogonal coordinates for flat plate (Sketch A.6, p. A-24)
x_H	axial distance ahead of hull centroid (Fig. 5)
x_s, y	axial and radially inward coordinates, $y = R - r$ (Fig. 1)
Y_p	side force on isolated propeller

z	radius vector in physical plane, $x_s + iy$ (Fig. 1(b))
α	instantaneous angle of attack, rad (Fig. 1(a))
α_j	angle of final slipstream or jet relative to duct axis, rad (Fig. 6)
α_o	mean free-stream angle of attack, rad (Fig. 1(a))
β	propeller blade pitch angle (between blade chord and plane of rotation)
γ	vorticity shed by actuator disk (Fig. 1(a))
$\gamma_\gamma, \gamma_\alpha, \gamma_q$	components of bound vorticity on duct due to actuator disk, angle of attack of free stream, and pitching motion of duct, respectively (Fig. 2)
Γ_k	a constant ($\Gamma_\alpha/\cos\phi$) given by Equation (A.64)
$d\Gamma_w$	trailing vortex filament in duct wake (Fig. 2)
$\Gamma_\gamma, \Gamma_\alpha, \Gamma_q$	components of circulation about duct chord, positive in the same sense as $\gamma_{(\ )}$ in Figure 2, $$\Gamma_{(\ )} = \int_{-c/2}^{+c/2} \gamma_{(\ )}\, dx_s$$
$\delta*$	displacement thickness of hull boundary layer
Δp	increase in static and total pressure across actuator disk, $T_{P(D)}/A$
ϵ	duct thickness
ζ	radius vector in circle plane (Fig. 1(b)) and Equation (A.13)
ζ_1	ratio of damping to critical damping
η_h	hovering or compressor efficiency (Eq. (196))
η_p	propulsive efficiency (Eq. (183))
θ	angle in circle plane (Fig. 1(b)), or momentum thickness of hull boundary layer

λ	propeller advance ratio $V_0/\omega D$, V_0/nD, or $V_0/\omega R$ (depending upon reference cited)
ν	frequency of plunging motion, rad/sec
ξ_R	axial distance from ring vortex (Sketch A.2, p. A-12)
ξ_t	axial distance from trailing edge of duct (Sketch A.1, p. A-3)
ρ	fluid density, slug/ft^3
σ	propeller solidity at three-quarter radius, $4Bb/3\pi D$
τ	propeller torque
ϕ	circumferential duct coordinate (Fig. 1)
Φ	velocity potential
χ	argument of elliptic integral, $\dfrac{\phi - \phi' + \pi}{2}$
ψ	stream function
ω	propeller rotational speed, rad/sec
ω_n	natural frequency of flight oscillations, rad/sec
$\lvert\ \rvert$	absolute value

Subscripts

a	axial component
c	cambered plate
D	isolated duct
DP	ducted propeller, D(P) + P(D)
D(P)	duct in the presence of the propeller (represented by an actuator disk)
D(P)→H	interference of ducted propeller on hull
D→P	interference of duct on propeller

xii

f	flat plate
F	isolated fin
h	for hovering flight condition
H	isolated hull
$H \rightarrow D(P)$	interference of hull on ducted propeller
j	jet or propeller slipstream far downstream
L	at base of hull
N	component of moment due to N
o	far upstream
P	isolated propeller
P(D)	propeller in the presence of the duct
q	due to pitching motion
r	radial component
s	at the duct surface
t	at the duct trailing edge
T	component of moment due to T
w	due to duct wake
α	due to angle of attack of free stream
$\dot{\alpha}$	due to plunging motion
γ	due to actuator disk

Superscripts

( )'	in the circle (ζ) plane, or running variable
$\bar{}$	average value as defined for each case
$\dot{}$	time derivative of ( )

Note: The α, $\dot{\alpha}$, and q subscripts denote partial differentiation only when used with stability derivatives (see Section 2).

1. INTRODUCTION

The benefits to be gained by ducting or shrouding a propeller for static operation and low-speed flight were demonstrated in 1931 by the experiments of Stipa in Italy. Since that time, and particularly in recent years when hovering flight and vertical take-off became feasible for conventional aircraft, ducted propellers have received considerable attention from numerous investigators. A vast number of individual experimental programs have been undertaken, as reviewed in Reference 2, and a number of VTOL (vertical take-off and landing) vehicles were designed and built employing ducted propellers.

Because of its complexity, however, the theory of the ducted propeller has lagged far behind experiment. Only now is a rigorous self-consistent theory emerging, even for predicting the aerodynamic forces and moments on ducted propellers in steady axial flow. This theory (Refs. 3 and 4) is based on the classical method of singularities in three dimensions and is thus far restricted to small angles of attack and light propeller loadings (i.e., small perturbations). However, an approximate theory for all angles of attack has been developed by Burggraf in Reference 1 in which the ducted propeller is represented by a short, thin, straight duct surrounding a uniformly loaded actuator disk. This representation permits the assumption of nearly two-dimensional flow over each chordwise strip of the duct.

As for dynamic stability derivatives, the situation is far worse. At this time, there appear to be neither experimental data

nor any theoretical analysis for the dynamic stability derivatives of an isolated ducted propeller.

The purpose of the present investigation is to provide a theoretical analysis for predicting the forces, moments, and stability derivatives of an isolated ducted propeller for hovering and for forward flight at all angles of attack. In order to accomplish this end, we shall first introduce the assumptions made by Burggraf in Reference 1. We shall then extend his analysis to cover the cases of pitching and plunging flight, and, finally, we shall generalize the analysis to include the interference effect of the duct on a propeller with finite number of blades. In the course of the analysis, we shall investigate the approximations made in Reference 1, particularly the averaging processes used in calculating certain induced velocities, and we shall investigate the effect of altering the propeller location within the duct.

The theory developed for the ducted propeller will be applied herein to a torpedo-like configuration in order to investigate its dynamic stability and to get some insight into the effectiveness of the ducted propeller as a stabilizer and oscillation damper. For this problem, the thrust interference between the hull and the ducted propeller will also be investigated by approximate methods.

In addition to the basic analysis, a qualitative analysis of real slipstream effects will be presented, and the latter will be used in developing a rational method for comparison of theoretical and experimental results.

2. APPROACH TO THE DUCTED-PROPELLER ANALYSIS

The primary objective of this study is the prediction of the stability derivatives of a ducted propeller without restriction on either angle of attack or propeller disk loading. This is done by finding the duct derivatives in the presence of the propeller first and then the propeller derivatives in the presence of the duct.

2.1 The Duct in the Presence of the Propeller

The aerodynamic forces and moments on the duct in the presence of the propeller are found by representing the propeller as a uniformly loaded actuator disk. The net duct reaction is expressed as a thrust force $T_{D(P)}$, a normal force $N_{D(P)}$, and a pitching moment about the midchord diameter $M_{D(P)}$ as shown in Figure 1.

For a given set of design variables c/D and γ/V_o (or $C_{T_{P(D)}}$, these three components can be written as dimensionless coefficients in terms of the flight conditions as follows:

$$\frac{N_{D(P)}}{Aq_o} = \left(C_N\right)_{D(P)} \left(\alpha_o, \frac{Dq}{V_o}, \frac{D\dot{\alpha}}{V_o}\right) \tag{1}$$

$$\frac{T_{D(P)}}{Aq_o} = \left(C_T\right)_{D(P)} \left(\alpha_o, \frac{Dq}{V_o}, \frac{D\dot{\alpha}}{V_o}\right) \tag{2}$$

$$\frac{2M_{D(P)}}{DAq_o} = \left(C_m\right)_{D(P)} \left(\alpha_o, \frac{Dq}{V_o}, \frac{D\dot{\alpha}}{V_o}\right) \tag{3}$$

Thus there are nine stability derivatives (with respect to α_o, q, and $\dot{\alpha}$) for the duct in the presence of the propeller, since V_o is assumed constant. The way in which these are defined will be

illustrated now for the three moment derivatives. But since α is not restricted to small values, an α coefficient will be used rather than an α derivative. Thus, partial differentiation of $(C_m)_{D(P)}$ with V_o constant and $\alpha = \alpha_o = $ constant[1], and then setting $q = \dot{\alpha} = 0$, gives the q and $\dot{\alpha}$ stability derivatives:

$$\left. \frac{\partial \left(C_m\right)_{D(P)}}{\partial \left(\frac{Dq}{V_o}\right)} \right|_{V_o,\alpha_o,q=\dot{\alpha}=0} = \left(C_{m_q}\right)_{D(P)}\left(\frac{c}{D}, C_{T_{P(D)}}, \alpha_o\right) \quad (4)$$

$$\left. \frac{\partial \left(C_m\right)_{D(P)}}{\partial \left(\frac{D\dot{\alpha}}{V_o}\right)} \right|_{V_o,\alpha_o,q=\dot{\alpha}=0} = \left(C_{m_{\dot{\alpha}}}\right)_{D(P)}\left(\frac{c}{D}, C_{T_{\bar{P}(D)}}, \alpha_o\right) \quad (5)$$

Hence, for small rates of pitching q and plunging $\dot{\alpha}$, the instantaneous duct moment is given by

$$C_{m_{D(P)}} = C_{m_{D(P)}}(\alpha_o,0,0) + \left(\frac{Dq}{V_o}\right)\left(C_{m_q}\right)_{D(P)} + \left(\frac{D\dot{\alpha}}{V_o}\right)\left(C_{m_{\dot{\alpha}}}\right)_{D(P)} \quad (6)$$

The first term is the static moment coefficient. The static coefficient and the q derivative are found in the present analysis by considering the ducted propeller in the pure pitch flight condition, and the $\dot{\alpha}$ derivative is estimated independently by use of the apparent mass concept. For pure pitch, the ducted actuator disk moves as though it were mounted rigidly to an arm with fixed radius R_a as shown in Figure 2. The arm rotates at constant

---

[1]Note that α differs from α_o only for plunging flight (See Fig. 1)

angular velocity q. Both α_o and V_o are constant and $V_o = qR_a$. The method of singularities is used to find the velocity distribution W over the duct surface as induced by all of the bound and shed vorticity for the ducted actuator disk shown in Figure 2. The moment coefficient for this motion

$$\left(C_m\right)_{D(P)} \left(\alpha_o, \frac{Dq}{V_o}, 0\right)$$

is then found by integration of the static pressure $(p_o + \frac{\rho}{2} V_o{}^2 - \frac{\rho}{2} W^2)$ over the duct surface. Then by setting $q = 0$ (but holding V_o constant), one obtains $(C_m)_{D(P)} (\alpha_o, 0, 0)$. By differentiating $(C_m)_{D(P)}$ with respect to q as described above, one obtains $\left(C_{m_q}\right)_{D(P)}$.

The total surface velocity distribution W on the duct during pure pitch is considered to be composed of six parts as shown in Figure 2. That is,

$$W = w_h + w_\alpha + w_q + w_{h_i} + w_{\alpha_i} + w_{q_i} \tag{7}$$

The first component w_h is induced by the actuator disk for no motion of the duct (i.e., for hovering flight). The second two components are due to the two components of the duct motion: a translational motion V_o at α_o, which produces w_α, and a rotational q about the midchord duct diameter which produces w_q. The w_α and w_q components include the velocity induced by the duct wake which is generated in each case.

It is assumed that the propeller thrust coefficient $C_{T_{P(D)}}$ is sufficiently large to produce a large jet velocity V_j compared with the lateral component of flight speed. That is,

$$V_j \gg V_o \sin \alpha_o \qquad (8)$$

In this case, the jet extends downstream nearly aligned with the duct axis as shown in Figure 2 for any combination of the duct motions. Furthermore, the duct motions, their vorticity distributions, and the reactions which they produce on the duct are all additive (See Eq. 6). The propeller vorticity γ and the duct wake vortex filaments $d\Gamma_w$ both lie on the cylindrical surface $r = D/2$ and are mutually perpendicular (Fig. 2).

The duct wake vortex filaments produce a counter rotating swirl distribution (Fig. 6). There is no swirl generated directly by the propeller in the present analysis since it is represented by an ideal actuator disk. However, the effect of real propeller slipstream effects, including swirl, is considered qualitatively in Section 4.2.2.

The bound vorticity distributions on the duct corresponding to hovering, angle of attack, and pitching, are composed of γ_h, γ_α, and γ_q, which are calculated with the assumption of two-dimensional flow over local chordwise strips of the duct for $c \ll D$. But since the vorticity is actually distributed on a ring rather than a flat plate, there are three additional self-induced axial velocity components w_{h_i}, w_{α_i}, and w_{q_i}. These are analogous to the

self-induced axial velocity (or propagation speed) of a ring vortex. Since the self-induced radial velocity distribution is small for $\infty > D \gg c$, it is neglected. In order to make the analysis tractable, it is found necessary to approximate the three self-induced components since it is not feasible to express them analytically (See Appendix D) and to incorporate them into the subsequent analysis. The approximation cannot be made by simply concentrating the bound vorticity on the duct into a single ring filament of strength $\Gamma_h + \Gamma_\alpha + \Gamma_q$ since such a ring induces an infinitely large axial velocity upon itself. The method employed here and in Reference 1 is to: (1) average the bound vorticity over the duct chord, (2) find the self-induced velocity distribution due to the averaged vorticity, and (3) then average the self-induced velocity over the duct chord and use these values, $\bar{w}_{h_i}$, $\bar{w}_{\alpha_i}$, and $\bar{w}_{q_i}$, in the subsequent analysis. The accuracy of this averaging process is assessed in Appendix D.

2.2 The Propeller in the Presence of the Duct

The stability derivatives for the isolated propeller are defined just as for the duct for the three components of the net aerodynamic force T_p, N_p, Y_p, and for the two components of the moment M_p and N^*_p which are about propeller diameters. The interference of the duct on the propeller due to α and q is found to produce only pitching moments $M_{(D \to P)\alpha}$ and $M_{(D \to P)q}$. The thrust interference $T_{D \to P}$ produced by the duct in steady axial flight (i.e., for $\alpha_o = 0$) is not predicted here since it is

considered to be part of the initial design process. Thus in the presence of the duct each component of the propeller reaction $(\ )_{P(D)}$ is the same as for the isolated propeller $(\ )_P$ except for the pitching moment which is given by $M_{P(D)} = M_P + M_{D \rightarrow P}$.

The α and q derivatives are obtained from Reference 5 for the isolated propeller at small α_o. The $\dot{\alpha}$ derivative and the duct interference will be estimated in the present analysis. Although the propeller thrust is generally greater than the duct thrust, the flight-induced forces and moments on the propeller in the presence of the duct are found to be small compared with those for the duct for typical conditions except for $M_{(D \rightarrow P)_q}$. Therefore, a more refined analysis of the propeller reactions does not appear to be warranted except possibly for the duct interference moment on the propeller due to pitch, $M_{(D \rightarrow P)_q}$. This moment may be appreciable for isolated ducted propellers, such as in VTOL applications, but even it is negligible when the ducted propeller is combined with a long hull, as for a torpedo.

3. ANALYSIS

3.1 Stability Derivatives of a Duct in the Presence of an Actuator Disk

3.1.1 Discussion

The purpose here is to determine the force and moment coefficients and the stability derivatives of a thin duct of uniform diameter with an actuator disk located in the exit plane (Fig. 1(a)) as in Reference 1. (The results are actually valid for any actuator disk location within the duct as shown in Appendix C.) The coefficients and derivatives here pertain to the aerodynamic force and moment acting on the duct in the presence of the actuator disk.

The initial assumptions are:

(a) The fluid is inviscid and incompressible, and a velocity potential represents the actual flow field in which the boundary layers are negligibly thin and unseparated.

(b) The chord-to-diameter ratio of the duct c/D is small enough so that the flow over each chordwise strip is nearly two dimensional.

(c) The lateral component of flight speed is much smaller than the slipstream (or jet) velocity; that is, $V_j \gg V_o \sin \alpha_o$ in Figure 2. In this case the slipstream extends nearly axially downstream as shown.

(d) The propeller is represented by an ideal actuator disk which produces a uniform loading or pressure rise Δp over the disk but no swirl.

(e) The diameter of the slipstream is considered constant and equal to the duct diameter for the purpose of calculating the

duct surface velocity W. This assumption is discussed on page 130 of Reference 6 and in Section 4.2.1.

With the above assumptions, the method of singularities is used in Appendix A to determine the duct surface velocity distribution W for the pure-pitch flight condition (Fig. 2). The pressure distribution corresponding to W is integrated over the duct surface to obtain the net force and moment on the duct in Appendix B. In the present section, we shall find the resulting force and moment coefficients for the duct in the presence of the actuator disk both in steady flight at angle of attack and in hovering. Then we shall find the pitching (q) stability derivatives and finally the plunging ($\dot{\alpha}$) derivatives.

3.1.2 Static (α) coefficients

Let us find the static (α) coefficients of the duct by the procedure in Section 2, from the results in Appendix B. These coefficients give the net aerodynamic reaction on the duct when $q = \dot{\alpha} = 0$, that is, for steady flow at angle of attack α_o.

There is a normal force $N_{D(P)}$ and a pitching moment $\left(M_N\right)_{D(P)}$ which are associated with the nonsingular portion of the pressure distribution, that is, excluding leading-edge suction. The latter, in turn, gives rise to a thrust force $T_{D(P)}$ and a pitching moment $\left(M_T\right)_{D(P)}$. We shall now consider these four components in succession.

The general expression for

$$\left(C_N\right)_{D(P)} \left(\alpha_o, \frac{Dq}{V_o}, 0\right)$$

corresponding to Equation (1) is given by Equation (B.33) of Appendix B. When $q = 0$, we obtain Equation (B.36). By substituting Equations (A.53) and (A.77) for $\overline{w}_{h_i}$ and $\overline{w}_{\alpha_i}$ and by dropping terms higher than second order in c/D, we find the static coefficient

$$\left(C_N\right)_{D(P)}(\alpha_o,0,0) = \frac{\frac{c}{D}\sin\alpha_o}{1 + \frac{\pi c}{2D}}\left\{4\pi\cos\alpha_o + \frac{\gamma}{V_o}\left[\pi \right.\right.$$
$$\left.\left. + \frac{c}{D}\left(\ln\frac{16D}{c} - 1\right)\left(2\ln\frac{4D}{c} - \frac{5}{2}\right) + \frac{c}{4D}\right]\right\} \quad (9)$$

For the special case of a ring wing at small angle of attack (i.e., for $\gamma = 0$ and $\alpha_o \ll 1$), this result reduces to that of Reference 7.

The general expression for $\left(M_N\right)_{D(P)}$ is given by Equation (B.35) and when $q = 0$ by Equation (B.37). Substituting Equations (A.53) and (A.77) for $\overline{w}_{h_i}$ and $\overline{w}_{\alpha_i}$ and then retaining only the lowest order terms in c/D, we find

$$\left(C_{m_N}\right)_{D(P)}(\alpha_o,0,0) = \frac{c^2}{D^2}\left(\frac{\pi\gamma}{2V_o} + 2\pi\cos\alpha_o\right)\sin\alpha_o \quad (10)$$

The duct thrust $T_{D(P)}$ is expressed by Equation (B.41), and when $q = 0$ we obtain the thrust coefficient

$$\left(C_T\right)_{D(P)}(\alpha_o,0,0) = \frac{\gamma^2}{V_o^2}\left(\frac{2c}{\pi D}\right)\left(\ln\frac{16D}{c} - 2\right)^2 + 4\pi\frac{c}{D}\left(\frac{\sin\alpha_o}{1 + \frac{\pi c}{2D}}\right)^2 \quad (11)$$

The expression for $\left(M_T\right)_{D(P)}$ is given in Equation (B.42), and when $q = 0$, we find

$$\left(C_{m_T}\right)_{D(P)} (\alpha_0, 0, 0) = \frac{4c\gamma/DV_0}{1 + \frac{\pi c}{2D}} \left(\ln \frac{16D}{c} - 2\right) \sin \alpha_0 \qquad (12)$$

Thus, except for the case of very low disk loading $(\gamma/V_0 \to 0)$, we find that C_{m_N} in Equation (10) is much smaller (higher order in c/D) than C_{m_T} in Equation (12). Therefore, we shall take the total pitching moment on the duct to be equal to the component arising from leading-edge suction, so that

$$\left(C_m\right)_{D(P)} (\alpha_0, 0, 0) = \left(C_{m_T}\right)_{D(P)} (\alpha_0, 0, 0) = \frac{4 \frac{c}{D} \frac{\gamma}{V_0}}{1 + \frac{\pi c}{2D}} \left(\ln \frac{16D}{c} - 2\right) \sin \alpha_0$$

$$(13)$$

3.1.3 Thrust ratio in hovering flight

For hovering flight, the duct thrust is given by Equation (B.41) with $V_0 = 0$. That is,

$$T_{D(P)_h} = \frac{cD}{2} \frac{\rho\gamma^2}{2} \left(\ln \frac{16D}{c} - 2\right)^2 \qquad (14)$$

Also, for hovering flight, application of Bernoulli's equation far ahead and far behind the propeller disk gives

$$\gamma = V_j = \sqrt{2\Delta p/\rho} \qquad (15)$$

Thus, the actuator-disk loading is given by

$$\frac{T_{P(D)_h}}{A} = \Delta p = \frac{\rho \gamma^2}{2} \tag{16}$$

and we find that the thrust ratio for hovering flight is therefore

$$\frac{T_{D(P)_h}}{T_{P(D)_h}} = \frac{2c}{\pi D} \left(\ln \frac{16D}{c} - 2 \right)^2 \tag{17}$$

3.1.4 Pitching (q) derivatives

We shall now find the q derivatives of the duct by using the procedure of Section 2 with the results of Appendix B. Again, we shall consider in succession the q stability derivatives of each of the four duct reaction components

$$N_{D(P)}, \quad \left(M_N\right)_{D(P)}, \quad T_{D(P)}, \quad \text{and} \quad \left(M_T\right)_{D(P)}$$

Thus, by differentiating Equation (B.33) with respect to Dq/V_o, holding α_o and V_o constant, we obtain Equation (B.38) for $\left(C_{N_q}\right)_{D(P)}$. But if only the two lowest order terms in c/D are retained, Equation (B.38) reduces to

$$\left(C_{N_q}\right)_{D(P)} = \frac{\gamma c}{V_o D} \left(\ln \frac{16D}{c} - 1 \right) + \frac{\pi c^2}{D^2} \cos \alpha_o \tag{18}$$

By the same procedure, Equation (B.35) gives (B.39) and we get

$$\left(C_{m_{N_q}}\right)_{D(P)} = \frac{\gamma c^2}{2 V_o D^2} \left(\ln \frac{16D}{c} - \frac{5}{2} \right) \tag{19}$$

Similarly, if Equation (B.41) is differentiated with respect to Dq/V_o holding α_o and V_o constant, and if q is then set equal to zero, we obtain

$$\left(C_{T_q}\right)_{D(P)} = -\frac{\pi^2 c^3 \sin \alpha_o}{D^3 \left(1 + \frac{\pi c}{2D}\right)^2} \qquad (20)$$

Differentiating Equation (B.42) in the same way gives

$$\left(C_{m_{T_q}}\right)_{D(P)} = -\frac{\pi \gamma c^3 \left(\ln \frac{16D}{c} - 2\right)}{2V_o D^3 \left(1 + \frac{\pi c}{2D}\right)} \qquad (21)$$

Now, since $\left(C_{m_{T_q}}\right)_{D(P)}$ is of higher order in c/D than $\left(C_{m_{N_q}}\right)_{D(P)}$, retention of terms only through second order in c/D gives for the q derivative of the pitching moment

$$\left(C_{m_q}\right)_{D(P)} = \left(C_{m_{N_q}}\right)_{D(P)} = \frac{\gamma c^2}{2V_o D^2} \left(\ln \frac{16D}{c} - \frac{5}{2}\right) \qquad (22)$$

3.1.5 Plunging ($\dot{\alpha}$) derivatives

In order to estimate the plunging ($\dot{\alpha}$) derivatives of the duct, we shall use an approximate analysis which is independent of the foregoing results for α and q and which is based on the apparent mass concept, as mentioned in Section 2. Again, we shall make use of the initial assumption that $c \ll D$ and utilize the flat-plate formulas for each chordwise strip of the duct.

We shall estimate the $\dot{\alpha}$ derivatives of the duct normal force and the duct pitching moment, but not of the thrust force. The

reason for this is that only the normal force and moment deriva-
tives appear independently in the equations for the natural
frequency and damping of a vehicle at small angle of attack.
The approximate method used to find the duct $\dot{\alpha}$ derivatives seems
justified by the fact that they are found to represent only about
1 percent of the total damping of a torpedo-like configuration,
to which the static normal-force derivative C_{N_α} of the duct is
actually the major contributor.

The plunging stability derivatives of the isolated duct will
be calculated by considering the flight condition illustrated in
Figure 1(a) where the duct is situated in a steady free stream at
small angle of attack $(\alpha_o \ll 1)$ and oscillates with a normal
velocity component

$$v = v_m \sin \nu t \qquad (23)$$

and a simultaneous axial velocity component

$$u = u_m \sin \nu t \qquad (24)$$

The oscillations are assumed to be of small amplitude and of low
frequency. In addition, the oscillations are taken to be normal
to V_o with u and v in phase with one another. That is,

$$u = - v \sin \alpha_o \qquad (25)$$

so that $\dot{v} = 0$, and $\dot{\alpha}$ is given by

$$\dot{\alpha} = - \frac{\dot{v}}{V_o \cos \alpha_o} \approx - \frac{\dot{v}}{V_o} \qquad (26)$$

The instantaneous flow condition corresponds to the free stream V at α as shown in Figure 1(a). The distribution of bound and trailing vorticity from the duct now consists of two parts:

(a) The steady-state distribution corresponding to the instantaneous flow condition (V at α in Section 3.1.2) which is in phase with velocity v.

(b) A distribution which is in phase with acceleration $\dot{v}$.

Within the framework of this analysis, the force and moment acting on each chordwise strip of the duct correspond with those on a flat plate in the same orientation performing the same motion. Now, the force and moment on an oscillating flat plate in a uniform stream at small angle of attack can be found in Reference 8 (pp. 293-303), and it can be shown that for any combination of u_f and v_f at low amplitude and frequency, there are: (1) a lift force acting at the quarter chord which corresponds with the instantaneous flow condition (V at α) and which is in phase with the velocity v_f, and (2) a force normal to the plate acting at its midchord and in phase with acceleration $\dot{v}_f$. At low frequency the latter force _per unit span_ is approximately given by the quasi-steady formula

$$N_f = - \frac{\pi c^2}{4} \rho \dot{v}_f \tag{27}$$

and evidently it does not depend upon either the free-stream condition or the axial component of acceleration (V, α, or $\dot{u}_f$). The factor $(\pi c^2/4)\rho$ is recognized as the apparent mass of a flat

plate of chord c undergoing normal oscillations $\dot{v}_f$. For stream-
wise oscillations $\dot{u}_f$, the apparent mass is clearly zero.

Applying the above results to each chordwise strip of the
isolated duct and integrating round the duct, one finds a normal
force acting at the midchord diameter, in phase with $\dot{v}$, which is
given by

$$N_D = -\frac{\pi^2 c^2 D}{8} \rho \dot{v} = \frac{\pi^2 c^2 D V_o \dot{\alpha} \rho}{8} \tag{28}$$

Thus, the apparent mass of the duct (for $\dot{v}$ at small α_o) is
that of a toroidal volume of fluid with the dimensions shown in
Sketch A.
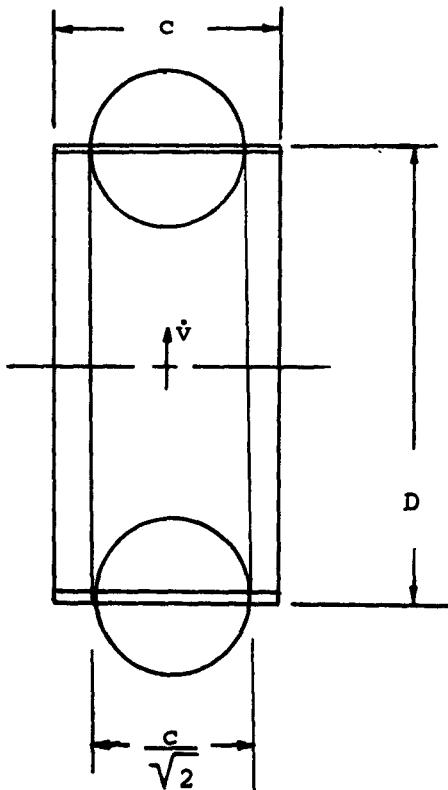
Sketch A.- Apparent mass of a duct for
lateral oscillation ($\dot{v}$).

Now, as described in Section 2, the plunging derivative can be found by differentiating Equation (28) with respect to $D\dot{\alpha}/V_o$ holding V_o constant. This gives, for $\alpha_o \ll 1$,

$$\left(C_{N_{\dot{\alpha}}}\right)_D = \pi \frac{c^2}{D^2} \qquad (29)$$

It will be assumed further that the propeller interference has no effect on $N_{D_{\dot{\alpha}}}$ so that when $\alpha_o \ll 1$,

$$\left(C_{N_{\dot{\alpha}}}\right)_{D(P)} = \left(C_{N_{\dot{\alpha}}}\right)_D = \pi \frac{c^2}{D^2} \qquad (30)$$

This seems to be a reasonable approximation since the apparent mass of the duct is independent of the free stream (Eq. (27)), and since the corresponding apparent mass of the propeller is much smaller than that of the duct. Also, since $N_{D_{\dot{\alpha}}}$ acts at the midchord diameter, we find that the corresponding moment vanishes. That is,

$$\left(C_{m_{\dot{\alpha}}}\right)_{D(P)} = 0 \qquad (31)$$

3.2 Stability Derivatives of an Isolated Propeller

The duct stability derivatives have been calculated in Section 3.1 by representing the propeller as a uniformly loaded actuator disk, for which the stability derivatives are all zero. We expect the actual propeller derivatives to be small compared with those of the duct, and this will be verified here (with the exception of C_{m_q}) for a typical example. To calculate the

propeller stability derivatives, we shall first use the analysis
of Reference 5 to calculate the derivatives of a simple paddle-wheel
type of isolated propeller (having constant blade pitch and chord).
Then the duct interference on the propeller will be estimated by
approximating the change in flow due to the duct. These effects
will be added, and finally the resulting propeller derivatives
will be compared with those of the duct.

The analysis of Reference 5 is based upon blade element theory
in which each element operates in a uniform induced flow field
which is found from simple momentum theory. Empirical constants
are introduced such as a "side wash factor" and a "spinner factor,"
and the theory is limited to small angle of attack α_o. The theory
gives the α derivatives of either a single or a dual propeller,
and the q derivatives of a single propeller.

3.2.1 Static (α) derivatives

The static derivatives of a single isolated propeller at a
small constant angle of attack α_o, (p. 11, Ref. 5) give rise to
a normal force N_{p_α} and a yawing moment $N_{p_\alpha}^*$. For dual counter-
rotating propellers, N_{p_α} is increased from 18 to 32 percent for
typical aircraft propellers, and $N_{p_\alpha}^*$ is zero. Specific values
have been calculated for the following assumed conditions:

$$c_{l_\alpha} = \text{blade section lift curve slope} = 2\pi$$

$$\beta = \text{blade pitch angle} = \text{const}$$

$$b = \text{blade chord} = \text{const}$$

$$\lambda = \frac{V_o}{\omega D} = \text{advance ratio} = 0.1$$

$$\sigma = \frac{4Bb}{3\pi D} = \text{propeller solidity (at 3/4 D)} = 0.1$$
$$\text{(where } B = \text{number of blades)}$$

$$C_{T_p} = \text{propeller thrust coefficient} = 2.17$$

The following factors, defined in Reference 5, are used:

$$a = \text{function of } T_c = 0.392 \text{ for } T_c = \frac{\pi}{8} C_{T_p} = 0.85$$

$$f(a) = \text{function of } a = 1.52$$

$$k_a = \text{side-wash factor} = 0.4$$

$$k_s = \text{spinner factor} = 1.14$$

$$I_1 = \frac{3}{2} \pi \sin \beta$$

For three values of β, the static stability derivatives are given in Table I for either single or dual propellers (whichever gives the larger value of the derivative in question).

The approximate values of $\left(C_{N_\alpha}\right)_P$ in Table I are from the following simple equation (p. 15, Ref. 5) which neglects the effects of induced velocity

$$\left(C_{N_\alpha}\right)_P \simeq f(a)k_s\sigma I_1 = 0.816 \sin \beta \tag{32}$$

It can be seen in Table I that this equation gives approximate values about three times greater than the more refined analysis for the present case.

3.2.2 Pitching (q) derivatives

Equations for the q derivatives of a single isolated propeller are given on page 13 of Reference 5. The pitching propeller

develops a side force Y_P and a pitching moment M_P, and we obtain the values in Table II for the same conditions assumed in Section 3.2.1 above.

The approximate values in Table II are from Equations (49), Reference 5, which neglect the effects of induced velocity. These equations can be written as

$$\left(C_{Y_q}\right)_P = - \frac{3}{4} \pi (1 + a)\sigma \cos \beta = - 0.33 \cos \beta \tag{33}$$

$$\left(C_{m_q}\right)_P = - 2(1 + a)\sigma = - 0.28 \tag{34}$$

where $a = 0.85$ and $\sigma = 0.1$, as before. It can be seen in Table II that these equations give approximate values about twice as large as those from the more refined analysis for the present case.

For comparison with Equation (34), the simple blade element method (used in Ref. 9) was employed to estimate $\left(C_{m_q}\right)_P$ for a paddle-wheel type of propeller (β = const, b = const, $c_{l_\alpha} = 2\pi$). This method assumes a very low advance ratio ($\omega D \gg V_o$), neglects induced flow effects, and gives

$$\left(C_{m_q}\right)_P = - \frac{3}{32} \pi \sigma \left(\frac{\omega D}{V_o} \right) \tag{35}$$

For the previously assumed conditions, we have

$$\sigma \left(\frac{\omega D}{V_o} \right) = 1 \tag{36}$$

so that Equation (35) gives

$$\left(C_{m_q}\right)_P = - 0.29 \tag{37}$$

This result is in good agreement with Equation (34). This latter method, however, gives no side force.

3.2.3 Plunging (ȧ) derivatives

The (ȧ) derivative of a plunging isolated propeller will be estimated here by use of the apparent mass method, applying the flat-plate result given by Equation (27) to each blade element. Consider one pair of propeller blades, shown in Sketch B, having constant chord b, constant pitch β, and located at azimuth angle ϕ. If the propeller oscillates laterally ($\dot{v}$ at low frequency and amplitude) then the component of $\dot{v}$ normal to the blade surface is $\dot{v} \sin\beta \cos\phi$ and there is a force in phase with $\dot{v}$ acting at the center of each blade surface and normal to it (Eq. (27)). Thus, the total force on each blade is

$$N_f = \frac{\pi b^2}{4}\ \frac{D}{2}\ \rho\dot{v}\sin\beta\sin\phi$$

End views of blades
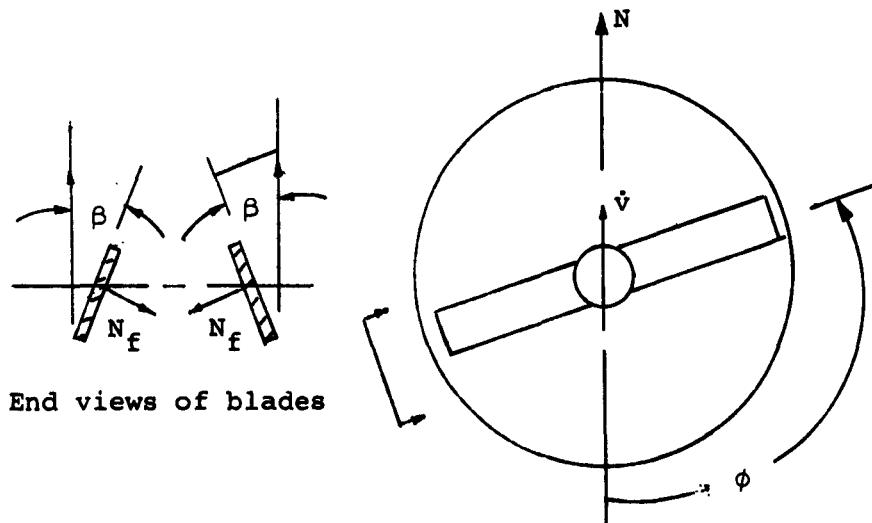
Sketch B.- Oscillating propeller nomenclature.

Hence, the net force on the blade pair normal to the duct axis is simply (Sketch B)

$$N = 2N_f \sin \beta \sin \phi = - \frac{\pi b^2 D}{4} \rho \dot{v} \sin^2 \beta \sin^2 \phi \qquad (39)$$

For $B/2$ pairs of blades, we have the total normal force on the propeller (integrated over ϕ to give the time average value)

$$N_P = \pi N \frac{B}{2} = - \frac{\pi^2 B b^2 D}{8} (\sin^2 \beta) \rho \dot{v} \qquad (40)$$

When $\alpha_o \ll 1$ such that $\dot{\alpha} = - \dot{v}/V_o$, differentiating with respect to $D\dot{\alpha}/V_o$ (holding V_o constant) gives

$$\left(C_{N_{\dot{\alpha}}} \right)_P = + \pi B \left(\frac{b}{D} \right)^2 \sin^2 \beta \qquad (41)$$

3.3 Interference of Duct on Propeller

Here we shall estimate the aerodynamic force generated by the duct on the propeller blades. We shall approximate this effect by first estimating the velocity profiles induced by the duct at the propeller plane and then estimating the effect produced on the propeller blade elements. For configurations which include a long hull, the total propeller reactions including interference will be relatively unimportant (see Section 3.5). For the isolated ducted propeller (Section 3.4), the propeller pitching moment due to pitch $M_{(D \to P)_q}$ is the only interference effect which is not small compared with the duct reaction itself. For configurations where this is significant (e.g., flying platforms and VTOL designs), the present estimate of $M_{(D \to P)_q}$ should be considered a first

approximation to the first step of an iterative process. That is, duct interference causes the propeller disk loading to be non-uniform, which changes the bound vorticity and net reaction on the duct. This, in turn, changes the propeller disk loading, and so on. This process is beyond the scope of the present study.

Here the duct interference is considered to be due only to the axial velocity component induced by the duct at the propeller location. The effects of the radial and tangential velocity components induced by the duct are probably small and are not considered. The duct interference on the propeller is due to three sources which will be estimated in succession below: (1) the bound vorticity γ_h, (2) the bound vorticity γ_α due to the free stream V_o at angle of attack α_o, and (3) the bound vorticity γ_q due to the pitching motion. It can be seen in Figure 2 that the trailing vortex filaments shed from the duct do not directly induce an axial component of velocity at the propeller, since they are aligned with the duct axis. However, they do induce an upwash on the duct and thereby influence the bound vorticity γ_α and γ_q which in turn causes duct interference upon the propeller.

Interference effects for the plunging ($\dot{\alpha}$) motion cannot be found with the apparent mass method employed here. However, with a long hull (Section 3.5), the apparent mass of the ducted propeller is found to give a negligibly small force and moment on the hull (Tables V and VI). For lateral ($\dot{v}$) oscillations of an isolated ducted propeller, the apparent mass of the propeller is much smaller than that of the duct (Section 3.4). Therefore, interference is probably unimportant here also.

3.3.1 Velocity profiles induced by $\gamma_h + \gamma$

Let us consider the axial velocity profiles $(u_{\gamma_h} + u_\gamma)$ induced within the duct by $\gamma_h + \gamma$. We have already found the axial velocity at the inner duct surface; it is $w_h + w_{h_i}$, where w_h is given by Equations (A.15) plus (A.47) and w_{h_i} is given by Equations (D.5) through (D.7), evaluated on page D-4.

At points away from the duct surface, the elementary velocity du_{γ_h} induced by the bound vorticity on each ring element of the duct is given by the results on page 305 of Reference 6. The vorticity on each ring element can be found from Equation (A.50) in terms of γ. Combining these results and summing over the duct surface, we obtain the following expression for the total velocity induced (at r, θ) by the duct bound vorticity γ_h (at θ').

$$u_{\gamma_h} = \frac{c\gamma}{2\pi^2 D} \int_0^\pi \frac{\left(\ln 16 \frac{D}{c} - 2\right) \tan \frac{\theta'}{2} \sin \theta' + (\pi - \theta') \sin \theta'}{\sqrt{\frac{\xi_R^2}{R^2} + \left(\frac{r}{R} + 1\right)^2}}$$

$$\left\{ K(k) - \left[1 + \frac{2(r/R - 1)}{\xi_R^2/R^2 + \left(\frac{r}{R} - 1\right)^2} \right] E(k) \right\} \, d\theta' \qquad (42)$$

where

$$\frac{\xi_R^2}{R^2} = \frac{c^2}{D^2} (\cos^2 \theta - 2 \cos \theta \cos \theta' + \cos^2 \theta') \qquad (43)$$

$$k^2 = \frac{4(D^2/c^2) r/R}{\cos^2 \theta - 2 \cos \theta \cos \theta' + \cos^2 \theta' + \frac{D^2}{c^2} \left(\frac{r}{R} + 1\right)^2} \qquad (44)$$

For various radial locations $(r < 0.8R)$, Equation (42) was evaluated on the Vidya IBM 1620.

The ratio u_γ/γ for the axial velocity component u_γ induced by a vortex cylinder of strength γ can be obtained directly from Table 15 on page 328 of Reference 6. The combined dimensionless axial velocity profiles $(u_{\gamma_h} + u_\gamma)/\gamma$ induced by $\gamma_h + \gamma$ as found by the procedure described above are plotted in Figure 3(a) for three axial stations in a duct with $c = 0.2D$ and with the propeller in the exit plane. These profiles do not depend upon the location of the propeller in the duct if it is represented as an actuator disk (see Appendix C). Therefore, the profiles show the individual velocity components u_{γ_h} and $u_\gamma = \gamma/2$ at three alternate propeller locations within the duct.

The results of this section (Fig. 3(a)) show that γ_h and γ induce a nearly constant axial velocity at the propeller which reduces the effective angle of attack of the free stream (α_o as seen by the propeller) and causes the blade pitch β (or speed ω) to be higher for a fixed thrust coefficient $c_{T_{P(D)}}$. Only the effect of γ_h is directly due to the duct since γ is shed by the propeller. However, the effect of both γ_h and γ are considered here to be a part of the initial propeller design problem rather than thrust force interference.

3.3.2 Interference produced by γ_α

Let us now consider the axial velocity u_{γ_α} induced by γ_α. The axial velocity induced at the inner duct surface by γ_α can be found from $w_\alpha + w_{\alpha_i}$. Thus, Equations (A.66) and (D.12) give

$$\left(u_{\gamma_\alpha}\right)_s = \frac{\Gamma_\alpha}{2\pi D} \left(\frac{2D}{c} \tan \frac{\theta}{2} + \ln \frac{16D}{c} - G_1 \right) \tag{45}$$

It can be seen (Eq. (A.64)) that Γ_α is proportional to $\cos \phi$.

Now, the radial variation of u_{γ_α} will be estimated near the center line of the duct by considering Γ_α to be concentrated at a single ring vortex. For small values of c/D and r/R, this approximation yields accurate values of u_{γ_α}. We can therefore write (using pp. 305 to 307 of Ref. 6)

$$u_{\gamma_\alpha} = \frac{\Gamma_k}{2\pi D} \int_0^{2\pi} \frac{\left\{ R' \left[1 - \cos(\phi - \phi') \right] + 1 - R' \right\} \cos \phi' \, d\phi'}{\left\{ \frac{4\xi_R^2}{D^2} + R'^2 - 2R' + 1 + 2R' \left[1 - \cos(\phi - \phi') \right] \right\}^{3/2}} \tag{46}$$

where $R' = r/R$.

Integration of Equation (46), by use of Equation (A.54) and the results on page 306, Reference 6, gives

$$u_{\gamma_\alpha} = - \frac{\Gamma_\alpha}{2\pi D \sqrt{R'} \, k} \left[(3k^2 - 4)K + (4 - k^2)E \right.$$

$$\left. - \frac{1 - R'}{R'} \left(\frac{k^2}{4} \right) \left(\frac{2 - k^2}{1 - k^2} E - 2K \right) \right] \tag{47}$$

In the plane of the vortex ring ($\xi_R = 0$), we obtain

$$k^2 = \frac{4R'}{(R' + 1)^2} \tag{48}$$

and

$$\frac{2\pi D}{\Gamma_\alpha} u_{\gamma_\alpha} = - \frac{1}{2R'} \left[(3k^2 - 4)K + (4 - k^2)E + 2 \frac{R'^2 + 1}{R'^2 - 1} E - 2 \frac{R' - 1}{R' + 1} K \right]$$

(49)

Thus, evaluation of Equation (49) gives the following variation of $(2\pi D/\Gamma_\alpha) u_{\gamma_\alpha}$ over the propeller disk.

$R' = \frac{r}{R}$	$\frac{2\pi D}{\Gamma_\alpha} u_{\gamma_\alpha}$
0	0
1/10	+0.06
1/4	+ .35
1/2	+1.96

These values and those from Equation (45) for $c = 0.2D$ are plotted in Figure 3(b). These profiles, when added to those in Figure 3(a) give the duct-induced velocity distribution over the propeller disk at angle of attack.

We shall now estimate the propeller interference produced by u_{γ_α} by making the rough approximation that the velocity profiles are linear with r/R, as shown by the dashed lines in Figure 3(b). We shall see later that the final results are insensitive to this approximation. Thus, the assumed velocity profile is from Equation (45)

$$u_{\gamma_\alpha} = \left(u_{\gamma_\alpha} \right)_s \frac{r}{R} = \frac{\Gamma_k}{2\pi D} \left(\frac{2D}{c} \tan \frac{\theta}{2} + \ln \frac{16D}{c} - G_1 \right) \frac{r}{R} \cos \phi$$

(50)

We shall also assume that the propeller consists of B blades of constant chord b and that its peripheral speed ωr is much larger than the axial velocity u_{γ_α}. The angle of attack on a blade element changes by an amount $(-u_{\gamma_\alpha}/\omega r)$, which causes a pitching moment (but no net force) on each pair of blades. The elementary pitching moment on a pair of blades is given by

$$dM_{(D \to P)_\alpha} = -2b \frac{\rho}{2} (\omega r)^2 r \cos \phi \left(\frac{u_{\gamma_\alpha}}{\omega r}\right) c_{l_\alpha} \, dr \qquad (51)$$

We shall assume here that $c_{l_\alpha} = 2\pi$ as before. Then

$$dM_{(D \to P)_\alpha} = -b \frac{\rho}{2} \frac{\omega D^2 \Gamma_k}{4} (\cos^2 \phi) \left(\frac{2D}{c} \tan \frac{\theta}{2} + \ln \frac{16D}{c} - G_1\right) \left(\frac{r}{R}\right)^3 d \frac{r}{R} \qquad (52)$$

where θ corresponds to the axial location of the propeller in the duct. Integration gives the moment per pair of blades as

$$M'_{(D \to P)_\alpha} = -\frac{b\rho\omega D^2 \Gamma_k}{32} (\cos^2 \phi) \left(2 \frac{D}{c} \tan \frac{\theta}{2} + \ln \frac{16D}{c} - G_1\right) \qquad (53)$$

Thus, for B/2 pairs of blades, the total pitching moment (time averaged) on the propeller due to u_{γ_α} is

$$M_{(D \to P)_\alpha} = \frac{B}{2} \frac{1}{2\pi} \int_0^{2\pi} M'_{(D \to P)_\alpha} \, d\phi$$

$$= -\frac{Bb\rho\omega D^2 \Gamma_k}{128} \left(2 \frac{D}{c} \tan \frac{\theta}{2} + \ln \frac{16D}{c} - G_1\right) \qquad (54)$$

Differentiating with respect to α_0 and using Equation (A.64) for Γ_k, we find that the interference of the duct on the propeller produces the following interference pitching moment.

$$\left(C_{m_\alpha}\right)_{D \to P} = - \frac{3 \frac{c}{D} \sigma}{32\left(1 + \frac{\pi c}{2D}\right)} \left(2 \frac{D}{c} \tan \frac{\theta}{2} + \ln \frac{16D}{c} - G_1\right) \frac{\omega D}{V_0} \cos \alpha_0$$

$$(55)$$

If, in lieu of Equation (50), we had assumed that $u_{\gamma_\alpha} = \left(u_{\gamma_\alpha}\right)_s = const$, integration over r would have given a result only $4/3$ times larger. Thus, the interference effect is quite insensitive to the profile shape. For small angles of attack $(\alpha_0 \ll 1)$, we find that the ratio of interference to duct moment (Eq. (13) and (55)) is given by

$$\frac{\left(C_{m_\alpha}\right)_{D \to P}}{\left(C_{m_\alpha}\right)_{D(P)}} = - \frac{3\pi\sigma}{128} \left(\frac{\omega D}{V_0}\right) \frac{V_0}{\gamma} \frac{2 \frac{D}{c} \tan \frac{\theta}{2} + \ln \frac{16D}{c} - G_1}{\ln \frac{16D}{c} - 2} \qquad (56)$$

where $G_1 = 2, 3,$ or 4 for the propeller located at the duct leading edge, midchord, or trailing edge, respectively (see Eq. (D.12)). Thus, $\left(C_{m_\alpha}\right)_{D \to P}$ is probably generally small compared with $\left(C_{m_\alpha}\right)_{D(P)}$ except for propeller locations near the duct leading edge.

3.3.3 Interference produced by γ_q

The interference from the duct bound vorticity γ_q will be estimated now by the same technique used above for γ_α. At the inner duct surface, the axial velocity induced by γ_q is $\left(u_{\gamma_q}\right)_s = w_q + w_{q_i}$. As above, we shall assume that the axial velocity profile is linear with radius, so that, using Equations (A.88), (A.90), (A.94), (D.16), (D.17), and (D.18), we find

$$
u_{\gamma_q} = \left(w_q + w_{q_i}\right) \frac{r}{R} = \frac{qc^2}{8D} \left(4 \frac{D}{c} \sin \theta + 4 \frac{D^2}{c^2}\right.
$$

$$
\left. - \frac{\pi}{1 + \frac{\pi c}{2D}} \tan \frac{\theta}{2} + G_2 \right) \frac{r}{R} \cos \phi \tag{57}
$$

where G_2 is evaluated on page D-7.

By analogy with Equations (50) and (54), it can be seen that the pitching moment on the propeller due to u_{γ_q} is

$$
M_{(D \to P)_\alpha} = - \frac{Bb\rho\omega D^2}{128} \left(2\pi D \frac{qc^2}{8D}\right) \left(4 \frac{D}{c} \sin \theta + 4 \frac{D^2}{c^2} - \frac{\pi}{1 + \frac{\pi c}{2D}} \tan \frac{\theta}{2} + G_2 \right) \tag{58}
$$

or

$$
\left(C_{m_q}\right)_{D \to P} = - \frac{3\pi}{128} \frac{c^2}{D^2} \sigma \frac{\omega D}{V_o} \left(4 \frac{D}{c} \sin \theta + 4 \frac{D^2}{c^2} - \frac{\pi}{1 + \frac{\pi c}{2D}} \tan \frac{\theta}{2} + G_2 \right) \tag{59}
$$

Thus, using Equation (22) for the duct moment gives the following moment ratio for pitching:

$$
\frac{\left(C_{m_q}\right)_{(D \to P)}}{\left(C_{m_q}\right)_{D(P)}} = - \frac{3\pi}{64} \frac{1}{\left(\ln \frac{16D}{c} - \frac{5}{2}\right)} \sigma \left(\frac{\omega D}{V_o}\right) \frac{V_o}{\gamma} \left(4 \frac{D}{c} \sin \theta \right.
$$

$$
\left. + 4 \frac{D^2}{c^2} - \frac{\pi}{1 + \frac{\pi c}{2D}} \tan \frac{\theta}{2} + G_2 \right) \tag{60}
$$

In Section 3.4.2 it will be shown that this ratio is large for the conditions assumed there. The $\tan(\theta/2)$ term in Equations (60) and (57) is comparatively small except near the leading edge of the duct where it dominates. This causes the interference moment to reverse sign with variation of propeller location θ.

Both γ_α and γ_q and the axial velocity profiles induced by them are all proportional to $\cos \phi$. This causes only pitching moments on the propeller due to α or q interference so that $N_{P(D)} = N_P$ and $Y_{P(D)} = Y_P$. The theoretical pitching moments are infinitely large when the propeller is at the duct leading edge because of the mathematical singularity there which invalidates the assumption that the angle of attack on the propeller blade element changes by only a small amount due to duct interference.

3.4 Comparison of Duct and Propeller Reactions for an Isolated Ducted Propeller

The static coefficients and stability derivatives of the duct and propeller as determined above will now be compared for a specific configuration in order to illustrate their relative magnitudes and overall importance for an isolated ducted propeller (and hence for certain VTOL configurations). It is found that all of the propeller reactions are small compared with the duct reactions except the propeller pitching moment due to pitching. In Section 3.5.4, it is shown that even this component is negligible when the ducted propeller is combined with a long hull. It should be noted, however, that two of the reaction components for an isolated propeller are perpendicular to the motion (a yawing moment due to α_0 and a side force due to q). The results given below are for small angles of attack, an aircraft type propeller which is moderately loaded, and a duct with $c = 0.2D$. Duct interference on the propeller causes only pitching moments with α and ϕ (Section 3.3). The duct moments are about its midchord diameter and the propeller

moments are about its own diameter.[2] The propeller conditions assumed for Section 3.2 are also applied here; for example,

$\sigma \frac{V_o}{\omega D} = 1$ and $C_{T_{P(D)}} = 2.17$. From Equation (170), we can evaluate γ/V_o in terms of $C_{T_{P(D)}}$ to find that these conditions lead to $\gamma/V_o = 0.78$.

3.4.1 Static (α) derivatives

First, consider the normal force derivatives of the duct and propeller at small angle of attack α_o. For the duct in the presence of an actuator disk (Eq. (9) with $c = 0.2D$), we have

$$\left(C_{N_\alpha}\right)_{D(P)} = 1.91 + 0.845 \frac{\gamma}{V_o} = 2.57 \tag{61}$$

For the propeller (from Table I)

$$\left(C_{N_\alpha}\right)_{P(D)} = 0.05, 0.10, 0.16 \text{ for } \beta = 10^\circ, 20^\circ, 30^\circ \tag{62}$$

Thus, the normal force on the duct is much larger than on the propeller.

Now, let us compare the pitching moments on the duct and propeller and the yawing moment on a single propeller. The duct moment derivative is (Eq. (13)).

$$\left(C_{m_\alpha}\right)_{D(P)} = 1.45 \frac{\gamma}{V_o} = 1.13 \tag{63}$$

---

[2]For small values of c/D we shall assume that the axes of pitch and moment for the duct and propeller coincide.

From Table I, the propeller yawing moment derivative is

$$\left(C_{n_\alpha}{}^*\right)_{P(D)} = 0.4 \quad \text{for } 10 < \beta < 30^\circ \quad \text{for a single propeller}$$

$$= 0 \quad \text{for a dual propeller}$$

The propeller pitching moment due to duct interference is given by Equation (56) as

$$-\frac{\left(C_{m_\alpha}\right)_{(D \rightarrow P)}}{\left(C_{m_\alpha}\right)_{D(P)}} = \infty,\ 0.451,\ 0.015 \qquad\qquad (65)$$

with the propeller located at the leading edge, midchord, and trailing edge of the duct, respectively. Thus, the propeller interference moment is smaller than the duct moment unless the propeller is located near the leading edge of the duct.

The thrust ratio from Equation (11) and with $C_{T_{P(D)}} = 2.17$ is

$$\frac{C_{T_{D(P)}}}{C_{T_{P(D)}}} = 0.20 \qquad\qquad (66)$$

so that the duct carries only 16.7 percent of the total thrust.

3.4.2 Pitching (q) derivatives

The pitching derivatives will now be compared at $\alpha_o = 0$. The duct normal force derivative is from Equation (18)

$$\left(C_{N_q}\right)_{D(P)} = 0.675\ \frac{\gamma}{V_o} + 0.126 = 0.65 \qquad\qquad (67)$$

The side force derivative of a single propeller is from Table II

$$\left(C_{Y_q}\right)_{P(D)} = -0.15 \quad \text{for} \quad \beta = 10^\circ$$

$$= -0.12 \quad \text{for} \quad \beta = 30^\circ \tag{68}$$

Thus, the duct normal force is about five times larger than the side force on the propeller.

Now let us compare the pitching moment on the duct and single propeller. For the duct (Eq. (22)) we have

$$\left(C_{m_q}\right)_{D(P)} = + 0.0376 \frac{\gamma}{V_o} = 0.029 \tag{69}$$

For the propeller (Table II)

$$\left(C_{m_q}\right)_P = -0.17 \quad \text{for} \quad 10 < \beta < 30^\circ \tag{70}$$

But due to duct interference on the propeller (Eq. (60)), we get

$$\frac{\left(C_{m_q}\right)_{(D \rightarrow P)}}{\left(C_{m_q}\right)_{D(P)}} = + \infty, \ -12.0, \ -10.2 \tag{71}$$

for leading-edge, midchord, and trailing-edge propeller locations, respectively. Thus, the net propeller pitching moment reverses sign with propeller position as mentioned below (Eq. (60)). It is generally large compared with that of the duct and it is dominated by duct-propeller interference.

3.4.3 Plunging ($\dot{\alpha}$) derivatives

For the duct normal force the plunging derivative is from Equation (30)

$$\left(C_{N_{\dot{\alpha}}}\right)_{D(P)} = \pi \frac{c^2}{D^2} = 0.13 \tag{72}$$

This force acts at the duct midchord, so that $\left(C_{m_{\dot{\alpha}}}\right)_{D(P)} = 0.$

The plunging derivative of the propeller normal force is given by Equation (41). Previously, we have assumed

$$\sigma = \frac{4Bb}{3\pi D} = \frac{1}{10} \tag{73}$$

Here, we shall also assume a three-bladed propeller (B = 3) so that D = 12.7b. Then we have

$$\left(C_{N_{\dot{\alpha}}}\right)_{P(D)} = 0.058 \sin^2 \beta, \text{ and } \left(C_{m_{\dot{\alpha}}}\right)_{P(D)} = 0 \tag{74}$$

Thus, the apparent mass of the propeller is considerably smaller than that of the duct, and the interference effect of the duct on the propeller is probably negligible as assumed in Section 3.3.

3.4.4 Summary

Specific calculations have been made for a moderately loaded, aircraft type, ducted propeller of low solidity. The propeller could be either single or dual for α, but only single for q.

The results of this section indicate that for an isolated ducted propeller of this type (and hence for certain VTOL configurations), all of the forces and moments on the duct are larger than on the propeller except for (1) the pitching moment due to pitch, and (2) the thrust force.

The motion studied consisted of small rates of pitching and plunging about a straight-line flight path aligned with the duct

axis because of the analytical restrictions used to obtain the duct plunging derivatives and all of the propeller stability derivatives. The midchord duct diameter was taken as the axis of pitching and the center of duct moments. The propeller pitching and moments were taken about its own diameter. The duct and propeller axes coincide for $c \ll D$. It should be borne in mind that two of the propeller reaction components were perpendicular to their duct counterparts (a yawing moment due to α and a side force due to q).

The duct interference on the propeller markedly increased its stabilizing moment for pitching if it was not located near the duct leading edge. This can be significant for VTOL-type applications.

3.5 Calculative Example of a Torpedo-Like Configuration

In this section the foregoing results will be employed to estimate the dynamic stability of a complete torpedo-like configuration. The purpose is to determine the relative importance of the ducted propeller derivatives for this type of vehicle.

We shall consider small rates of pitching and plunging about an equilibrium condition of steady axial flight with the thrust of the ducted propeller equal and opposite to the hull drag. It is found that this condition requires a very lightly loaded propeller for the assumed configuration (Fig. 4) where the propeller diameter is taken equal to the maximum hull diameter. With this assumption, the reference areas (A) of the hull and ducted propeller derivatives are the same so that they are directly comparable. The hull shape will be chosen for mathematical simplicity rather than from practical considerations; however, for the present purpose

it is probably sufficiently representative of actual hull shapes.
For purposes of the present stability analysis, the hull and ducted
propeller will be assumed to be isolated from one another (i.e.,
no duct-hull interference), but thrust equilibrium will be imposed.
This assumption will be examined qualitatively at the end of the
section.

The method of approach will be to estimate first the isolated
hull stability derivatives about its centroid by use of slender
body theory and then to calculate the isolated ducted propeller
derivatives about the hull centroid by use of the previous analysis.
The static stability of the configuration will be examined, and
sufficient fins will be added to the duct to provide a 10 percent
margin of static stability (neglecting aspect ratio and interfer-
ence effects). Finally, the dynamic stability of the entire con-
figuration will be considered by shifting the axis of pitch and
center of moments from the centroid to the assumed location of the
center of gravity of the hull(0.4L in Fig. 4) Interference between
the hull and ducted propeller will then be considered briefly in
order to furnish a better understanding of the results obtained.

3.5.1 Isolated hull derivatives about hull centroid

The stability derivatives of an isolated slender hull (Fig. 5)
will be estimated by using slender body theory and by assuming that
the hull boundary layer remains attached and axially symmetric.
The hull probably actually oscillates within its boundary layer

to some extent. Thus at small angle of attack the latter assumption probably leads to overestimation of the effect of an attached boundary layer and the hull stability derivatives. However, at higher angles of attack, which are not considered here, the boundary layer actually separates, and the normal force on the hull becomes much greater than indicated by the above method. The total drag on the hull will be taken equal to the friction drag, and its form drag will be neglected. This seems justified for the present case where the boundary layer is found to be thin. This condition is believed to be generally true for submerged torpedoes which have little wave drag.

Static (α) Derivatives

The normal force on a slender hull at small angle of attack is given by Reference 10 (page 68)

$$N_{H_\alpha} = 2\pi q_o r_L^2 \alpha_o \qquad (75)$$

where r_L is the base radius. Also, the center of pressure is at (Ref. 10)

$$a = L - \frac{Vol}{\pi r_L^2} \qquad (76)$$

where Vol is the volume of the body and L is its length (Fig. 5). For a slender body with a pointed base at small angle of attack, it is assumed that the effective base radius r_L is simply δ_L^*, the displacement thickness of the hull boundary layer at the base

(See Ref. 10, page 68). If the boundary layer is axially symmetric, then the friction drag of the body is given by $2\pi\theta_L^2 q_0$ where θ_L is the momentum thickness of the boundary layer at the base. Thus, if we neglect form drag (assuming the boundary layer be thin), then the total drag is equal to the friction drag and we have

$$X = 2\pi\theta_L^2 q_0 \tag{77}$$

It is assumed here that the hull is a body of revolution (Fig. 5) for which

$$\left(\frac{2x_H}{L}\right)^2 = 1 - \frac{r_H}{r_m} \tag{78}$$

and the hull volume is from Appendix E (Eq.(E.7) with $\delta_L^* = 0$)

$$Vol = \frac{8}{15}\pi r_m^2 L \tag{79}$$

Consequently, from the above equations, the axial and normal forces of the hull are given by

$$\frac{X}{\pi q_0 r_m^2} = 2\frac{\theta_L^2}{r_m^2} \tag{80}$$

$$\frac{N_{H_\alpha}}{\pi q_0 r_m^2} = 2\alpha_0\frac{\delta_L^{*2}}{r_m^2} \tag{81}$$

and, for no boundary-layer volume, the center of pressure is at

$$\frac{a}{L} = 1 - \frac{8r_m^2}{15\delta_L^{*2}} \tag{82}$$

The boundary layer profile over the axisymmetric hull will be taken equal to that given by the 1/7-power law (p. 432, Ref. 11) for a turbulent boundary layer over a flat plate of length L in uniform two-dimensional flow. Thus, at the hull base (Fig. 5), the boundary-layer profile is given by

$$\frac{u}{V_o} \sim \left(\frac{r}{\delta_L^*}\right)^{1/7} \tag{83}$$

for which (Ref. 11)

$$\delta_L^* = 1.29 \ \theta_L = 0.37 \ L \ \left(Re_L\right)^{-\frac{1}{5}} \tag{84}$$

where the length Reynolds number of the hull is $Re_L = (\rho V_o L)/\mu$. For a hull moving through water with kinematic viscosity $\mu/\rho = 10^{-5}(ft^2/sec)$, we can write

$$Re_L = 10^5 V_o L \tag{85}$$

Now, if $L = 10$ ft and $V_o = 40(ft/sec)$, we have $Re_L = 4 \times 10^7$. Thus, the hull boundary layer is mostly turbulent (as assumed), since transition to turbulence occurs at a length Reynolds number of approximately 2×10^6 for a flat plate[3] (or at 5 percent of the hull length). Substitution of the assumed values (Fig. 4) into Equation (84) gives

$$\delta_L^* = 0.111 \ ft = 1.34 \ in. \tag{86}$$

$$\theta_L = 0.0865 \ ft \tag{87}$$

---

[3]Kuethe, A. M. and Schetzer, J. D.: Foundations of Aerodynamics. J. Wiley and Sons, Inc., New York, p. 283.

and the drag coefficient and normal force derivative of the hull
are, from Equations (80) and (81),

$$C_X = 0.0600 \tag{88}$$

$$\left(C_{N_\alpha}\right)_H = 0.0994 \tag{89}$$

Neglecting the boundary-layer volume, we have from Equation (82)

$$\frac{a}{L} = -9.78 \tag{90}$$

However, with the displacement thickness of the assumed hull
boundary layer included, the total volume of hull and boundary
layer from Equation E.9 in Appendix E is given by

$$Vol^* = 0.709(\pi r_m^2 L) \tag{91}$$

and we find that

$$a^*/L = -13.6 \tag{92}$$

We shall use this value to obtain the pitching moment derivative
about the hull centroid. Thus (see Fig. 5) we have

$$\left(C_{m'_\alpha}\right)_H = \frac{N_{H_a}}{A q_o \alpha_o}\left(\frac{L}{2} - a^*\right)\frac{2}{D} = 0.0994(10 + 13.6 \times 20) = 28.0 \tag{93}$$

Pitching (q) derivatives

The stability derivatives for the hull pitching about its
centroid are given by the following formulas, taken from p. 371 of
Reference 10:

$$\left(C_{N'_q}\right)_H \equiv \frac{N'_{H_q}}{\pi r_m^2 q_o}\left(\frac{Lq}{2V_o}\right) = + 2\bar{A}_{22} = 2\frac{r_L^2}{r_m^2} \qquad (94)$$

and

$$\left(C_{m'_q}\right)_H \equiv \frac{M'_{H_q}}{\pi r_m^2 q_o}\left(\frac{L^2 q}{2V_o}\right) = -\bar{A}_{22} - 4C_{22} = -\frac{r_L^2}{r_m^2} - 4\int_{-\frac{1}{2}}^{+\frac{1}{2}} \frac{r_H^2}{r_m^2}\frac{x_H}{L}\, d\,\frac{x_H}{L}$$

$$(95)$$

where $\bar{A}_{22}$ and C_{22} are apparent mass coefficients defined in Reference 10, and the different reference lengths appearing in the above formulas require conversion to the present system of nomenclature. Both of the above derivatives are zero for the assumed hull shape if we neglect the boundary-layer thickness. With the previous assumptions regarding the boundary layer, the above formulas become (with $r_L = \delta^*_L$ and $C^*_{22} = -0.144$ from Appendix E, Eq.(E.13)

$$\left(C_{N'_q}\right)_H = 2\frac{\delta_L^{*2}}{r_m^2} = 0.0990 \qquad (96)$$

$$\left(C_{m'_q}\right)_H = 0.050 + 0.576 = 0.526 \qquad (97)$$

The above q derivatives for the hull are due entirely to the boundary layer. Now, converting to the present system of nomenclature, we obtain

$$\left(C_{N'_q}\right)_H = 0.0990\,\frac{L}{2D} = 0.495 \qquad (98)$$

$$\left(C_{m'_q}\right)_H = 0.526\,\frac{L^2}{D^2} = 52.6 \qquad (99)$$

Plunging (ἀ) Derivatives

The plunging (ἀ) stability derivatives for the normal force N_H and pitching moment M'_H about the centroid of the isolated hull are, from pages 369 and 374 of Reference 10,

$$\left(C_{N_{\dot{\alpha}}}\right)_H \equiv \frac{N_{H_{\dot{\alpha}}}}{\pi r_m^2 q_o} \left(\frac{2V_o}{L\dot{\alpha}}\right) = 4B_{22} = 4 \int_{-\frac{1}{2}}^{+\frac{1}{2}} \frac{r_H^2}{r_m^2} \, d\frac{x_H}{L} \qquad (100)$$

and

$$\left(C_{m'_{\dot{\alpha}}}\right)_H \equiv \frac{M'_{H_{\dot{\alpha}}}}{\pi r_m^2 q_o L} \left(\frac{2V_o}{L\dot{\alpha}}\right) = 4C_{22} = 4 \int_{-\frac{1}{2}}^{+\frac{1}{2}} \frac{r_H^2}{r_m^2} \frac{x_H}{L} \, d\frac{x_H}{L} \qquad (101)$$

where N_H (Fig. 5) is opposite in sign from Z of Reference 10. For the assumed hull shape (neglecting the displacement thickness of the boundary layer), the above formulas become

$$\left(C_{N_{\dot{\alpha}}}\right)_H = 4 \frac{Vol}{\pi r_m^2 L} = 2.13 \qquad (102)$$

$$\left(C_{m'_{\dot{\alpha}}}\right)_H = 0 \qquad (103)$$

Now, approximating the effect of the boundary layer as before the effective value of B_{22} is

$$B^*_{22} = \frac{Vol^*}{\pi r_m^2 L} = 0.709 \qquad (104)$$

and the effective value of C_{22} from Equation E.13 in Appendix E is

$$C^*_{22} = -0.144 \tag{105}$$

Therefore, Equations (100) and (101) for the hull with boundary layer become

$$\left(C_{N_{\dot{\alpha}}}\right)_H = 2.84 \tag{106}$$

$$\left(C_{m'_{\dot{\alpha}}}\right)_H = -0.576 \tag{107}$$

Thus, for pure plunging motion, all of the moment and a small part of the normal force on the hull are due to its boundary layer. Now, converting to the present system of nomenclature, we obtain for $\dot{\alpha}$ derivatives of the hull with boundary layer

$$\left(C_{N_{\dot{\alpha}}}\right)_H = 2.84 \frac{L}{2D} = 14.2 \tag{108}$$

$$\left(C_{m'_{\dot{\alpha}}}\right)_H = -0.576 \left(\frac{L}{D}\right)^2 = -57.6 \tag{109}$$

The above results for the hull are summarized in Table V.

3.5.2 Isolated ducted-propeller derivatives about the hull centroid

Here we shall determine the derivatives of the ducted propeller mounted at the base of the hull in Figure 4 by use of the results of Section 3. In order to do this, we must assume that the ducted propeller is isolated from the hull but is in thrust equilibrium with it. That is, we shall neglect all interference between the hull and ducted propeller, including the effect of the hull boundary layer flowing into the ducted propeller. Neglecting this latter effect is probably justified, since the displacement thickness of

the boundary layer at the hull base was found to be 1.34 inches, which is reasonably small compared with the assumed duct radius of 6 inches.

We shall assume that the propeller is located toward the rear of the duct, so that the duct interference on the propeller from q is not large and destabilizing. (See Eq. (71))

Thrust Equilibrium

The propeller disk loading is from Equation (170) with $\alpha_o = 0$

$$C_{T_{P(D)}} = \frac{\gamma^2}{V_o^2} \left(1 + 2 \frac{V_o}{\gamma} \right) \tag{110}$$

also, from Equation (11), we find that the duct thrust (for $\alpha_o = 0$ and $c = 0.2D$) is

$$T_{D(P)} = \frac{0.724}{1 + 2(V_o/\gamma)} T_{P(D)} \tag{111}$$

Thus, the total thrust of the ducted propeller is given by

$$C_{T_{D(P)}} \equiv \frac{T_{P(D)} + T_{D(P)}}{Aq_o} = 1.724 \frac{\gamma^2}{V_o^2} + 2 \frac{\gamma}{V_o} \tag{112}$$

For thrust equilibrium of the entire vehicle, we have $T_{D(P)} + T_{P(D)} = X$. Using Equation (88) for the drag coefficient of the hull, we obtain

$$C_X = \frac{X}{Aq_o} = 1.724 \frac{\gamma^2}{V_o^2} + 2 \frac{\gamma}{V_o} = 0.060 \tag{113}$$

so that

$$\frac{\dot{\gamma}}{V_o} = 0.050 \tag{114}$$

Thus, for the assumed configuration, the slipstream velocity V_j is only 5 percent greater than the flight speed V_o and the propeller disk loading is low. We shall now determine the stability derivatives of the isolated ducted propeller about the hull centroid for this case, namely $\alpha_o = 0$, $c = 0.2D$, and $\gamma = 0.05\ V_o$.

Static (α) Derivatives

The normal force and pitching moment derivatives of the duct are found from (Eqs. (9) and (13)) to be

$$\left(C_{N_\alpha}\right)_{D(P)} = 1.91 + 0.845 \frac{\dot{\gamma}}{V_o} = 1.95 \tag{115}$$

$$\left(C_{m_\alpha}\right)_{D(P)} = 1.45 \frac{\dot{\gamma}}{V_o} = 0.0725 \tag{116}$$

The above pitching moment is about the midchord duct diameter, so that the moment about the centroid of the hull due to the duct (Fig. 4) is given by

$$M'_{D(P)_\alpha} = M_{D(P)_\alpha} - \frac{L N_{D(P)_\alpha}}{2}$$

Thus we find that

$$\left(C_{m'_\alpha}\right)_{D(P)} = 0.07 - 19.5 = -19.4 \tag{118}$$

where the first small term is the duct moment about its own center and the second is the moment about the hull centroid due to the duct normal force.

The duct α derivatives are listed in Table III together with the propeller derivatives estimated from the results of Section 3.4.1 for either a dual or single aircraft type propeller located near the rear of the duct with $\gamma = 0.05\ V_o$. It can be seen that the normal force on the propeller is much smaller than on the duct and that the pitching moment about the hull centroid due to the propeller is much smaller than that due to the duct. It should be noted, however, that there is a smaller yawing moment on the propeller which is perpendicular to the duct moment.

Pitching (q) Derivatives

The pitching derivatives of the duct for rotation about the hull centroid are (from Eqs. (9) and (18)):

$$\left(C_{N'_q} \right)_{D(P)} = 0.675\ \frac{\gamma}{V_o} + 0.126 + \left(1.91 + 0.845\ \frac{\gamma}{V_o} \right)\left(\frac{\alpha_o' V_o}{Dq} \right) = 9.91$$

(119)

and from Equations (13) and (22)

$$\left(C_{m_q} \right)_{D(P)} = 0.0376\ \frac{\gamma}{V_o} + 0.0725 \left(\frac{\alpha_o' V_o}{Dq} \right) = 0.364 \qquad (120)$$

The last term in each expression is due to the induced angle of attack which is introduced at the ducted propeller by rotation about the hull centroid,

$$\alpha_o{}' = \frac{qL}{2V_o} \tag{121}$$

The pitching moment about the centroid of the hull (denoted by a prime) due to the duct is

$$M'_{D(P)_q} = M_{D(P)_q} - \frac{L}{2} N_{D(P)_q} \tag{122}$$

so that

$$\left(C_{m'_q}\right)_{D(P)} = 0.364 - 99.1 = -98.7 \tag{123}$$

Note that the duct moment about its own center $M_{D(P)_q}$ is negligible, just as was $M_{D(P)_\alpha}$.

The duct q derivatives are listed in Table IV for comparison with the propeller derivatives as estimated from the results of Section 3.4.2, for an aircraft type propeller located near the rear of the duct, with $\gamma = 0.05 \, V_o$.

It can be seen that the forces and moments acting at the hull centroid due to the propeller are small compared with those due to the duct. It should be noted, however, that there is a somewhat smaller side force and yawing moment on the propeller which are perpendicular to the pitching motion.

The above results show that the q damping of the ducted propeller is due almost entirely to the duct normal force arising from rotation about the hull centroid. Equations (119), (120), and (122) show that the disk loading has a small effect on pitch damping about the hull centroid for the present example, even for high disk loading.

Plunging ($\dot{\alpha}$) Derivatives

For the duct, the net hydrodynamic reaction due to $\dot{\alpha}$ is a normal force acting through the midchord plane, and from Equations

(30) and (31) we obtain

$$\left(C_{N_{\dot\alpha}}\right)_{D(P)} = \pi\left(\frac{c}{D}\right)^2 = 0.126 \qquad (124)$$

and

$$\left(C_{m_{\dot\alpha}}\right)_{D(P)} = 0 \qquad (125)$$

The pitching moment about the hull centroid due to the duct is then

$$M'_{D(P)_{\dot\alpha}} = -\frac{L}{2} N_{D(P)_{\dot\alpha}} \qquad (126)$$

and the corresponding stability derivative is

$$\left(C_{m_{\dot\alpha}}'\right)_{D(P)} = -\frac{L}{D}(0.126) = -1.26 \qquad (127)$$

From the results of Section 3.4.3, (Eq. (72) and (74)) the estimated $\dot\alpha$ reaction from the apparent mass of the propeller is negligibly small compared with that of the duct.

3.5.3 Comparison of isolated hull derivatives and isolated ducted propeller derivatives about hull centroid

The stability derivatives which have been obtained for the hull and ducted propeller about the hull centroid are summarized in Table V for comparison. It should be recalled that these results were obtained for the configuration in Figure 4, and for small oscillations from axial flight at low frequency as assumed in the $\dot\alpha$ analysis. The hull and ducted propeller are considered isolated from one another but are in thrust equilibrium. An aircraft-type propeller is located near the duct exit

plane. The hull boundary layer is assumed to be attached and axially symmetric.

The following conclusions are drawn from Table V and the foregoing analysis.

(1) The q damping moment about the hull centroid $(-C_{m_q}')$ from the propeller is small compared with that due to the duct, even though the propeller moment about its own center was comparitively large.

(2) The upwash over the duct arising from the q motion causes a stabilizing moment about the hull centroid which is greater than the destabilizing moment from the hull boundary layer.

(3) The $\dot{\alpha}$ damping $(-C_{m_{\dot{\alpha}}})$ is due mainly to the apparent mass of the hull boundary layer.

(4) Both $C_{m_{\dot{\alpha}}}'$ and C_{m_q}' for the hull are due entirely to its boundary layer for a hull with a pointed base. Since these damping components are comparatively large, refinement of the present analysis is needed. Both of these components are probably over-estimated by the present analysis for small q and $\dot{\alpha}$ motions of the hull, since the analysis assumes that the hull boundary layer remains axially symmetric.

(5) For a torpedo-like configuration, all of the propeller forces and moments (except thrust) are small compared with those of the duct. However, some of the propeller reactions are perpendicular to the motion which causes them. This is not true of the duct.

3.5.4 Static stability of torpedo-like configuration

Before we can make a dynamic stability analysis of a complete torpedo-like configuration, we must insure that the vehicle is trimmed and is statically stable. For this purpose we shall now add fins to the configuration (Fig. 4) and determine the static derivatives of the entire configuration consisting of a hull, ducted propeller, and fin. We shall not consider the comparatively small propeller forces and moments (Table III). The only interference effect which is to be included is propeller interference on the duct, so that the total normal force and pitching moment on the entire configuration are given by

$$N_{HDPF} = N_H + N_{D(P)} + N_F \qquad (128)$$

and

$$M_{HDPF}'' = M_H'' + M_{D(P)}'' + M_F'' \qquad (129)$$

The double prime superscript on the moment indicates that it is about the <u>center of gravity</u> of the hull.[4] We shall use the moment transfer equations of page 400, Reference 10 to shift the centers of moments and pitch from the hull centroid (previously considered) to the hull center of gravity. The normal force derivatives due to α and $\dot{\alpha}$ are not affected by this transfer and can be taken directly from Table V. All the other stability derivatives, however, are affected.

---

[4]It is assumed that the center of gravity of the hull is the same as that of the complete vehicle.

The center of gravity of the entire configuration is assumed to be at 0.4L (Fig. 4). Using Table V, we find that the center of pressure of the hull and duct is located a distance $x_{c.p.}$ ahead of the hull centroid as given by

$$\frac{x_{c.p.}}{L} = \frac{M'_{H_\alpha} + M'_{D(P)_\alpha}}{N_{H_\alpha} + N_{D(P)_\alpha}} = \frac{(28.0 - 19.4)D/2L}{0.10 + 1.95} = 0.21$$

(130)

Thus the center of pressure is located 0.29L from the nose in Figure 4 and is ahead of the assumed center of gravity. Since this results in static instability, we must add fins to make the configuration statically stable. We shall add fins near the base of the hull (Fig. 4) which are sufficiently large to place the center of pressure at the hull centroid (0.5L) and thereby obtain a "10-percent static margin." We shall use a fin with chord c and exposed span S, such that the net moment about the hull centroid is zero. That is,

$$M'_{F_\alpha} + M'_{H_\alpha} + M'_{D(P)_\alpha} = 0$$

(131)

Thus, using Table V, we find that

$$M'_{F_\alpha} = -8.6 \frac{D}{2} Aq_o \alpha_o$$

(132)

Now we shall neglect interference effects on the fin, assume that
its lift curve slope is 2π and make no correction for its aspect
ratio. Then we can write the normal force on the fin as

$$N_{F_\alpha} = - \frac{2M'_{F_\alpha}}{L} = 8.6 \frac{D}{L} Aq_o\alpha_o = 0.86 \left(\frac{\pi D^2}{4}\right) q_o\alpha_o = 2\pi c S q_o\alpha_o \tag{133}$$

Thus, if the fin chord is taken equal to the duct chord ($c = 0.2D$),
we find that the total required exposed fin span is

$$S = 0.537 \, D \tag{134}$$

With this fin added for static stability, the static α de-
rivatives about the hull center of gravity (0.4L) as obtained from
Table V using the transfer Equations (10-119) of Reference 10 are given
in Table VI.

3.5.5 Dynamic stability of complete configuration with no inter-
      ference between hull and ducted propeller

The dynamic stability derivatives for the hull and duct about
the vehicle center of gravity can be found by transferring their de-
rivatives about the centroid (Table V) using Equations (10-119) of
Reference 10. The results are given in Table VI.

For the fin, we shall neglect the moment about its own axis,
any interference effects, and aspect ratio corrections. The upwash
over this idealized fin due to pitching about the hull center of
gravity produces the following derivatives:

$$\left(C_{N_q}{}''\right)_F = \frac{cS}{A}\, 2\pi\left(\frac{.6L}{D}\right) = 5.15 \tag{135}$$

$$\left(C_{m_q}{}''\right)_F = -\left(C_{N_q}{}''\right)_F\left(\frac{.6L}{D/2}\right) = -61.9 \tag{136}$$

The normal force and moment on the fin due to rotation about _its own axis_ are comparatively small and have been neglected here.

Due to $\dot{\alpha}$, there is a normal force on the fin (Section 3.6) given by Equation (166)

$$\frac{N_{F_{\dot{\alpha}}}}{N_{D(P)_{\dot{\alpha}}}} = \frac{2}{\pi}\,\frac{S}{D} = 0.298 \tag{137}$$

thus we find that

$$\left(C_{N_{\dot{\alpha}}}\right)_F = 0.298(0.126) = 0.038 \tag{138}$$

$$\left(C_{m_{\dot{\alpha}}}{}''\right)_F = 0.298(-1.51) = -0.45 \tag{139}$$

The resulting stability derivatives about the hull center of gravity with ducted propeller and fins are tabulated in Table VI for the entire torpedo-like configuration.

The following comments should be made concerning the results summarized in Table VI:

(1) For the hull, both the stabilizing $\dot{\alpha}$ moment and the destabilizing q moment are due entirely to its boundary layer, which has been assumed to remain axially symmetric. For the small oscillations from steady axial flight considered here, these

moments are probably overestimated by this assumption, since the boundary layer oscillation will actually differ from that of the hull.

(2) For the duct, the stabilizing moments about the vehicle center of gravity (with α and q) are due primarily to the normal force which is generated by the upwash over the duct. The moments about the midchord diameter of the duct are negligible in comparison with these moments. In this analysis, however, we have allowed no interference between the hull and ducted propeller, and we have neglected the effect of the hull boundary layer on the propeller since it is reasonably small compared with the duct radius (δ^*_L = 1.34 in., R = 6 in.).

(3) We have assumed an aircraft type propeller (of low solidity with slender blades) which is located near the exit plane of the duct. For such a configuration the only appreciable effects of the propeller are its thrust force and its interference upon the duct. However, small forces and moments are generated on the propeller which are perpendicular to the motion which causes them.

The following conclusions are drawn from Table VI for the overall configuration:

(1) The static stability C_{m_α} " is influenced appreciably by each component; the hull, the ducted propeller, and the fin.

(2) The q damping C_{m_α} " from the ducted propeller and fin are both strongly stabilizing and outweigh the destabilizing effect

of the hull boundary layer, even though this has been overestimated here.

(3) The $\dot{\alpha}$ damping $C_{m_{\dot{\alpha}}}"$ is due almost entirely to the hull boundary layer and has been overestimated here.

(4) The damping in pitch ($C_{m_q}" + C_{m_{\dot{\alpha}}}"$) is stabilizing and is produced mostly by the ducted propeller. The fins provide about 30 percent of the damping and the contribution of the hull is negligible with the boundary layer producing opposite effects on $C_{m_{\dot{\alpha}}}"$ and $C_{m_q}"$.

Now we shall estimate the undamped natural frequency ω_n and the damping ratio ζ_1 (or percent critical damping) for oscillation of the entire configuration, the undamped natural frequency is given by (Eqs. (8-85) , Ref. 10)

$$\omega_n^2 = - C_{m_\alpha}" \left[\frac{q_o A(D/2)}{m_c K_y"^2} \right] \qquad (140)$$

and the damping ratio for impulsive pitch control in steady flight is (Eq. (8-86), Ref. 10)

$$\zeta_1 = \left[C_{N_\alpha} - \left(C_{m_q}" + C_{m_{\dot{\alpha}}}" \right) \frac{(D/2)^2}{2 K_y"^2} \right] \frac{q_o A}{2 m_c V_o \omega_n} \qquad (141)$$

where m_c is the mass of the entire configuration and $K_y"$ is the radius of gyration of entire configuration about the hull center of gravity.

We shall take m_c and $K_y"$ to be those for the hull alone from Appendix E as follows:

$$m_c = \rho \; \text{Vol} = \frac{8}{15} \pi r_m^2 L \rho \qquad (142)$$

$$K_y''^2 = 0.0457 \; L^2 \qquad (143)$$

Substitution of these values and those in Table VI and Figure 4 into Equation (140) yields for the natural frequency

$$\omega_n^2 = - C_{m_\alpha}'' \; \frac{15}{32(0.456)} \left(\frac{V_o}{L} \right)^2 \qquad (144)$$

$$= - 16.4 \; C_{m_\alpha}''$$

$$= 95.0$$

$$\omega_n = 9.75 \; \text{rad/sec} \qquad (145)$$

The undamped period of oscillation is then

$$T = \frac{2\pi}{\omega_n} = 0.66 \; \text{sec} \qquad (146)$$

and the damping ratio is

$$\zeta_1 = \left(C_{N_\alpha} - \frac{C_{m_q}'' + C_{m_{\dot\alpha}}''}{8 \times 4.57} \right) \left(\frac{15}{32} \; \frac{V_o}{L\omega_n} \right)$$

$$= \left(2.91 + \frac{212.3}{8 \times 4.57} \right) \left(\frac{15 \times 4}{15 \times 9.75} \right)$$

$$= 1.67 \qquad (147)$$

so the torpedo is heavily damped.

This ratio is influenced appreciably by each component of the configuration (the hull, the ducted propeller and the fin) as seen from Table VI.

3.5.6 Interference between hull and ducted propeller

In the above calculative example, the stability derivatives of an isolated slender hull were used along with those for an isolated ducted propeller with which it was in thrust equilibrium, $X = T_{D(P)} + T_{P(D)}$. In other words, the mutual interference between the hull and ducted propeller was neglected. To obtain some insight into the order of magnitude of this interference effect, we shall estimate here the thrust interference for steady axial flight. This will be done by:

(1) Assuming the hull drag to be independent of hull shape and given by the flat plate boundary layer of Section 3.5.1 (Eq. (84)).

(2) Approximating the duct bound vorticity distribution (Eq. (A.50)) by the expression

$$\gamma_h = \gamma + 2K_1 \tan \frac{\theta}{2} \tag{148}$$

where γ is the actuator disk vorticity and K_1 is a constant to be determined.

(3) Representing the hull shape by the dividing stream surface about a concentrated point source and sink (Sketch C).

(4) Choosing the value of K_1 such that there is no lateral velocity at the midchord point of the duct.

(5) Solving for the duct thrust from the leading-edge singularity represented by K_1.

In this analysis, the hull shape is allowed to change according to the inflow of the ducted propeller (Sketch D), and the effect of the hull boundary layer entering the ducted propeller will be neglected. Thus, the results will give only an order-of-magnitude estimate of the mutual interference.
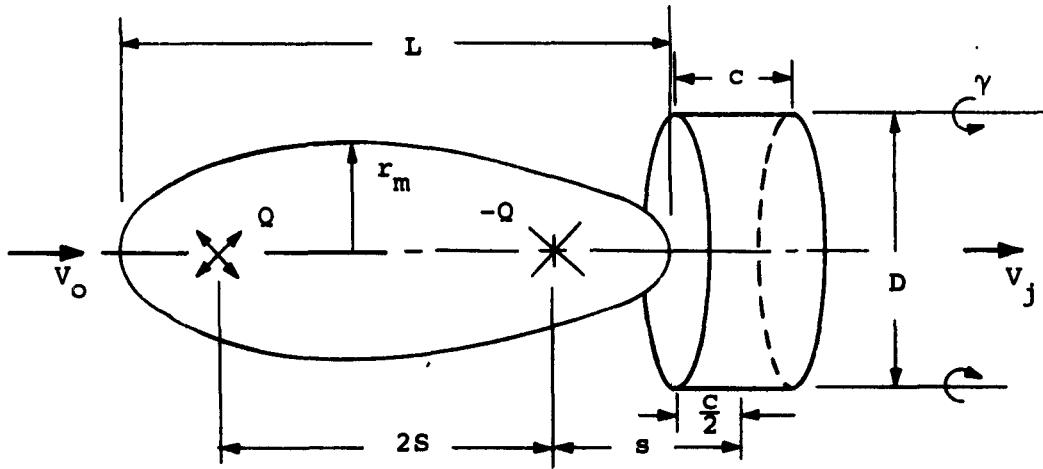
Sketch C. - Hull and ducted-propeller nomenclature.

The above analytical approximations will first be tested by solving for the value of duct thrust $T_{D(P)_a}$ (for the isolated ducted propeller) using the above approximate bound vorticity distribution and comparing this value with $T_{D(P)_e}$ obtained from the more exact theory (Eq. (11)). For the approximate flow model, the duct thrust is found to be expressible as

$$T_{D(P)_a} = \frac{cD}{2} \rho \frac{\gamma^2}{2} \left(\ln \frac{8D}{c} - 2 \right)^2 \qquad (149)$$

and from Equation (11) we have

$$T_{D(P)_e} = \frac{cD}{2} \rho \frac{\gamma^2}{2} \left(\ln \frac{16D}{c} - 2 \right)^2 \qquad (150)$$

For cases in which $c/D < 1/8$, we find that

$$0.89 < \frac{T_{D(P)_a}}{T_{D(P)_e}} < 1 \qquad (151)$$

Thus, the approximate value of duct thrust is reasonably good for very short ducts. Also, the total circulation about the duct chord is found to be within 8 percent of the more exact value for $c/D < 1/8$.

In the absence of the ducted propeller, the hull shape (Ref. 12, p. 461) is axially symmetric and is symmetric fore and aft. Also, for a very slender hull, we have

$$r_m \ll S$$

$$L \simeq 2S$$

and

$$Q \simeq \pi r_m^2 (V_o/2) \qquad (152)$$

In the presence of the ducted propeller, the hull is no longer symmetric fore and aft, but the forward half of the hull is not significantly distorted (see Sketch D). The duct thrust in the

presence of the hull and propeller (as calculated by the method described above) is given approximately by

$$T_{D(HP)_a} \simeq T_{D(P)_a} \left[1 + \frac{\pi \left(V_o/\gamma \right) r_m^2/D^2}{\ln(8D/c) - 2} \right]^2 \qquad (153)$$

where it has been assumed that $s \ll D \ll L$ and $r_m \ll L$. The duct thrust in the presence of the propeller is therefore increased, due to hull interference, by an amount

$$T_{H \rightarrow D(P)} = T_{D(HP)_a} - T_{D(P)_a} \qquad (154)$$

On the other hand, the pressure drag of the hull due to interference from the ducted propeller is found from the Blasius formula (p. 168, Ref. 12) to be

$$X_{D(P) \rightarrow H} = D^2 q_o \frac{\pi r_m^2 \gamma}{2D^2 V_o} \left(\frac{c}{D} \ln \frac{8D}{c} + 1 + \pi \frac{V_o c r_m^2}{\gamma D^3} \right) \qquad (155)$$

Thus we find that the ratio of increased thrust to increased drag is

$$\frac{T_{H \rightarrow D(P)}}{X_{D(P) \rightarrow H}} = \frac{2 \ln(8D/c) - 4 + \pi \left(V_o/\gamma \right) r_m^2/D^2}{\ln(8D/c) + \frac{D}{c} + \pi \left(V_o/\gamma \right) r_m^2/D^2} = 0.78$$

$$(156)$$

and there is a net loss of thrust for the entire configuration due to duct-hull interference. One would expect this effect to be even greater without hull distortion. One can imagine that the interference forces are generated by moving the ducted propeller from far

downstream to a point near the base of the hull as shown in Sketch D. Now, since $T_{H \rightarrow D(P)} < X_{D(P) \rightarrow H}$, the propeller thrust (or γ/V_o) must be increased to maintain thrust equilibrium. If there were no propeller in the duct, that is, if $\gamma = 0$, then the hull and duct interference forces would of course be equal and opposite, but thrust equilibrium would not be possible without the propeller.

$$V_o \qquad \gamma \qquad V_j$$
$$X$$
$$T_{D(P)} + T_{P(D)}$$

$$V_o \qquad \gamma \qquad V_j$$
$$X + X_{D(P) \rightarrow H} \quad T_{D(P)} + T_{P(D)} + T_{H \rightarrow D(P)}$$
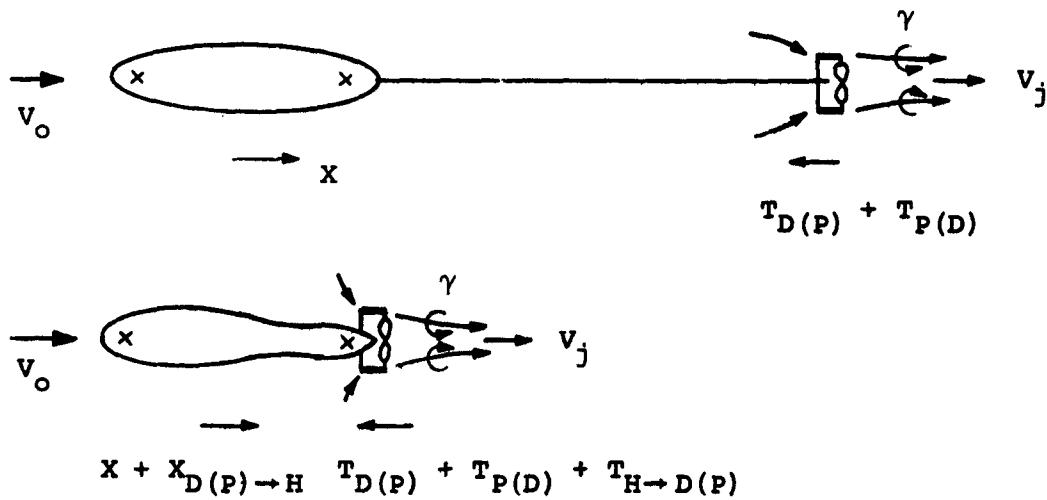
Sketch D - Hull and ducted propeller interference forces.

Using the values estimated in Section 3.5.1 for a different (parabolic) isolated hull shape $\left(\gamma/V_o = 0.050, \ c = 0.2D, \ D = 2r_m, \text{ and } L = 10D \right)$, we find from Equation (153) that

$$T_{D(HP)a} \simeq T_{D(P)a} \left[1 + \frac{\pi}{0.050(4)1.69} \right]^2 = 106 \ T_{D(P)a} \qquad (157)$$

Thus, the approximate duct thrust increases tremendously because of interference with a blunt base hull.[5] However, this is due to the fact that the ducted propeller is very lightly loaded when it is isolated from the hull (far downstream in Sketch D). When they are brought together, the hull induces a large radial velocity component across the duct as compared with the lightly loaded propeller (Sketch D). Thus, the duct thrust due to hull interference is much larger than that required to overcome the hull drag for the present configuration. If the propeller had been more highly loaded so that $\gamma = V_o$ for example, then the duct thrust would have increased by a factor of only 2.15 rather than 106.

The above analysis indicates that large interference effects may exist between the ducted propeller and hull, and that more precise analysis should therefore be made to obtain valid quantitative results. Since both the hull and the propeller induce a radial in-flow which results in a leading-edge suction on the duct, the effect of hull interference on the duct stability derivatives should be similar to the effect of an increase in propeller loading or γ/V_o. One aspect of this observation is that duct shapes which would actually be used in practice to propel hulls with blunt bases would likely have the duct diameter decreasing in the streamwise direction in order to prevent flow separation (in the absence of boundary-layer control). Thus, in view of the large effect of propeller loading on hull-duct interference forces, a reasonable estimate of these interference forces would require that the actual

---

[5] Note that Equation (151) is considerably less accurate for c/D = 0.2 than for c/D ≤ 1/8.

hull and duct shape and the appropriate propeller loading be approximated more closely than is possible within the scope of the present project. This is particularly true for the nonaxial and unsteady flight conditions.

3.6 Comparison of Duct Normal Force with that of an Equivalent Fin

It would be of interest to know whether a ducted propeller is more or less effective in damping than a fin having the same projected area. For this purpose, we shall compare the normal forces on a duct in the presence of a propeller with those on such a fin for small α, q, and $\dot{\alpha}$ motions. The propeller forces themselves are known to be comparatively small (Section 3.4) and will therefore not be considered.

The duct normal force $N_{D(P)}$ predicted in Section 3.1 (Eq. (9)) will be compared with N_F for a fin with chord c and total exposed span D where $c = 0.2D$ for both the duct and the fin. Thus the fin planform is the projected side area of the duct. The fin will be considered as a section of an infinitely long plate; that is, no aspect ratio corrections will be made. For $c = 0.2D$ (aspect ratio of 5) these corrections are small.

First, let us consider the effect of a small angle of attack α_o. For the duct, we have from Equation (9)

$$\left(C_{N_\alpha}\right)_{D(P)} = 1.91 + 0.845 \frac{\gamma}{V_o} \tag{158}$$

and for the fin, using a lift curve slope of 2π, the normal force is

$$N_{F_\alpha} = c D q_o 2\pi \alpha_o \tag{159}$$

Hence

$$\frac{N_{D(P)_\alpha}}{N_{F_\alpha}} = \frac{5}{8}\left(1.91 + 0.845\,\frac{\dot\gamma}{V_o}\right) = 1.19 + 0.528\,\frac{\dot\gamma}{V_o} \tag{160}$$

Thus, even without a propeller $(\gamma = 0)$, we see that N_D is 19 percent greater than N_F. This result is nearly independent of c/D when $c \ll D$ as can be seen from Equations (9) and (159). In Reference 7 an identical expression for N_D is derived for the duct alone $(\alpha = 0)$ and it is shown therein that N_D is exactly twice the lift of a fin of elliptical planform with a total span equal to D and a maximum chord equal to c. Increasing the propeller loading (or γ/V_o) further increases the effectiveness of the ducted propeller over the fin.

Now consider $N_{D(P)}$ due to pitching q about the midchord duct diameter. From Equation (18) we find that

$$\left(C_{N_q}\right)_{D(P)} = \frac{c}{D}\left(\ln\frac{16D}{c} - 1\right)\frac{\gamma}{V_o} + \pi\,\frac{c^2}{D^2} = 0.675\,\frac{\gamma}{V_o} + 0.126 \tag{161}$$

for $c = 0.2D$ and $\alpha_o = 0$.

For the flat fin pitching about its midspan with $\alpha_o = 0$, N_F corresponds to that for an equivalent cambered fin (Sketch A.7) so that the normal force is

$$N_{F_q} = cDq_o 2\pi\alpha'$$ (162)

where

$$\alpha' = \frac{2h}{c} = \frac{cq}{4V_o}$$

Thus, we find for pitching

$$\frac{N_{D(P)_q}}{N_{F_q}} = \frac{\pi}{2} + \frac{D}{2c}\left(\ln\frac{16D}{c} - 1\right)\frac{\gamma}{V_o} = 1.57 + 8.45\frac{\gamma}{V_o}$$ (163)

The increased effectiveness of the ducted propeller over the fin in pitch therefore increases with γ/V_o and decreases with c/D.

Finally, let us consider the normal force due to plunging, $\dot{\alpha} = -\dot{v}/V_o$ at $\alpha_o = 0$. For the duct, we have from Equation (28)

$$(N)_{D(P)_{\dot{\alpha}}} = -\frac{\pi^2 c^2 D}{8}\rho\dot{v}$$ (164)

For the fin, we have from Equation (27)

$$N_F = -\frac{\pi c^2 D}{4}\rho\dot{v}$$ (165)

Thus for any value of c/D

$$\frac{N_{D(P)_{\dot{\alpha}}}}{N_{F_{\dot{\alpha}}}} = \frac{\pi}{2} = 1.57$$

It is therefore concluded that the duct normal force due to α, q, and $\dot{\alpha}$ is larger than the fin normal force for all values of c/D and γ/V_o. Furthermore, the effectiveness with q and α increase as the propeller loading is increased.

4. COMPARISON OF EXPERIMENTAL DATA AND THEORY

4.1 Introduction

In this section, the predicted forces and moments on the duct in the presence of the propeller will be compared with every known source of applicable ducted propeller data. The sources of data will be selected from the references listed, which are summarized in Reference 2. We shall use only the data for which the forces and moments on the propeller and on the duct were measured independently and where the duct was reasonably short, straight, and thin as assumed in the present theory. Wherever a choice is possible, only the shortest duct tested will be considered here. Most of these data are for steady hovering flight or for axial flow, in which case only thrust forces exist on the duct and propeller and for which the theory predicts only the duct thrust coefficient in terms of the propeller thrust coefficient.

Two sources of data for steady flow at angle of attack (Refs. 13 and 14) will be used for comparison with the predicted normal force coefficient of the duct, but only one of these (Ref. 13) contains measurements of the duct pitching moment coefficient which will also be compared. The most recent ducted propeller data at angle of attack (Ref. 15) will not be used here, because tne duct chord to diameter ratio (c/D = 0.61) was not small as assumed in the present theory.

The only known source of dynamic data (Ref. 16) will not be used here for comparison, because the ducted propeller was mounted

near a large hull and only the forces and moments on the entire
configuration were measured. Since the hull interference and
boundary-layer effects upon the ducted propeller were probably not
small enough to neglect, it does not appear worthwhile to attempt
the extraction of isolated ducted propeller data from these measure-
ments. Thus no dynamic data will be compared with the theory.

Even for the data which are used, the validity of the compar-
ison with the present theory is questionable because of one or
more of the following factors:

(a) Flow separation from the duct inlet

(b) Duct chord/diameter ratio too large

(c) Nonuniform propeller loading

(d) Slipstream swirl generated by a single propeller

(e) Too much duct taper

(f) Large centerbody

The present theory predicts the forces and moments on the
duct in the presence of the propeller by representing the propeller
as a uniformly loaded actuator disk. The duct force and moment
coefficients, $C_{T_{D(P)}}$, $C_{N_{D(P)}}$, and $C_{m_{D(P)}}$, are predicted as
functions of the independent variables α_0, c/D, and γ/V_0. There-
fore, in order to predict the duct data for a given test, we must
first express γ/V_0 in terms of the measured data. For the ideal,
uniformly loaded actuator disk and the corresponding ideal slip-
stream with constant velocity V_j and no swirl, this is done quite
simply by use of Bernoulli's equation far ahead and behind the

propeller disk. However, this model is evidently too idealized

for a satisfactory comparison of theory and experiment. Therefore,

in order to improve the comparison of the present theory with data

for real propellers, we shall now consider real slipstream effects.

These can be catagorized as:

    (a)   Slipstream swirl generated by the propeller

    (b)   Nonuniformity of the jet velocity component V_j, which is
           aligned with the axis of the slipstream (Fig. 6)

    (c)   Frictional losses which appear as propeller blade wakes

Dual, counter-rotating propellers or propeller-stator combina-

tions are seldom used in the data described below. When such com-

binations are used, the slipstream swirl should be comparatively

small compared with that for a single propeller.

For the purpose of improving the comparison of the present

theory with experimental data, the data will be selected for com-

binations of blade pitch β and advance ratio λ for which the

real slipstream effects are minimum. A method for accomplishing

this end will be described below, and the real slipstream effects

upon the present theory will be discussed. The purpose of the latter

discussion is to give some insight into how the predicted duct

coefficients are influenced, but no attempt is made to give quanti-

tative predictions of real slipstream effects.

4.2 Data Reduction Method

The present theory predicts the forces and moments on the duct

in the presence of a propeller by representing the propeller as a

uniformly loaded actuator disk, and the propeller slipstream vorticity, γ/V_0 in Figure 2, is the only direct effect of the propeller which appears in the analysis. The purpose of this section is to develop expressions for γ/V_0 in terms of the propeller coefficients which are usually measured in experimental investigations.

First, we shall retain the assumption of an ideal actuator disk and find γ/V_0 in terms of the propeller disk loading $C_{T_{P(D)}}$. Then we shall include two real propeller slipstream effects, the swirl and the blade wake frictional losses, and derive a second expression for γ/V_0. The purposes of the second derivation are to demonstrate: (1) a method for selecting data which minimizes the real slipstream effects, and (2) the way in which real slipstream effects influence the predicted duct forces and moments.

4.2.1 Evaluation of γ/V_0 for an Actuator Disk

The diameter of the actual stream tube flowing through the ducted propeller at angle of attack changes continuously as shown in Figure 6. However, the duct forces and moments have been predicted by assuming that the slipstream vorticity γ could be put on the dashed cylindrical surface of diameter D. In the actual slipstream, there is a counter-rotating swirl distribution due to the cross flow of the free stream over it (Fig. 6). This swirl distribution (which is generated by the trailing vortex filaments in the duct wake $d\Gamma_{\alpha_w}$ in Fig. 2) is already incorporated in the present analysis. The kinetic energy associated with this swirl distribution causes an induced drag due to lift, which appears in

the calculated duct thrust and duct normal force. However, since
we have assumed that the cross flow is small ($V_o \sin \alpha_o \ll V_j$),
we shall neglect the swirl velocity component in evaluating the
total pressure rise across the actuator disk. Thus, we can write
Bernoulli's equation ahead of and behind the propeller disk as

$$\Delta p = \frac{\rho}{2} \left(V_j{}^2 - V_o{}^2 \right) \tag{167}$$

so that

$$C_{T_{P(D)}} = \frac{T_{P(D)}}{Aq_o} = \left(\frac{V_j{}^2}{V_o{}^2} - 1 \right) \tag{168}$$

Furthermore, since $\alpha_j \ll \alpha_o$ in Figure 6, we can write

$$\gamma = V_j - V_o \cos \alpha_o \tag{169}$$

Thus, by equating the two expressions for V_j given by Equations
(168) and (169), we can evaluate the propeller slipstream vorticity
in terms of the propeller thrust coefficient as

$$\frac{\gamma}{V_o} = \sqrt{C_{T_{P(D)}} + 1} - \cos \alpha_o \tag{170}$$

For the special case of hovering flight, Equation (15) replaces
Equation (170).

4.2.2 Real slipstream effects and data selection procedure

The above evaluation of γ/V_o assumes that the slipstream
is ideal; that is, the propeller is an actuator disk, which is
uniformly loaded so that it generates no swirl, the slipstream
velocity V_j is constant, and there are no frictional losses

(blade wakes). Here we shall evaluate γ/V_o with these real slip-stream effects included insofar as possible within the context of the present theory. To do this, we shall first assume that the actuator disk adds angular as well as axial momentum to the slip-stream as shown in Figure 6.

To account for the swirl qualitatively, we shall assume that far downstream, at station j, the slipstream or jet rotates as a solid body with a swirl velocity component

$$V_S = \frac{r_j}{r_{j_m}} V_{S_m} \tag{171}$$

The additional vorticity shed by the propeller to produce this swirl is a uniform distribution of axial vortex filaments within the jet and a uniform distribution of filaments of opposite sign along the jet boundary. Within the context of the present theory, the effect of this vorticity upon the duct is found by placing the slipstream on the dashed cylindrical extension of the duct, as indicated in Figure 6. It can be shown that when this is done the additional vorticity induces no velocity outside of the semi-infinite dashed cylinder. Thus, the equations for the duct force and moment coefficients given by the present theory in terms of γ/V_o are not affected by the additional vorticity due to solid body rotation of the slipstream.

The theory assumes that the slipstream vorticity γ, associated with the velocity component V_j aligned with its axis, is concentrated along the jet surface. Thus, within the framework of this

theory, we must retain the assumption that V_j is constant. How-
ever, for single propellers operating at peak efficiency, the net
effect of propeller swirl V_s is probably larger than the non-
uniformity of V_j. Hence, we can account for the dominant real
effect.

With this representation of the propeller slipstream, the
propeller disk loading Δp is no longer uniform, since the total
pressure in the slipstream is not constant. We shall now assume
that, in addition to imparting axial and angular momentum and
energy to the slipstream, the propeller introduces frictional
losses in the form of blade wakes. The head loss H_l associated
with these wakes causes an increase in propeller power. However,
we shall assume that the wakes mix rapidly and that the head loss
is distributed uniformly within the slipstream. Thus, there is
no vorticity far downstream associated with H_l and no effect upon
the duct or propeller forces. The only effect of H_l then is to
increase the propeller torque and power.

Steady Flight at Angle of Attack

Now let us consider the angular momentum, the power, and the
thrust associated with the slipstream swirl V_s. For a single
propeller and no stator, we can equate the propeller torque to the
angular momentum of the jet, since $\alpha_j \ll 1$ (Fig. 6). Thus, we
have

$$\left. \begin{aligned} \tau &= \int_{A_j} r_j V_S \rho V_j \, dA_j \\ &= 2\pi \rho V_j V_{S_m} r_{j_m}^{\,3} \int_0^1 \frac{r_j^{\,2}}{r_{j_m}^{\,2}} \frac{V_S}{V_{S_m}} \, d \frac{r_j}{r_{j_m}} \\ &= A_j \frac{r_{j_m}}{2} \rho V_j V_{S_m} = W_j \frac{r_{j_m}}{2} V_{S_m} \end{aligned} \right\} \qquad (172)$$

where the mass flow rate in the slipstream is

$$W_j = \rho A_j V_j \qquad (173)$$

For dual propellers, or propeller-stator combinations, τ is the net torque on the combination.

The steady-flow energy equation for the stream tube in Figure 6 (between stations far upstream and far downstream) can be written as

$$P = \int_{A_j} \left(\frac{p}{\rho} + \frac{V_j^{\,2} + V_S^{\,2}}{2} \right) \rho V_j \, dA_j - W_j \left(\frac{p_o}{\rho} + \frac{V_o^{\,2}}{2} - \frac{H_l}{\rho} \right) \qquad (174)$$

where P is the power supplied to the propeller and H_l/ρ is the frictional head loss due to blade wakes. In Equation (174), we have neglected the comparatively small swirl velocity component in the jet which is induced by the duct trailing vorticity (see Fig. 6) just as we did previously in calculating Δp across the actuator disk (see Eq. (167)).

Let us now find the variation of static pressure across the jet so that we can evaluate Equation (174). This can conveniently be done in a coordinate system which translates along the jet with velocity V_j. In this coordinate system, we can write

$$\frac{\partial p}{\partial r_j} = \rho \frac{V_s^2}{r_j} \tag{175}$$

Making use of Equation (171), we find by integration that

$$P_o - P = \frac{\rho}{2}\left(V_{s_m}^2 - V_s^2\right) = \frac{\rho}{2} V_{s_m}^2 \left(1 - \frac{r_j^2}{r_{j_m}^2}\right) \tag{176}$$

Substitution into Equation (174) then gives

$$P = 2\pi\rho V_j r_{j_m}^2 \int_0^1 \left(\frac{P_o}{\rho} + \frac{V_j^2}{2} - \frac{V_{s_m}^2}{2} + V_{s_m}^2 \frac{r_j^2}{r_{j_m}^2}\right) \frac{r_j}{r_{j_m}} \, d\frac{r_j}{r_{j_m}}$$

$$- W_j \left(\frac{P_o}{\rho} + \frac{V_o^2}{2} - \frac{H_\perp}{\rho}\right) \tag{177}$$

and upon integration over the jet, we find that

$$P = \tau\omega = \frac{W_j}{2}\left(V_j^2 - V_o^2 + 2\frac{H_\perp}{\rho}\right) \tag{178}$$

where $\tau\omega$ is summed for the propellers if there are more than one. Thus, the propeller power is increased by an amount

$$W_j \left(\frac{H_\perp}{\rho}\right)$$

due to swirl and blade wakes.

Now let us find the effect of V_S upon the total thrust force of the ducted propeller, $T_{D(P)} + T_{P(D)}$. We can write the momentum equation along the duct axis, for a large control surface surrounding Figure 6, as

$$T_{D(P)} + T_{P(D)} = W_j \left(V_j \cos \alpha_j - V_0 \cos \alpha_0 \right) - \cos \alpha_j \int_{A_j} (p_0 - p) \, dA$$

$$(179)$$

Substitution of Equation (176) and use of $\cos \alpha_j \approx 1$ then gives

$$T_{D(P)} + T_{P(D)} = W_j (V_j - V_0 \cos \alpha_0) - \rho V_{S_m}^2 A_j \int_0^1 \left(1 - \frac{r_j^2}{r_{j_m}^2} \right) \frac{r_j}{r_{j_m}} \, d \frac{r_j}{r_{j_m}}$$

$$(180)$$

$$T_{D(P)} + T_{P(D)} = W_j \left(V_j - V_0 \cos \alpha_0 - \frac{V_{S_m}^2}{4V_j} \right) \qquad (181)$$

so that the total thrust is reduced by an amount

$$W_j \left(\frac{V_{S_m}^2}{4V_j} \right)$$

due to swirl. Now we shall combine Equations (172), (178), (180), and (181), and put the results in dimensionless coefficient form. Thus, equating the two expressions for τ as given by Equations (172) and (178) yields for a single propeller

$$\frac{r_{j_m}}{R} \frac{\omega R}{V_0} \frac{V_{S_m}}{V_0} = \frac{V_j^2}{V_0^2} - 1 + 2 \frac{H_1}{\rho V_0^2} \qquad (182)$$

Division of Equation (181) by (178) gives a propulsive efficiency defined as

$$
\eta_P \equiv \frac{T_{D(P)} + T_{P(D)}}{P} V_o = 2 \frac{\dfrac{V_j}{V_o} - \cos \alpha_o - \dfrac{V_{s_m}^2}{4V_o^2} \dfrac{V_o}{V_j}}{\dfrac{V_j^2}{V_o^2} - 1 + 2 \dfrac{H_1}{\rho V_o^2}}
\tag{183}
$$

and the total thrust coefficient of the ducted propeller is, from Equation (181)

$$
C_{T_{DP}} \equiv \frac{T_{D(P)} + T_{P(D)}}{A q_o} = 2 \frac{\bar{V}}{V_o} \left(\frac{V_j}{V_o} - \cos \alpha_o - \frac{V_{s_m}^2}{4 V_o V_j} \right)
\tag{184}
$$

where $\bar{V}$ is the averaged axial velocity component through the duct, given by

$$
\bar{V} = \frac{1}{A} \int_A V \, dA
$$

In addition to the above set of equations, we can write from continuity

$$
\frac{r_{j_m}}{R} = \sqrt{\frac{\bar{V}}{V_o} \frac{V_o}{V_j}}
\tag{185}
$$

and, from Figure 6, (where $\alpha_o \gg \alpha_j \approx 0$)

$$
\frac{\gamma}{V_o} = \frac{V_j}{V_o} - \cos \alpha_o
\tag{186}
$$

Thus, we have a set of five equations, (182) through (186), for the six dimensionless unknowns

$$\frac{r_{j_m}}{R} \; , \; \frac{V_{S_m}}{V_o} \; , \; \frac{V_j}{V_o} \; , \; \frac{H_l}{\rho V_o^2} \; , \; \frac{\bar{V}}{V_o} \; , \; \frac{\gamma}{V_o}$$

in terms of three measured coefficients

(a) Propeller advance ratio, $\lambda = V_o/\omega R$

(b) Propulsive efficiency, η_p

(c) Total thrust coefficient, $C_{T_{DP}}$

We could solve this set of equations by using the present theory to evaluate $\bar{V}/V_o$ in terms of c/D and γ/V_o. For example, Figure 3(a) gives values of $\bar{V}/\gamma$ for hovering flight and for $c = 0.2D$. For axial forward flight, $\bar{V}$ is simply increased by V_o. The present theory also gives the thrust ratio

$$\frac{T_{D(P)}}{T_{P(D)}} \left(\frac{c}{D} \; , \; \frac{\gamma}{V_o} \; , \; \alpha_o \right) = \frac{C_{T_{D(P)}}}{C_{T_{P(D)}}} \tag{187}$$

so that either of these thrust coefficients could be used instead of $C_{T_{DP}}$ in Equation (184). However, our purpose here is to find an independent expression for γ/V_o in terms of measured coefficients to supplement the present theory. Therefore, we shall drop $H_l/\rho V_o^2$ in Equation (183), assuming it to be zero, rather than use the present theory to evaluate $\bar{V}/V_o$.

It should be noted that the coefficients $C_{T_{DP}}$ and η_P used above are related to the torque coefficient C_Q and the power coefficient C_P as follows:

$$C_Q = \frac{\tau}{A q_o R} = \frac{\lambda C_{T_{DP}}}{\eta_P} = f\left(\frac{\bar{V}}{V_o}, \frac{V_{S_m}}{V_o}, \frac{r_{j_m}}{R}\right) \tag{188}$$

$$C_P = \frac{\tau \omega}{A q_o V_o} = \frac{C_Q}{\lambda} \tag{189}$$

Axial Flight

If we now restrict the angle of attack α_o to zero and eliminate V_{S_m}/V_o, r_{j_m}/R, and γ/V_o with Equations (183), (185), and (186), respectively, then we can write the remaining Equations (182) and (184) in the form

$$\frac{\bar{V}}{V_o} = \frac{\lambda^2/4}{\left[1 - \frac{\eta_P}{2}\left(\frac{V_j}{V_o} + 1\right)\right]} \frac{\left(\dfrac{V_j^2}{V_o^2} - 1\right)^2}{\dfrac{V_j}{V_o} - 1} \tag{190}$$

and

$$\frac{\bar{V}}{V_o} = \frac{C_{T_{DP}}}{\eta_P} \frac{1}{\left(\dfrac{V_j^2}{V_o^2} - 1\right)} \tag{191}$$

Then, elimination of $\bar{V}/V_o$ gives the expression

-81-

$$\frac{4C_{T_{DP}}}{\lambda^2 \eta_P} = \frac{\left(\dfrac{V_j}{V_o} - 1\right)^2 \left(\dfrac{V_j}{V_o} + 1\right)^3}{\left[1 - \dfrac{\eta_P}{2}\left(\dfrac{V_j}{V_o} + 1\right)\right]} \tag{192}$$

if $H_l = \alpha_o = 0$. From Equation (186) with $\alpha_o = 0$, we have

$$\frac{\gamma}{V_o} = \frac{V_j}{V_o} - 1 \tag{193}$$

Thus, Equations (192) and (193) give the propeller vorticity γ/V_o in terms of three measured coefficients $(C_{T_{DP}}, \eta_P, \text{and } \lambda)$ for the case in which the angle of attack and propeller frictional losses are zero.

To illustrate the effect of swirl, we shall use Equation (192) for γ/V_o with one source of experimental data (Ref. 19) for comparison with Equation (170). However, in general, we shall use Equation (170) to evaluate γ/V_o. We shall do this for selected values of λ and β which minimize the real slipstream effects. From Equations (170) and (183) it can be seen that, for fixed values of α_o and $C_{T_{D(P)}}$ (or V_j/V_o), these effects (as represented by V_S and H_l) are minimum when η_P is maximum. It is noted in Equation (183) that both propeller swirl and frictional losses tend to decrease η_P as would be expected from physical reasoning for axial flow. It should be recalled that Equation (183) is based upon the following assumptions:

(1) V_j is constant and $\alpha_j \approx 0$

(2) The jet slipstream rotates as a solid body

(3) The frictional head loss is uniformly distributed over the jet

Using the above results, we shall select combinations of λ and β for which η_P is a maximum for a fixed value of $C_{T_{P(D)}}$. Since ducted propeller data are usually presented in terms of λ and β , this will be done by use of data plots as shown below for a fixed angle of attack.
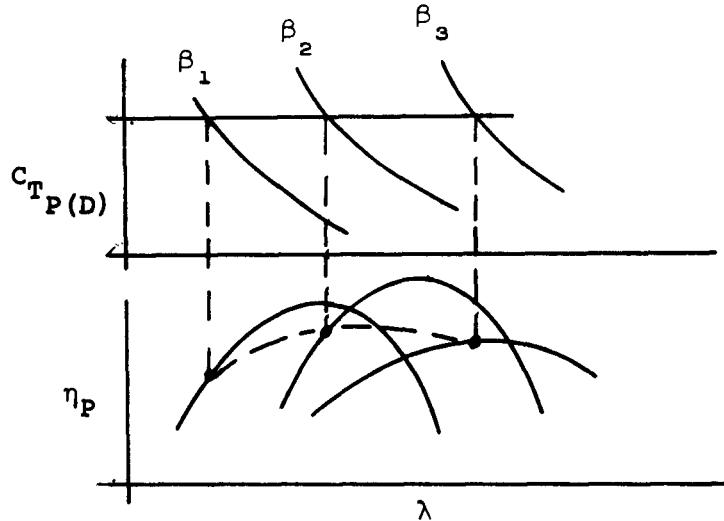
Sketch E.- Example data plots.

It can be seen that the combination of λ and β for maximum η_P with $C_{T_{P(D)}}$ fixed cannot be obtained by the usual procedure of maximizing η_P with either β or λ held constant.

Hovering Flight

Carrying through the above analysis for hovering flight $(V_o = 0)$, with the appropriate definitions based on V_j rather then V_o, we find instead of Equations (183) and (192)

$$\eta_h \equiv \frac{T_{D(P)} + T_{P(D)}}{P} \frac{V_j}{2} = \frac{1 - \dfrac{V_{S_m}^{\,2}}{4V_j^{\,2}}}{1 + \dfrac{2H_l}{\rho V_j^{\,2}}} \qquad (194)$$

and

$$\left(\frac{V_j}{\omega R}\right)^4 = \frac{2\left(1 - \eta_h\right)}{\eta_h} \frac{T_{D(P)_h} + T_{P(D)_h}}{A\left(\dfrac{\rho}{2}\,\omega^2 R^2\right)} \qquad (195)$$

It can be seen that η_h is maximum for minimum swirl and minimum frictional loss and that η_h could be evaluated from Equation (194) by use of measured data and Equation (195) to eliminate V_j. However, η_h is the "compressor efficiency" which is customarily defined as

$$\eta_h \equiv \frac{T_{D(P)_h} + T_{P(D)_h}}{P} \sqrt{\frac{T_{P(D)_h}}{2\rho A}} \quad \text{for} \quad V_{S_m} = H = 0 \qquad (196)$$

by neglecting swirl and evaluating V_j from the Bernoulli Equation (15). We shall retain this system for evaluating η_h. It can then be shown that

$$\eta_h = \frac{M_h}{\sqrt{\dfrac{T_{D(P)_h}}{T_{P(D)_h}} + 1}} \quad \text{for} \quad V_{S_m} = H_l = 0 \qquad (197)$$

where M_h is the usual figure of merit for hovering flight as defined in the List of Symbols. Now, to select hovering data for which the swirl and head loss are minimum, the value of β will be chosen which gives a maximum value of η_h as defined in Equation (197). For no swirl, we have the ideal case of

$$\eta_h \rightarrow 1 \quad \text{and} \quad M_h \rightarrow \sqrt{\frac{T_{D(P)_h}}{T_{P(D)_h}} + 1} \tag{198}$$

For a very long duct, simple momentum theory gives $T_{D(P)_h} \rightarrow T_{P(D)_h}$, and Equation (198) then gives for $c \gg D$

$$\eta_H \rightarrow 1 \quad \text{and} \quad M_h \rightarrow \sqrt{2} \tag{199}$$

Pitching or Plunging Flight

For either pitching or plunging flight, the same procedure of data extraction as outlined above for steady flight at angle of attack will be used for small pitching and plunging rates. At the present time, however, no applicable dynamic data are available for comparison with the theory.

4.3 Thrust Ratio in Hovering and Axial Flight
Hovering Flight

The division of thrust in hovering flight as predicted by theory (Eq. (17)) is

$$\left(\frac{T_{D(P)}}{T_{P(D)}}\right)_h = \frac{2c}{\pi D}\left(\ln\frac{16D}{c} - 2\right)^2 \tag{200}$$

This expression is plotted in Figure 7 and is compared with six sources of data chosen from Table I of Reference 2. The asymptotic value for large chord (Eq. (199)) is also shown. Equation (200) is based upon the assumption that $c \ll D$. However, this assumption does not introduce much error into the approximate expressions for the velocity induced by the actuator disk if $c \leq (D/4)$ (see Eq. (A.12)). Furthermore, the additional approximation that the flow is two dimensional over each chordwise strip of the duct is expected to be reasonably accurate if $c \leq (D/4)$. Therefore, we expect Equation (200) to be valid within this range as indicated by the solid line in Figure 7.

Data by Gill

Shown in Figure 7(a) are data by Gill taken from Figures 25, 26, and 28 of Reference 13 for three duct shapes designed at Hiller Aircraft Corp. These ducts were all relatively straight, thin, and short and had an inside diameter of 24 inches as indicated. The ducts were used with counter-rotating propellers, each having three twisted and tapered blades with only 0.04-inch clearance between the blade tips and the inner surface of the duct. The thrust ratio was found to depend only very slightly on the mean blade pitch setting β, as shown in Figure 7(a). With independent variation of β, neither the figure of merit

$$M_h \equiv \frac{T_{D(P)_h} + T_{P(D)_h}}{P} \sqrt{\frac{T_{D(P)_h} + T_{P(D)_h}}{2\rho A}} \qquad (201)$$

nor the compressor efficiency

$$\eta_h \equiv \frac{T_{D(P)_h} + T_{P(D)_h}}{P} \sqrt{\frac{T_{P(D)_h}}{2\rho A}} \qquad (202)$$

was a maximum when the thrust ratio $T_{D(P)}/T_{P(D)}$ was maximum, as
can be seen from the data of Figure 7(a). This behavior is believed
to be associated with flow separation from the duct leading edge,
which was actually observed during hovering flight for all the
duct shapes except for one having a large inlet lip radius.
Because of this fact, it is not surprising that the measured thrust
ratio was only about half of that calculated. That is, the thrust
carried by the duct was evidently greatly diminished by flow separa-
tion from the duct leading edge.

Data by Horn

Shown in Figure 7(b) is a datum point by Horn taken from Fig-
ure 13 of Reference 17. The configuration was of the shape indicated
and was tested in water. A single propeller with four blades was
used without a stator, so that swirl was introduced into the slip-
stream. Furthermore, the duct is too long for comparison with the
theory, and the blade-pitch angle was not varied. Propeller loca-
tion was varied in a still longer duct (which is therefore not
shown in the figure) and there was little effect of propeller
location upon either $T_{P(D)_h}$ or $T_{D(P)_h}$.

Data by Moser

Also shown in Figure 7(a) are data by Moser, taken from Figure 12(b) of Reference 18. The duct shape was varied by adding a sheet-metal ring after the duct, as indicated, such that

$$0.33 \leq \frac{c}{D} \leq 0.89$$

It was found that the thrust ratio was virtually invariant with duct length as indicated by the arrow in the figure. The single propeller had two blades. The blade pitch was not varied, and stators were not used.

Data by Kruger

Finally shown in Figure 7(b) are data by Kruger, taken from Figure 21 of Reference 19 for one of fifteen shroud shapes tested with a relatively large centerbody. The duct shape used here had the smallest camber, thickness, and chord-to-diameter ratio of all the ducts tested therein. A single propeller with eight blades and no stator was used with this duct, and the blade-pitch setting β was varied independently. It can be seen that the thrust ratio in this case was very dependent upon β and again was not maximum for peak efficiency (either M_h or η_h). These peaks occurred at the lowest blade-pitch angle which was tested, namely 15°. However, it can be seen from the measured values of duct and propeller thrust in Figure 21 of Reference 19 that both the propeller and the duct were stalled at the higher pitch angles, so that the measured thrust ratio at high β is not actually

comparable with the theory. For a longer, thicker, converging

shroud, hovering thrust ratios as great as two were obtained.

However, the duct length, c = 0.625D, and convergence were too

large for comparison with the present theory.

Data by Grose

Shown in Figure 7(c) are data by Grose, taken from Figures 18

to 21 of Reference 14. The shroud shown in Figure 7(c) (Grose's

"high-speed" shroud), was relatively thin and straight, as indi-

cated; however, it was rather long for comparison with the present

theory (c = 0.475D). The flow was observed to separate from the

leading edge and to reattach near the trailing edge of this duct

during hovering. The variation of thrust ratio $T_{D(P)_h}/T_{P(D)_h}$

with blade pitch is shown in Figure 7(c). In this case M_h, η_h,

and $T_{D(P)_h}/T_{P(D)_h}$ were all maximum for $\beta = 15°$. A second

"static" shroud, designed with a large radius inlet lip to prevent

separation, had thrust ratios as large as unity. Both ducts were

tested with a single propeller having four blades and no stators.

Propeller tip speeds were between 500 and 1200 feet per second

during these tests.

Data by Platt

Also shown in Figure 7(c) are data by Platt, taken from Figure 19

of Reference 20 for the shortest of three ducts tested. This duct

was tested with counter-rotating propellers with blade tip speeds

between 400 and 600 feet per second. The front propeller had five

blades and the rear seven blades. The variation of thrust ratio

with blade pitch is indicated in Figure 7(c). Here M_h, η_h, and
$T_{D.(P)_h}\big/T_{P(D)_h}$ were all highest for the highest pitch angle tested,
namely $\beta = 45^\circ$. It will be noted that the values of $T_{D(P)_h}\big/T_{P(D)_h}$
measured by Platt were far in excess of the values predicted either
by the present theory or by simple momentum theory. However, neither
of these theories is expected to be valid for this intermediate range
of c/D (c = 0.67D). Thus, the need for a theory in the intermediate
range of chord-to-diameter ratio is readily apparent.[6]

Flow separation and high noise level were observed by Platt only
at low propeller speed with this duct. At the higher rotational speeds
tested (corresponding to the data shown in Fig. 7(c)), the flow was
attached and the duct thrust was about twice as great as for separated
flow. This configuration is the only one known for which the duct
was essentially straight and thin and for which the flow was known to
be unseparated in hovering. The fact that the Grose duct was always
stalled and the Platt duct generally unstalled during hovering tests
apparently was not due to Reynolds number, because the maximum Reynolds
numbers based on tip speed and chord length were nearly equal for the
two cases.

Axial Flight

The thrust ratio for axial flight can be written (from Eqs. (11),
(168), (169), and (200)) as

$$\frac{T_{D(P)}}{T_{P(D)}} = \frac{\frac{2c}{\pi D}\left(\ln\frac{16D}{c} - 2\right)^2}{1 + 2\frac{V_o}{\gamma}} = \frac{\left(T_D/T_P\right)h}{1 + 2\frac{V_o}{\gamma}} \qquad (203)$$

---

[6]Subsequent analysis has shown that for hovering flight the theoretical
thrust ratio is greater than unity for the intermediate range of c/D.

Thus, the thrust ratio in axial flow is evidently given by the value for hovering divided by $1 + 2(V_o/\gamma)$. Furthermore, the ratio V_o/γ is a function only of the actuator disk loading when there are no real slipstream effects. That is, Equations (169) and (170) give (for $\alpha_o = 0$)

$$\frac{V_j}{V_o} = \frac{\gamma}{V_o} + 1 = \sqrt{C_{T_{P(D)}} + 1} \qquad (204)$$

Thus, Equations (203) and (204) give the predicted thrust ratio in terms of c/D and the measured propeller thrust coefficient. This predicted value will now be compared with five sources of measured data. The data will be restricted, whenever possible, to those combinations of propeller advance ratio $\lambda = V_o/\omega R$, and blade-pitch setting β which give maximum propulsive "efficiency,"

$$\eta_P = \frac{\left[T_{D(P)} + T_{P(D)} \right] V_o}{P} \qquad (205)$$

with fixed propeller loading $C_{T_{P(D)}}$. This combination should minimize the real slipstream effects (see Section 4.2) which have been assumed to be zero in the present theory. Thus, the predicted value of propulsive efficiency (Eq. (183)) with $V_{S_m} = H_l = 0$) is the "ideal Froude efficiency."

$$\eta_P = \frac{2}{\frac{V_j}{V_o} + 1} \qquad (206)$$

Data by Gill

Of the three Hiller ducts shown in Figure 7(a), only $D_4 P_3 S$ was tested in axial flight. Measured values of η_p and values of V_j/V_o calculated from Equation (204) are plotted in Figure 8, using data from Figures 178 and 179 of Reference 13, and the method of data selection is indicated in Figure 8 for values of V_j/V_o of 1.75, 2.0, and 3.5.

For the values of V_j/V_o indicated in Table VII, this procedure (λ and β in each case selected for the highest value of η_p) gives the results shown therein. The values of V_j/V_o in Figure 8 differ from those in Table VII because the former were chosen to illustrate that β varies with V_j/V_o for maximum η_p. The measured values of η_p in Table VII are considerably smaller than the predicted ideal Froude efficiency (Eq. (206)). Therefore, real slipstream effects are probably not negligible as assumed in the above comparison of data and theory.

It was not reported in Reference 13 whether this duct was stalled at the above test conditions, but it was observed to be stalled during hovering. Therefore, the low values of measured thrust ratio as compared with theory could be due to flow separation and/or real slipstream effects.

Data by Horn

The duct shape of Horn, shown in Figure 7(b), was also tested in axial flow, and the values in Table VIII were obtained from Figure 13, Reference 17, by the method described above.

As indicated in Figure 7(b), this duct is actually too long for accurate prediction of the thrust ratio by the present theory. A single propeller was tested with β fixed. The axial flight data indicate a wide variation of thrust ratio with advance ratio. At the advance ratio for which η_p was highest, there is little difference between the small values of measured and predicted thrust ratio. Real slipstream effects were probably large, since η_p as measured was much smaller than the predicted ideal Froude efficiency.

Data by Allen

In Reference 21, data are presented for axial-flow tests of two-bladed propellers with and without a duct. Three different propellers were used which had pitch settings, β = 20°, 25°, and 30°. The duct shape, propeller location, and tip clearance are indicated in Sketch F, below.
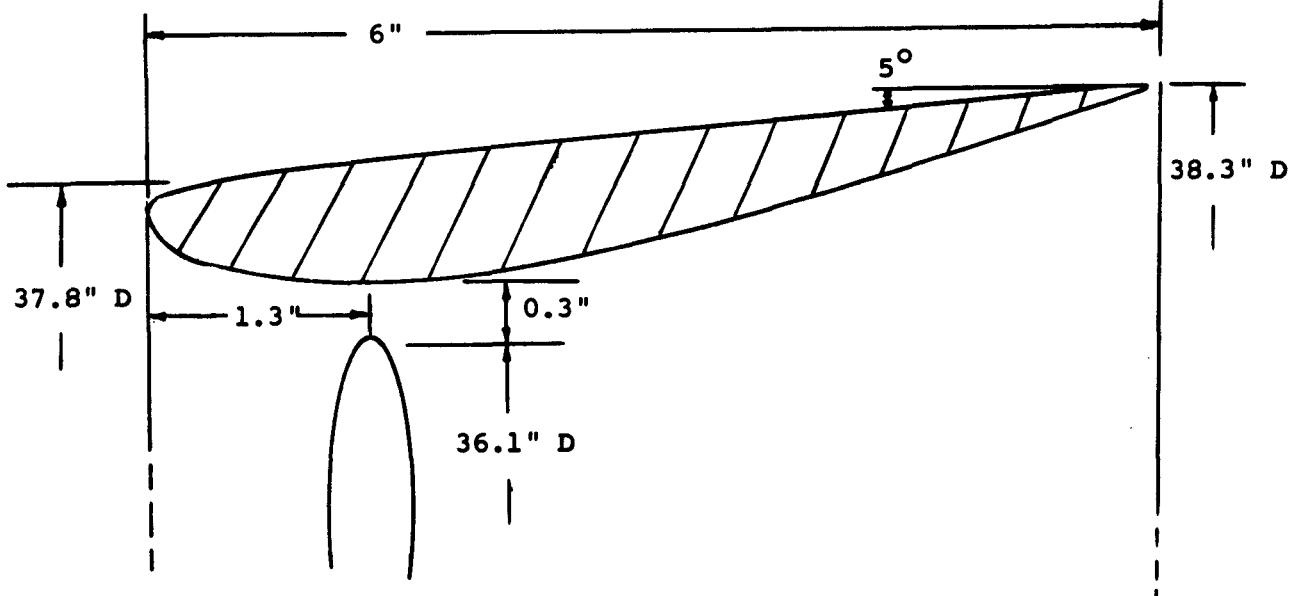
Sketch F.- Ducted-propeller configuration
tested by Allen (Ref. 21).

It can be seen that more duct divergence and "internal diffusion" were incorporated into this configuration than in those of Figure 7.

From a plot of measured data (taken from Fig. 2, Ref. 21) similar to Figure 8, the values in Table IX were obtained for maximum η_p at the selected values of $C_{T_{P(D)}}$.

Both the measured pressure distribution over this duct surface and the good agreement between the measured values of duct thrust and those predicted by the approximate potential flow analysis (of Ref. 21), indicate that this duct was not appreciably stalled during high-speed forward flight with any of the three propellers tested. However, the measured value of $T_{D(P)}$ gradually increased and then suddenly dropped appreciably when V_o/nD was decreased to values slightly less than those corresponding to the data used above. It is therefore concluded that the duct was not stalled for the data used above. At high advance ratios, $T_{D(P)}$ became negative due to the large external duct divergence and friction drag. Negative values of $T_{D(P)}$ also were measured without the propeller. It is observed that high values of η_p were attained and that the measured thrust ratio for $\beta = 25^{\circ}$ is greater than the predicted ratio (for a straight duct). It seems reasonable to attribute the latter fact mainly to internal diffusion.

Data by Kruger

The ducted propeller of Kruger shown in Figure 7b was also tested in axial flow, and the blade pitch setting was varied independently over the range $15^{\circ} < \beta < 55^{\circ}$. The procedure described

above was employed for selecting λ and β for maximum η_p at fixed $C_{T_{P(D)}}$, and the values in Table X were obtained from a data plot similar to Figure 8. (Data from Fig. 21, Ref. 19, were used for this purpose).

It can be seen that at the highest value of $C_{T_{P(D)}}$ the measured value of η_p was not much smaller than the ideal Froude efficiency and the agreement between the measured and predicted value of thrust ratio is fair.

However, comparatively high values of β and λ were used during these tests. From the data (Fig. 21, Ref. 19), it appears that stalling of both the duct and the propeller occurred at low advance ratios, but that neither was stalled at the advance ratios in Table X. Therefore, at the lower values of $C_{T_{P(D)}}$ the poor agreement between the theory and data for η_p and $T_{D(P)}/T_{P(D)}$ is attributed mainly to real slipstream effects. However, a small part of the duct thrust was generated by interference with the comparatively large centerbody. This effect was measured (Fig. 7, Ref. 19) and found to give $T_{D(H)} = 0.063 \, Aq_o$.

To illustrate that the above data reduction procedure gives better overall agreement between theory and experiment, we shall now use the more conventional method where for each pitch setting β, the advance ratio λ which gives maximum propulsive efficiency is chosen. The results are given below:

$\beta°$	$\dfrac{V_o}{\omega R}$	$C_{T_{P(D)}}$ (exp.)	γ/V_o	$\dfrac{T_{D(P)}}{T_{P(D)}}$ (exp.)	$\dfrac{T_{D(P)}}{T_{P(D)}} \simeq \dfrac{0.75}{1+2(V_o/\gamma)}$ (pred.) (Eq. (203))	η_P (exp.)	$\eta_P = \dfrac{2}{\dfrac{V_j}{V_o}+1}$ (pred.) (Eq. (206))
15	0.20	1.12	0.46	1.0	0.14	0.50	0.81
25	.35	.33	.15	0.62	.054	.56	.86
35	.48	.22	.10	.80	.036	.59	.90
40	.55	.16	.08	1.0	.029	.58	.93
45	.60	.17	.08	0.92	.029	.55	.92
55	.65	.24	.11	1.0	.039	.52	.89

Upon comparison with Table X it is evident that the overall agreement for thrust ratio is not as good by this method.

We shall now attempt to account for the real slipstream effects in these data by using the procedure described in Section 4.2.2. With this method, we choose λ and β for highest η_p for each fixed value of $C_{T_{P(D)}}$ as was done for Table X. However, we shall use Equations (192) and (193) to estimate γ/V_o with propeller swirl present in the slipstream, rather than using Equation (170) which is valid only for an ideal slipstream with no swirl. Using this method, we find the values given below for two values of $C_{T_{P(D)}}$ which correspond to the first and fourth values in Table X.

β°	$\dfrac{V_o}{\omega R}$	$C_{T_{P(D)}}$	$\dfrac{\gamma}{V_o}$	$\dfrac{T_{D(P)}}{T_{P(D)}}$	$\dfrac{T_{D(P)}}{T_{P(D)}} = \dfrac{0.75}{1 + 2(V_o/\gamma)}$ (pred.) (Eq. (203))
15	0.14	3	2.05	0.3	0.38
25	.32	0.5	0.75	.6	.21

It can be seen from these results that the comparison for thrust ratio is improved by including the effect of propeller swirl in evaluating γ/V_o. The experimental values of η_p, $C_{T_{DP}}$, and λ were used in evaluating γ/V_o from Equations (192) and (193). The relatively poor agreement for the lower value of $C_{T_{P(D)}}$ may be due to frictional head loss which is not included in Equation (192), since we had set $H_\ell = 0$.

Data by Grose

The ducted propeller of Grose shown in Figure 7(c) was also tested in axial flow with independent variation of blade pitch. Using the data reduction method illustrated in Figure 8 (for maximum η_p at fixed $C_{T_{P(D)}}$), we find the values in Table XI by using data from Figures 33 through 37 of Reference 14. It can be seen that relatively high values of η_p were attained in these tests, so that real slipstream effects were probably comparatively small.

Although this duct was apparently unstalled in axial flow (from the discussion in Ref. 14), particularly at the higher advance ratios, agreement between theory and experiment for the

thrust ratio cannot be expected because the duct was too long (c/D = 0.475) for accurate prediction with the present theory. Furthermore, the frictional drag of the duct was relatively large for these tests as compared with the duct thrust. In fact, it was found that for each blade pitch setting tested, except $\beta = 17^\circ$, there was a net drag force on the duct at the advance ratio for which η_P was maximum. Using the data at peak efficiency for $\beta = 17^\circ$, we find the following values.

β°	$\dfrac{V_o}{nD}$	$C_{T_{P(D)}}$	γ/V_o	$T_{D(P)}/T_{P(D)}$	$\dfrac{T_{D(P)}}{T_{P(D)}} \approx \dfrac{0.070}{1+2(V_o/\gamma)}$ (pred.)	η_P	$\eta_P = \dfrac{2}{\dfrac{V_j}{V_o}+1}$ (pred.)
17	0.66	0.41	0.19	0.0049	0.061	0.72	0.91

Thus, $T_{D(P)}$ was much smaller than predicted, in fact generally negative, by the data reduction procedure using $\eta_{P_{max}}$ for fixed β.

4.4 Forces and Moments at Angle of Attack

Here we shall compare the present theory with all the available data for the static stability derivatives of ducted propellers having relatively short, straight, thin ducts. There are evidently two sources of such data: Reference 14 for only $\left(C_{N_\alpha}\right)_{D(P)}$ at relatively low angles of attack ($0 < \alpha_o < 6.3^\circ$), and Reference 13 for both $\left(C_{N_\alpha}\right)_{D(P)}$ and $\left(C_{m_\alpha}\right)_{D(P)}$ at relatively large angles of attack ($50^\circ < \alpha_o < 80^\circ$).

The static derivatives of the duct forces and moments as predicted by the present theory will be compared with these two sources of data as selected by the technique used in Section 4.3 above. That is, combinations of advance ratio and blade pitch will be chosen which give highest η_p at fixed values of $C_{T_{P(D)}}$.

Data by Grose

The comparison of the Grose data will be made for the " high speed" duct (shown in Fig.7(c)) at the highest angle of attack tested, namely 6.3°. The data are from Figures 69 through 80 of Reference 14.

The predicted value of the duct lift force, for $\alpha_o \ll 1$, can be expressed as

$$L_{D(P)} = N_{D(P)} + T_{D(P)} \, \alpha_o \tag{207}$$

which gives upon substitution of Equations (9) and (11) with c/D = 0.475

$$C_{L_\alpha \, D(P)} \equiv \frac{L_{D(P)_\alpha}}{q_o A \alpha_o} = 3.42 + 1.47 \, \frac{\gamma}{V_o} + 0.009 \, \frac{\gamma^2}{V_o^2} \tag{208}$$

The value of γ/V_o will be obtained from Equation (170) using the measured value of $C_{T_{P(D)}}$. Choosing values of β and λ for maximum η_p at fixed $C_{T_{P(D)}}$ from a data plot similar to Figure 8 gives the values in Table XII.

The duct was apparently unstalled during the test conditions used above. All of the data used here were with a free-stream Mach number of 0.2, the lowest value which was tested. The

agreement between theory and experiment for the duct lift curve slope is excellent, despite the rather large value of c/D.

Data by Gill

The three ducts of Gill shown in Figure 7(a) were tested at large angles of attack. However, only the data for the shortest duct $(D_4 P_3 S)$ will be compared with theory for nonaxial flow. All of the ducts were probably stalled at the large angles of attack tested.

The predicted coefficients of this duct (from Eqs. (9), (11), and (13), with c = 0.15D) are

$$\left(C_N\right)_{D(P)} = \sin \alpha_o \left(1.52 \cos \alpha_o + 0.655 \frac{\gamma}{V_o}\right) \tag{209}$$

$$\frac{T_{D(P)}}{T_{P(D)}} = \frac{1}{C_{T_{P(D)}}} \left(0.680 \frac{\gamma^2}{V_o^2} + 1.25 \sin^2 \alpha_o\right) \tag{210}$$

$$\left(C_m\right)_{D(P)} = 1.30 \frac{\gamma}{V_o} \sin \alpha_o \tag{211}$$

and from Equations (169) and (170), we have

$$\frac{V_j}{V_o} = \frac{\gamma}{V_o} + \cos \alpha_o = \sqrt{C_{T_{P(D)}} + 1} \tag{212}$$

Using the data reduction method of Section 4.2.2 and the measured data from Figures 58, 60, 61, 196, 198, and 199 of Reference 13, we obtain the values in Table XIII for two angles of attack, $\alpha_o = 50°$ and $\alpha_o = 80°$.

It can be seen that the measured values of thrust ratio and duct pitching moment are much smaller than predicted. This is attributed to flow separation at the duct leading edge, since both $T_{D(P)}$ and $M_{D(P)}$ depend primarily on leading-edge suction (see Eq. (13)). The agreement is considerably better for $\left(C_N\right)_{D(P)}$ because it is less sensitive to leading-edge separation than is duct thrust. The experimental coefficients $\left(C_N\right)_{D(P)}$ are from 53 to 86 percent of the predicted values.

4.5 Summary and Conclusions for Comparison of Data and Theory

For hovering flight, the predicted values of the duct-to-propeller thrust ratio are, in general, about twice the measured values. This is probably due mainly to flow separated from the duct leading edges. However, in the case of the duct tested by Platt (Ref. 20), which was comparatively long, the measured values of thrust ratio were much <u>higher</u> than predicted either by the present theory (for small c/D) or by simple momentum theory (for large c/D). Additional uncertainty is introduced into the results by real slipstream effects as described in Section 4.2.2.

For axial flight, the data of Gill (Ref. 13) and Grose (Ref. 14) are probably most comparable with the present theory, even through flow separation probably occurred for the duct used by Gill; and the duct used by Grose was actually too long for accurate comparison with the present theory. The measured thrust ratios for these ducts are about half the predicted values.

The data reduction procedure described in Section 4.2.2 to account for real slipstream effects was compared with the usual procedure, and it was shown that the comparison of theory and the data by Kruger (Ref. 17) was considerably improved when the real effects were included in the theory.

Excellent agreement is obtained between measured and predicted values of duct lift force at small angles of attack ($\alpha_o < 6^o$) using the data by Grose (Ref. 14), despite the large chord/diameter ratio ($c/D = 0.475$). Only large angles of attack were tested for the duct used by Gill (Ref. 13), and this duct was probably stalled. Hence, the duct thrust and pitching moment were much smaller than the calculated values. Nevertheless, the normal force was more than half the computed value.

The following conclusions are drawn from the comparison of data with the present theory:

(1) For the only source of data for $\left(C_{N_\alpha}\right)_{D(P)}$ at small angles of attack with a thin duct to which the flow was attached (Ref. 14), this derivative was in excellent agreement with the present theory. Hence, the dominant contribution of the ducted propeller to the dynamic stability of a torpedo-like configuration is well predicted by the present theory (see Section 3.5).

(2) At high angles of attack with flow separation from the duct (Ref. 13), experimental duct coefficients $\left(C_N\right)_{D(P)}$ were from 53 to 86 percent of the predicted values. The measured values of

duct thrust and pitching moment were much smaller than predicted.
This is due in part to real slipstream effects but probably more
to effects of flow separation upon duct leading-edge suction.

(3) There is an urgent need for experimental data on ducted
propellers which do not exhibit leading-edge separation.

5. OUTLINE OF TEST PROGRAM

It is evident from the previous comparison of ducted propeller data with the present theory that additional data are needed for all flight conditions with short ducts and without flow separation from the duct leading edge. There are no data whatever for the dynamic stability derivatives of isolated ducted propellers. Furthermore, there is an apparent need for parametric experimental studies of such design variables as propeller position in the duct, duct chord-to-diameter ratio, duct camber, etc. Basic flow studies should be directed toward prevention of flow separation from the duct leading edge and direct measurement of real slipstream effects.

The following experimental program is specifically designed to provide ducted propeller stability derivatives for comparison with the present theory. A model configuration is suggested, specific tests are outlined for each flight condition, and the stability derivatives are predicted for the suggested configuration.

5.1 Model Design

The ducted propeller shown in Figure 9 is suggested for obtaining data comparable with the present theory. The inner diameter is constant so that tip clearance does not change with propeller location. The radius of the inlet lip is relatively large and is provided with boundary-layer control to prevent leading-edge flow separation. Boundary-layer control is considered essential to prevent flow separation from the duct for all the test conditions. Suction through either a slotted or porous tube

seems suitable for boundary-layer control, and the precise shape of the leading edge may have to be investigated. Counter-rotating, variable-pitch propellers should probably be used to minimize swirl. The Hiller rig (at DTMB) having three-bladed propellers with a diameter of 24 inches and a spacing of 1.5 inches (Ref. 13) might be used with a modified duct. The propellers should be movable in the duct to at least two well-separated positions (fore and aft).

If the propeller axial location is varied in the duct, the inflow velocity distribution to the propeller disk will vary with axial position of the propeller. The present analysis assumes a uniform disk loading, and it may be necessary to vary both blade setting and blade twist to obtain a uniform disk loading experimentally. On the other hand, changes in blade setting alone may give a good enough approximation to uniform loading. In order to investigate this point, we have calculated the radial profile of axial velocity at the entry, exit, and central duct planes for $c = 0.2D$ and $\alpha_o = 0$. The results (Fig. 3(a)) show the axial velocity profiles induced by the bound vorticity on the duct and the trailing vorticity shed from the disk. It can be seen that the profiles are relatively flat, except in the range $0.8 < r/R < 1$. This is particularly true when the axial component of the free stream velocity, $V_o \cos \alpha_o$, is added to these profiles to obtain the total axial velocity profile. Thus, the existing dual propellers used with the Hiller rig seem adequate for the study outlined here. (These propellers were designed to operate in a

uniform flow.) Furthermore, actual duct thickness and boundary-
layer effects tend to decrease the velocity near the duct leading
edge from the computed value, which is singular as shown in Figure
3(a).

In the Hiller rig, duct forces and total configuration forces
were measured (Ref. 13). By subtraction, the forces on the propeller
plus motor housing were obtained. By use of a dummy motor, the
aerodynamic force on the driving motor housing was shown indirectly
to be small. However, it would be desirable to measure this force
directly, particularly at angle of attack, by use of a separate
fairing or wind shield over the motor. In this way, any appreciable
disturbance to the slipstream and/or error in the measured aero-
dynamic reaction on the propeller could be measured directly.

5.2 Hovering Tests

The following specific procedures are suggested for the hover-
ing case: Use only the highest practical propeller speed (and
Reynolds number). Observe flow separation and measure minimum
boundary-layer-control flow required to prevent it. Using this
amount of boundary-layer-control, measure $T_{D(P)_h}$, $T_{P(D)_h}$, P, ω.
Compare thrust ratio with theory by selecting data as described in
Section 4.2. For each value of β, traverse the slipstream and
measure the magnitude and direction of the time average-velocity
vector to determine whether the swirl is actually a minimum when
η_h is maximum. The traverse probably should be about one
diameter downstream of the duct exit plane in order to minimize

both blade interference with the probe and excessive mixing of the slipstream with entrained fluid. Total pressure should also be measured to determine whether it is nearly constant across the wake, as assumed. Use at least two propeller positions in the duct, varying β at each.

5.3   Axial Flow Tests

If, as predicted by theory, there is found to be little effect of propeller axial position on $T_{D(P)_h}/T_{P(D)_h}$ for hovering (measured at optimum η_p for each position), then only one central position might be used in the axial flow tests. However, at least one check case should be made to determine whether propeller position also has little effect in forward flight, as predicted. Repeat the procedure described for a sufficient number of advance ratios to establish the values of $C_{T_{P(D)}}$ (β,λ), η_p (β,λ), and $T_{D(P)}/T_{P(D)}$ at maximum η_p. Compare $T_{D(P)}/T_{P(D)}$ with theory. Use the duct alone to see if $T_D \cong 0$ as predicted for zero duct thickness and to determine whether the use of boundary-layer control actually has little effect upon T_D (aside from preventing flow separation in the presence of the propeller).

5.4   Tests at Angle of Attack

Repeat the procedure in Section 5.3 for a sufficient number of values of α_o in the range $0 < \alpha_o < 90^o$ to determine the effect of α_o on the aerodynamic reactions (including the moment and normal force on the duct and on the propellers). Use the duct alone for comparison with theory (at $C_{T_{P(D)}} = 0$) and also for

comparison with results obtained for the value of λ for which the propeller is free-wheeling. The latter comparison will indicate the effect of propeller losses. Traverse the slipstream to determine swirl, variation in total pressure, and deflection of the slipstream boundary by the free stream (if feasible in the presence of mixing). For each run, use sufficient boundary-layer control to prevent flow separation everywhere on the duct. Compare the static stability derivatives and thrust ratios with the theory for which each of these is given as a function of c/D, $C_{T_{P(D)}}$, and α_o at optimum η_p.

Many of the tests suggested herein are actually being planned at DTMB and should be coordinated with that facility.

5.5 Pitching (q) Tests

In evaluating stability derivatives for pure pitch (as on a rotating arm) use the same blade pitch settings which gave optimum η_p in Section 5.4 for each value of α_o. Determine the boundary-layer control required to prevent flow separation for each run (or determine this in Section 5.4 versus Reynolds number and use the results here). Use maximum arm radius and speed to maximize Reynolds number and minimize boundary-layer control requirement. Use the duct alone to obtain additional information (as in Section 5.4) at angles of attack for which separation can be prevented. Measure the aerodynamic reactions on the duct and propellers, propeller power P and propeller rotational speed ω. Compare with

theory which gives these (as function of c/D, $C_{T_{P(D)}}$, α_o, Dq/V_o at optimum η_p). If a rotating arm of radius R_a is used, then

$$q = \frac{V_o}{R_a} \qquad (213)$$

and the dimensionless pitch parameter is

$$\frac{Dq}{V_o} = \frac{D}{R_a} \qquad (214)$$

Several values of this ratio should be tested in order to determine the maximum value to which each aerodynamic reaction remains proportional to Dq/V_o as predicted by theory.

5.6 Plunging ($\dot{\alpha}$) Tests

Test with pure sinusoidal plunging with boundary-layer control as required to prevent separation. Cover a sufficient range of α_o and λ to establish the functional relationship of each variable. In addition to the complete configuration, test the duct alone as in Section 5.4.

The present theory (for low frequency, small angle of attack, and low amplitude oscillation) predicts that the duct normal force due to $\dot{\alpha}$ is independent of λ, α_o, and frequency; that is,

$$\left(C_{N_{\dot{\alpha}}}\right)_{D(P)} = \pi \frac{c^2}{D^2} \qquad (215)$$

This theory should be compared with data of low frequency, but higher frequencies should also be tested. All the aerodynamic reactions on the duct and propeller should be measured. Both the steady values and the time variations should be measured for comparison with previous tests (Sections 5.3 and 5.4) and with theory.

5.7 Predicted Coefficients and Derivatives

The static thrust coefficients and dynamic stability derivatives for the proposed ducted propeller configuration shown in Figure 9 are given below. They are obtained from Sections 3.1 and 3.4 (with $c = 0.2D$) as functions of the disk loading $C_{T_{P(D)}}$ and the flight conditions $(\alpha_o, q, \dot{\alpha})$. In the equations given below, $\gamma/V_o = \sqrt{C_{T_{P(D)}} + 1} - \cos \alpha_o$, $M_{D(P)}$ is a positive pitching moment about the duct midchord diameter, and $M_{P(D)}$ is about a propeller diameter.

Hovering Flight $(V_o = 0)$

For hovering flight, the predicted thrust ratio is, from Equation (17),

$$\frac{T_{D(P)_h}}{T_{P(D)_h}} = \frac{2}{5\pi} (\ln 80 - 2)^2 = 0.724 \tag{216}$$

Axial Flight $(\alpha_o = 0)$

For axial flight, the predicted thrust ratio is, from Equations (11), (168), and (169),

$$\frac{T_{D(P)}}{T_{P(D)}} = \frac{0.724}{1 + 2(V_o/\gamma)} \tag{217}$$

Steady Flight at Angle of Attack

For this flight condition, the static coefficients of the duct in the presence of an actuator disk are from Equations (9), (11), and (13).

$$\left(c_N\right)_{D(P)} = \sin \alpha_o \left(1.91 \cos \alpha_o + 0.845 \frac{\gamma}{V_o}\right) \tag{218}$$

$$\left(c_T\right)_{D(P)} = 0.724 \frac{\gamma^2}{V_o^2} + 1.46 \sin^2 \alpha_o \tag{219}$$

$$\left(c_m\right)_{D(P)} = 1.45 \frac{\gamma}{V_o} \sin \alpha_o \tag{220}$$

The only static derivative of an isolated dual propeller at small angle of attack, with constant blade pitch and chord, and with $\lambda = V_o/\omega D = 0.1$, and $\sigma = 4Bb/3\pi D = 0.1$ is from Section 3.2.1, a normal force derivative given by

$$\left(c_{N_\alpha}\right)_P = 0.05, \ 0.10, \ 0.16 \quad \text{for} \quad \beta = 10, \ 20, \ 30°, \text{respectively,} \tag{221}$$

since

$$\left(c_{n_\alpha}^*\right)_P = 0 \tag{222}$$

For the Hiller propellers, we have $\sigma \simeq 0.126$ (from Reference 13).

Due to duct interference there is a pitching moment on the propeller which is estimated (from Eq. (65)) to be given by

$$- \frac{\left(C_{m_\alpha}\right)_{(D \to P)}}{\left(C_{m_\alpha}\right)_{D(P)}} = \infty, \ 0.451, \ 0.015 \tag{223}$$

with the propeller located at the entry, central, and exit planes of the duct, respectively.

Pitching Flight

For small rates of pitch, the duct q derivatives in the presence of an actuator disk, are from Equations (18), (20), and (22),

$$\left(C_{N_q}\right)_{D(P)} = 0.675 \frac{\gamma}{V_o} + 0.126 \cos \alpha_o \tag{224}$$

$$\left(C_{T_q}\right)_{D(P)} = -0.0460 \sin \alpha_o \tag{225}$$

$$\left(C_{m_q}\right)_{D(P)} = 0.0376 \frac{\gamma}{V_o} \tag{226}$$

The q derivatives for an isolated propeller at $\alpha_o = 0$ are, for the previously assumed propeller parameters: a side force derivative given by

$$- \left(C_{Y_q}\right)_P = 0 \tag{227}$$

and for a single propeller a pitching moment derivative given, respectively, by

$$- \left(C_{m_q}\right)_P = 0.17, \ 0.17, \ 0.18 \quad \text{for} \quad \beta = 10^\circ, \ 20^\circ, \ 30^\circ \tag{228}$$

Note that $\left(C_{m_q}\right)_P$ for a dual propeller is not given in Reference 5 nor is it calculated herein.

Due to q interference from the duct, there is a pitching moment on the propeller which is estimated (from Eq. 71) to be given by

$$\frac{\left(C_{m_q}\right)_{(D \rightarrow P)}}{\left(C_{m_q}\right)_{D(P)}} = + \infty, \ -12.0, \ -10.2 \qquad (229)$$

with the propeller located at the entry, central, and exit planes of the duct respectively.

Plunging Flight

For small angles of attack, the estimated normal force derivative of the duct due to plunging (Eq. (30)) is

$$\left(C_{N_{\dot{\alpha}}}\right)_{D(P)} \simeq 0.126 \qquad (230)$$

There is no thrust force or moment due to $\dot{\alpha}$; i.e., $\left(C_{T_{\dot{\alpha}}}\right)_{D(P)} = \left(C_{m_{\dot{\alpha}}}\right)_{D(P)} = 0$

The estimated reaction on the propeller due to plunging, for constant blade pitch and chord and $\alpha_o \ll 1$, is only a normal force with (see Eq. 41)

$$\left(C_{N_{\dot{\alpha}}}\right)_{P(D)} = \pi B \left(\frac{b}{D} \sin \beta\right)^2 \qquad (231)$$

6. CONCLUSIONS

A theoretical analysis has been presented for predicting the forces, moments, and stability derivatives of an isolated ducted propeller. The analysis is an extension of the steady-flow analysis of Reference 1 in which the duct is represented as a straight, short, thin ring surrounding a uniformly loaded actuator disk which produces a slipstream velocity much greater than the lateral component of the flight velocity $(V_j \gg V_o \sin \alpha_o)$. This representation, of course, requires that the minimum disk loading (for which the theory is valid) increase with angle of attack. In the present work, the approximations of Reference 1 have been investigated in detail and the effect of moving the propeller in the duct has also been taken into account. In addition, the interference effect of the duct on a real propeller with finite blades has been incorporated, and the cases of pitching and plunging motions have been treated. An experimental program specifically designed to check the theory has been outlined.

6.1 Theoretical Results for Isolated Ducted Propeller

The results quoted here are applicable to all angles of attack to the extent that the propeller can be represented by an actuator disk. Any results pertaining to the forces on a propeller with finite number of blades, however, are restricted to small angles of attack. With this restriction, the following conclusions can be drawn from the theoretical analysis of an isolated, moderately loaded, ducted propeller of solidity 0.1:

(1)   Except for thrust force and pitching moment due to pitch (about the duct center), the forces and moments on the duct are considerably larger than those on the propeller.

(2)   When it is located within the duct the propeller produces a positive damping $(-C_{m_q})$ which is greater than the negative damping due to the duct. This fact is significant for STOL airplanes with ducted propellers mounted on a lateral axis through the center of gravity.

(3)   The forces and moments acting on the duct are unaffected by the location of the propeller inside the duct.

(4)   The duct interference on the propeller produces a large positive damping, unless the propeller is placed near the duct leading edge where it produces large negative damping.

(5)   The normal force, provided by a ducted propeller, is from 20 to 60 percent greater than for a flat plate of the same projected area, even for zero disk loading.

(6)   All of the static and pitching derivatives for the duct in the presence of the propeller are found to increase with propeller disk loading. Some derivatives increase nearly proportionately to disk loading, and others are nearly independent of it.

6.2   Theoretical Results for Torpedo-Like Configurations

From the analysis of a torpedo-like configuration (in axial flow) consisting of a body of revolution with rear-mounted ducted propeller, the following conclusions are drawn:

(1)   The dominant contribution of the ducted propeller to the damping is produced by the normal force on the duct due to its induced angle of attack arising from the q motion. This damping is increased at higher disk loadings.

(2) Both C_{m_q} and $C_{m_{\dot{\alpha}}}$ due to the hull are large and are associated with the hull boundary layer, which has been assumed to oscillate as a solid body with the hull. Therefore, a more refined analysis seems warranted, even though C_{m_q} and $C_{m_{\dot{\alpha}}}$ due to the hull tend to cancel one another.

(3) The thrust interference between the ducted propeller and the hull appears to be large, depending upon the geometry and the propeller disk loading. Therefore, a more refined analysis of this effect appears to be warranted.

(4) Because of the radial inflow produced at the base of a symmetrical hull with attached flow, such a hull is expected to affect the stability derivatives of a rear-mounted ducted propeller in the same direction as would an increase in propeller disk loading.

6.3 Comparisons with Experiment

The comparisons attempted herein between the present theory and available experimental data have indicated the following conclusions:

(1) Only one reference (Ref. 14) provided data free of flow separation for a check on any of the calculated stability derivatives. This check showed that, for small angles of attack, the present theory gave excellent predictions of the static stability derivative C_{N_α}. The dominant factor in the dynamic stability of the torpedo-like configuration at zero angle of attack was found to be the lift curve slope of the isolated ducted propeller.

(2) Only one reference (Ref. 21) provided data for a short duct free of flow separation as a check on the thrust ratio in axial flow. For this case, the theory over-predicted $T_{D(P)}/T_{P(D)}$ by about 20 percent at the lowest advance ratio. The error was larger at higher advance ratios because of duct drag not included in the theory.

(3) In one case of a rather long unseparated duct in hovering flight (Ref. 20), the measured ratio $T_{D(P)}/T_{P(D)}$ was far above that predicted by either the present (small c/D) theory or the asymptotic simple momentum theory for infinitely long ducts. There thus appears to be a real need for a theory valid for ducted propellers of intermediate chord/diameter ratios.

(4) There appear to be no experimental data for pitching moments on unseparated ducts during steady flow at angle of attack or for either normal force or pitching moments on unseparated ducts at high angles of attack. However, the static stability derivative C_{N_α} predicted by the present theory at angles of attack of 50° and 80° agreed within about 15 to 45 percent with the data of Reference 13 for which the flow was probably separated at the duct leading edge.

(5) There are at present no experimental data for the dynamic stability derivatives of isolated ducted propellers.

(6) The data reduction technique presented herein succeeded in bringing theory and experiment into closer agreement than would be indicated by comparisons made at the same advance ratio and/or blade setting.

7. RECOMMENDATIONS FOR FUTURE WORK

On the basis of the foregoing conclusions and the investigations undertaken in the present report, the following recommendations are made regarding future theoretical and experimental work on ducted propellers:

(1) There is an urgent need for systematic experimental data on ducted propellers having relatively straight, thin ducts of small chord/diameter ratio <u>without leading-edge separation</u> at all flight conditions to check the theory. A program designed for this purpose has been suggested herein.

(2) A theory should be developed for treating ducted propellers of larger chord/ diameter ratios than are treated in the present theory. In addition, the effects of duct camber and thickness should be investigated.

(3) The present theory should be extended to cover nonuniform disk loadings and wake swirl.

(4) The effects of interference between a ducted propeller and a wing, ground plane, or adjacent ducted propellers should be studied theoretically, especially for VTOL configurations.

(5) The theory should be extended to study the speed derivatives $(\dot{V})$ of a ducted propeller at angle of attack, which may be significant in the transitional flight regime for a VTOL aircraft.

(6) A more refined analysis should be carried out to study the mutual interference between the hull and rear-mounted ducted propeller for a specific modern torpedo and for a high-speed submarine.

This analysis should include a further investigation of the averaging process used herein because of its possible significant effect on the duct derivative C_{N_α} which evidently dominates the damping in pitch of the configuration.

(7) Engineering calculations should be made to investigate the relative importance of the ducted propeller stability derivatives on the overall stability of vehicles in the following categories:

(a) VTOL aircraft employing tilting ducts.

(b) Vehicles employing multiple ducted propellers in which mutual interference may be important but ground effect is not.

(c) Ground-effect machines.

REFERENCES

1. Aerophysics Development Corp., Aerial Jeep Phase I Final Report, Appendix D, vol. II of II. U. S. Army Contract No. DA-44-177-TC-397, ADC Rept. No. 520-3/R24/46, Dec. 1957.

2. Sacks, A. H., Burnell, J. A.: A Critical Review of the State of the Art. Progress in Aeronautical Sciences, edited by Ferri, A., Küchemann,D., and Sterne, L. H. G., Pergamon Press, New York, 1962, pp. 85-135.

3. Ritter,A., and Ordway, D. E.: Ducted Propeller and Related Airscrew Studies at TAR. TAR-TR614, Therm. Advanced Research Division of Therm., Ithica, New York, Aug. 1961.

4. Morgan, W. B., A Theory of the Ducted Propeller with a Finite Number of Blades, Univ. of Calif., Institute of Engr. Research, Berkeley, Calif., Series No. 82, Contract No. N-onr-222(30), May 1961.

5. Ribner, H. S.: Propellers in Yaw. NACA Rept. 820.

6. Küchemann, D., and Weber, J.: Aerodynamics of Propulsion. McGraw-Hill Book Co., Inc., New York, 1953.

7. Ribner, H. S.: The Ring Airfoil in Nonaxial Flow. Jour. Aero. Sci., vol. 4, no. 9, Sept. 1947, p. 529.

8. Durand, W. F: Aerodynamic Theory, vol. II, Div. E. Calif. Inst. of Tech., 1943.

9. Greenman, R. N. and Gaffney, M. G.: Dynamic Stability Analysis of Ducted Fan Type Flying Platforms. Rept. no. ARD-233, Advanced Research Division of Hiller Aircraft Corp., Contract No. Nonr 1357(00), phase IV, May 1959.

10. Nielsen, Jack N.: Missile Aerodynamics. McGraw-Hill, New York, 1955.

11. Schlichting, H.: Boundary Layer Theory. McGraw-Hill, New York, 1955.

12. Milne-Thomson, L. M.: Theoretical Hydrodynamics, 4th Edition. The Macmillan Co., New York, 1960.

13. Gill, W. J.: Wind Tunnel Tests of Several Ducted Propellers in Non-Axial Flow. Report No. ARD-224, Contract No. Nonr 1357 (00), phase IV, Advanced Research Division of Hiller Aircraft Corp., April 20, 1959.

14. Grose, R. M.: Wind Tunnel Tests of Shrouded Propellers at Mach Numbers from 0 to 0.60. Contract No. AF(616)-5363, WADC TR 58-604, ASTIA Doc. No. AD-205464, Research Dept. United Aircraft Corp., Dec. 1958.

15. Grunwald, K. J. and Goodson, K. W.: Aerodynamic Loads on an Isolated Shrouded-Propeller Configuration for Angles of Attack from -10° to 110°. NASA TN D-995, Jan. 1962.

16. Suarez, A.: Hydrodynamic Coefficients of a Torpedo-Like Test Vehicle Equipped with a Ducted Propeller System. Parts I through IV, Rept. Nos. 578, 579, 626, 627, Experimental Towing Tank, Stevens Institute of Technology, Hoboken, New Jersey. (Confidential)

17. Horn, Von F.: Jahrbuch 1940 der Schiffbautechnischen Gesellshaft.

18. Moser, H. H. and Livingston, C. L.: Experimental and Analytic Study of the Ducted Fan and Fan-in-Wing in Hovering and Forward Flight. TR 79-1, ASTIA Doc. No. AD 201 398, Aeroelastic and Structures Research Lab., MIT, Jan. 1959.

19. Krüger, W.: On Wind Tunnel Tests and Computations Concerning the Problem of Shrouded Propellers. NACA TM 1202, Feb. 1949.

20. Platt, R. J., Jr.: Static Tests of a Shrouded and an Unshrouded Propeller. NACA RM No. L7H25.

21. Allen, H. J. and Rogallo, F. M.: Ring-Cowled Propellers. Engineer Thesis, ME Dept., Stanford University, June 1935.

22. Bromwich, T. J.: An Introduction to the Theory of Infinite Series. Macmillian and Co., Ltd., London, 1949.

APPENDIX A

DUCT SURFACE VELOCITY DISTRIBUTION W FOR
PURE-PITCH FLIGHT CONDITION

As explained in Section 2, the complete velocity distribution
W for pure pitch is composed of three parts (see Fig. 2): $w_h + \overline{w}_{h_i}$
due to hovering, $w_\alpha + w_{\alpha_i}$ due to free stream V_o at angle of
attack α_o, and $w_q + \overline{w}_{q_i}$ due to pitching rate q about the
duct midchord diameter. Here we shall determine successively these
three parts of W. The derivation of the first two parts will be
compared with Reference 1, from which it is taken, in order to
point out certain detailed errors. However, the final result of
Appendix B (after integration of W^2 and cancellation of higher
order terms in c/D) gives net duct forces and moments which are
identical with the results given in Reference 1 for both hovering
and steady flight at angle of attack.

A.1 SURFACE VELOCITY DUE TO HOVERING, $w_h + \overline{w}_{h_i}$

For no motion of the duct (hovering flight), the duct surface
velocity distribution w_h is induced by the vorticity shed by
the actuator disk (γ in Fig. 2) and by the bound vorticity γ_h
which is generated on the duct to satisfy the boundary and Kutta
conditions (considering γ_h to lie in a flat surface). Finally,
as described in Section 2, $\overline{w}_{h_i}$ is self-induced by γ_h due to
the fact that this vorticity actually lies on a ring rather than
on a flat surface.

The complete surface velocity distribution on the duct for
hovering flight, $w_h + \overline{w}_{h_i}$, can be obtained from the results of
this section by adding Equations (A.15) and (A.47) for w_h and
Equation (A.53) for $\overline{w}_{h_i}$. This gives

$$w_h + \bar{w}_{h_i} = u_{\gamma_s} + w_{F_s} + \bar{w}_{h_i} = \frac{\gamma}{2\pi} \left\{ \frac{3\pi}{2} - \theta + \left(\ln \frac{16D}{c} - 2 \right) \tan \frac{\theta}{2} \right.$$

$$- \frac{c}{2D} \left[\ln \frac{8D}{c} - \ln(1 - \cos \theta) \right] (1 - \cos \theta)$$

$$\left. + \frac{c}{2D} \left(\ln \frac{16D}{c} - 1 \right) \left(\ln \frac{4D}{c} + \frac{1}{2} \right) \right\} \tag{A.1}$$

On the inside and outside of the duct trailing edge, w_h/γ is 3/4 and $-(1/4)$, respectively. For $\bar{w}_{h_i}/\gamma$, we obtain the following values

c/D	$\bar{w}_{h_i}/\gamma$
0	0
0.1	0.136
.2	.189
.4	.240

Thus $\bar{w}_{h_i}$ is somewhat smaller than w_h at the trailing edge.

It is assumed that the disk loading $C_{T_{P(D)}}$ or pressure rise across the disk Δp, is constant over the disk, which is located at the exit plane of a thin duct of constant diameter D. The flow field generated by the actuator disk is induced by the shed vorticity γ which surrounds its slipstream. The γ vorticity distribution is approximated by a sheath of vorticity uniformly distributed over a semi-infinite cylinder as shown in Figure 2 and Sketch A.1.
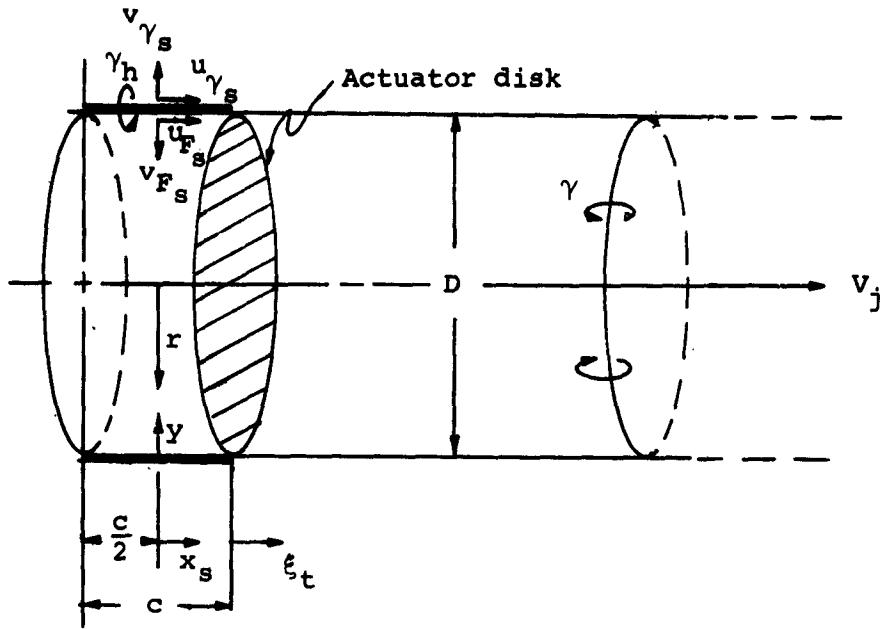
Sketch A.1.- Ducted actuator-disk nomenclature.

A.1.1 Velocity Induced by γ Shed From Actuator Disk

The velocity components induced directly by γ at the duct surface, are (p. 319, Ref. 6):

$$u_{\gamma_s} = \frac{\gamma}{2\pi} \left[\frac{\pi}{2} + \sqrt{1 - k^2} \; K(k) \right] \tag{A.2}$$

$$v_{\gamma_s} = \frac{\gamma}{2\pi} \left[\left(k - \frac{2}{k} \right) K(k) + \frac{2}{k} \, E(k) \right] \tag{A.3}$$

where $K(k)$ and $E(k)$ are the complete elliptic integrals of first and second kind, respectively, as defined in the List of Symbols. The series expansions of these functions are (p. 307, Ref. 6):

$$K(k) = \ln \frac{4}{\sqrt{1 - k^2}} + \frac{1}{4} \ln \left(\frac{4}{\sqrt{1 - k^2}} - 1 \right) (1 - k^2)$$

$$+ \frac{9}{64} \left(\ln \frac{4}{\sqrt{1 - k^2}} - \frac{7}{6} \right) \left(1 - k^2 \right)^2 + \ldots \tag{A.4}$$

$$E(k) = 1 + \frac{1}{2} \left(\ln \frac{4}{\sqrt{1 - k^2}} - \frac{1}{2} \right) (1 - k^2)$$

$$+ \frac{3}{16} \left(\ln \frac{4}{\sqrt{1 - k^2}} - \frac{13}{12} \right) (1 - k^2)^2 + \ldots \quad (A.5)$$

where

$$k^2 = \frac{1}{1 + \frac{\xi^2}{D^2}} \quad (A.6)$$

$$1 - k^2 = \frac{\xi^2 / D^2}{1 + \frac{\xi^2}{D^2}} \quad (A.7)$$

and for Equations (A.2) and (A.3) we have $\xi = \xi_t$ as shown in Sketch A.1. Now, if $\left| \xi \right| \ll \left| D \right|$, then $k^2 \approx 1$, and the leading terms in the series expansion of E and K are simply

$$K(k) \approx \ln \left| \frac{4D}{\xi} \right| \quad (A.8)$$

$$E(k) \approx 1 \quad (A.9)$$

The duct lies on the surface $r = D/2$, $-c < \xi_t < 0$. Since we shall assume here that $c \ll D$, the velocity components induced by the actuator disk on the duct surface are given approximately by the leading terms in the series expansion of Equations (A.2) and (A.3) which are (for $\xi = \xi_t$)

$$u_{\gamma_s} \approx \frac{\gamma}{2\pi} \left[\frac{\pi}{2} + \frac{\xi_t}{D} \left(\ln 8 - \ln \left| \frac{2\xi_t}{D} \right| \right) \right] \quad (A.10)$$

$$v_{\gamma_s} \simeq \frac{\gamma}{2\pi} \left[(2 - \ln 8) + \ln \left| \frac{2\xi_t}{D} \right| \right] \qquad (A.11)$$

These equations agree with Equations (A.2) and (A.3) within 1 percent and 10 percent, respectively, when

$$\left| \xi_t \right| \leq \frac{D}{4} \qquad (A.12)$$

A.1.2 Complex Potential F Required for Boundary Condition

In order to make the duct a streamline, a distribution of vorticity must be added along the duct chord which induces a radially <u>inward</u> velocity component v_{F_s} equal to the radial component v_{γ_s} (Sketch A.1). To do this, we shall find a complex potential function $F(z)$ which gives $v_{F_s} = v_{\gamma_s}$ by treating a chordwise strip of the duct as a two-dimensional airfoil.[1] It is convenient for this purpose to introduce the Joukowski transformation (p. 159, Ref. 12,)thus

$$z = \frac{c}{4} \left(\zeta + \frac{1}{\zeta} \right) = x_s + iy \qquad (A.13)$$

and with the actuator disk at the trailing edge of the duct, we have from Sketch A.1

$$x_s = \xi_t + \frac{c}{2} \qquad (A.14)$$

The chordwise strip $(- c/2 < x_s < + c/2)$ maps on to the unit circle $\zeta_s = e^{i\theta}$ such that on the duct surface $z = x_s = c/2 \cos \theta$. Thus, we can write Equations (A.10) and (A.11) in terms of θ as follows:

---

[1]This approach is justified with the restriction that $c \ll D$.

$$u_{\gamma_s} = \frac{\gamma}{2\pi} \left\{ \frac{\pi}{2} - \frac{c}{2D} (1 - \cos\,\theta) \left[\ln\,\frac{8D}{c} - \ln(1 - \cos\,\theta) \right] \right\} \quad (A.15)$$

$$v_{\gamma_s} = \frac{\gamma}{2\pi} \left[2 - \ln\,\frac{8D}{c} + \ln(1 - \cos\,\theta) \right] \quad (A.16)$$

Let the required complex potential function in the ζ plane

$$F' = \Phi' + i\psi' = \frac{i\Gamma_h}{2\pi} \ln\,\zeta + \sum_{n=0}^{\infty} \frac{ia_n}{\zeta^n} \quad (A.17)$$

Then the complex velocity in the ζ plane is given by (p. 150, Ref. 12)

$$u_F' - iv_F' = + \frac{dF'}{d\zeta}$$

$$= \frac{i\Gamma_h}{2\pi\zeta} + \sum_{n=0}^{\infty} - \frac{ia_n n}{\zeta^{(n+1)}} \quad (A.18)$$

On the circle $(\zeta_s = e^{i\theta})$, we have

$$u_{F_s}' - iv_{F_s}' = \frac{i\Gamma_h}{2\pi} e^{-i\theta} - \sum_{n=0}^{\infty} ia_n n e^{-(n+1)i\theta} \quad (A.19)$$

The complex velocity at a corresponding point in the physical plane is

$$u_F - iv_F = \frac{dF'}{d\zeta}\,\frac{d\zeta}{dz} = (u_F' - iv_F')\,\frac{4\zeta}{c\left(\zeta - \frac{1}{\zeta}\right)} \quad (A.20)$$

so that on the flat plate $(\zeta_s = e^{i\theta})$ we have, in terms of θ,

$$u_{F_s} - iv_{F_s} = \left(u_{F_s}' - iv_{F_s}' \right)\,\frac{2e^{i\theta}}{ci\,\sin\,\theta} \quad (A.21)$$

Substituting Equation (A.19) into (A.21) gives

$$u_{F_s} - iv_{F_s} = \frac{\Gamma_h}{\pi c \sin \theta} - \sum_{n=0}^{\infty} \frac{2a_n n}{c \sin \theta} e^{-in\theta} \qquad (A.22)$$

Therefore, v_{F_s} is finally found to be

$$+v_{F_s} \sin \theta = \text{Im} \sum_{n=0}^{\infty} \frac{2a_n n}{c} (\cos n\theta - i \sin n\theta) \qquad (A.23)$$

Now let us express v_{γ_s} in the same form as v_{F_s}. The following identity can be found on page 202 of Reference 22)

$$\ln(1 - \cos \theta) = - \ln 2 - 2 \sum_{n=1}^{\infty} \frac{1}{n} \cos n\theta \qquad (A.24)$$

By use of this and the identity

$$2 \sin \theta \cos n\theta \equiv \sin(1 + n)\theta + \sin(1 - n)\theta \qquad (A.25)$$

Equation (A.16) can be written in the form

$$v_{\gamma_s} \sin \theta = \frac{\gamma}{2\pi} \left\{ \left(2 - \ln \frac{16D}{c} \right) \sin \theta \right.$$

$$\left. - \sum_{n=1}^{\infty} \frac{1}{n} \left[\sin(n + 1)\theta - \sin(n - 1)\theta \right] \right\} \qquad (A.26)$$

Now, setting v_{γ_s} (Eq. (A.26)) equal to v_{F_s} (Eq. (A.23)) in order to satisfy the boundary condition of zero normal velocity through the duct surface, we find that (a_n) is real, so that Equation (A.23) can be written as

$$v_{F_s} \sin \theta = \sum_{n=0}^{\infty} - \frac{2a_n n}{c} \sin n\theta \qquad (A.27)$$

Substitution of v_{γ_s} for v_{F_s} (Eq. (A.26) into Eq. (A.27)) then gives

$$\left(2 - \ln \frac{16D}{c}\right)\sin \theta + \sum_{n=0}^{\infty} \frac{4\pi n a_n}{\gamma c} \sin n\theta$$

$$+ \sum_{n=1}^{\infty} - \frac{\sin(n+1)\theta}{n} + \frac{\sin(n-1)\theta}{n} = 0$$

(A.28)

By reindexing, this equation can be written in the following form:

$$\left(2 - \ln \frac{16D}{c}\right)\sin \theta + \frac{4\pi n a_0}{\gamma c} + \sum_{n=1}^{\infty} \left(\frac{4\pi n a_n}{\gamma c} + \frac{1}{n+1}\right) \sin n\theta$$

$$- \sum_{n=2}^{\infty} \frac{\sin n\theta}{n-1} = 0$$

(A.29)

Consequently, the coefficients a_n are found to be

$$\left.\begin{array}{l} a_0 = 0 \\[2mm] a_1 = - \frac{\gamma c}{4\pi}\left(\frac{5}{2} - \ln \frac{16D}{c}\right) \\[2mm] a_n = \frac{\gamma c}{2\pi n(n^2 - 1)} \quad \text{for} \quad n > 1 \end{array}\right\}$$

(A.30)

Thus, Equation (A.17) for the complex potential can be written as

$$F' = \Phi' + i\psi' = \frac{i\Gamma_h}{2\pi} \ln \zeta + i \frac{\gamma c}{2\pi} \sum_{n=2}^{\infty} \frac{\zeta^{-n}}{n(n^2 - 1)} + \frac{ia_1}{\zeta}$$

(A.31)

Now, on the circle $(\zeta_s = e^{i\theta})$, we have

$$F_s{}' = \Phi_s{}' + i\psi_s{}' = -\frac{\Gamma_h \theta}{2\pi} + \sum_{n=0}^{\infty} ia_n(\cos n\theta - i \sin n\theta) \quad \text{(A.32)}$$

Thus, substitution of Equation (A.30) gives

$$\Phi_s{}' = -\frac{\Gamma_h \theta}{2\pi} + \frac{\gamma_c}{2\pi} \sum_{n=2}^{\infty} \frac{\sin n\theta}{n(n^2 - 1)} + a_1 \sin \theta \quad \text{(A.33)}$$

In order to evaluate the series the following technique is used (from Ref. 1): We use the identity from Reference 22, page 188

$$\sum_{n=1}^{\infty} \frac{\sin n\theta}{n} = \frac{\pi - \theta}{2} \quad 0 < \theta < 2\pi \quad \text{(A.34)}$$

We then form the product

$$(\cos \theta - 1) \sum_{n=1}^{\infty} \frac{\sin n\theta}{n} = \frac{1}{2} \sum_{n=1}^{\infty} \frac{\sin(n+1)\theta + \sin(n-1)\theta - 2 \sin n\theta}{n}$$

$$\text{(A.35)}$$

Now, by reindexing, we can write Equation (A.35) as

$$\sum_{n=2}^{\infty} \frac{\sin n\theta}{n(n^2 - 1)} = \frac{\pi - \theta}{2} (\cos \theta - 1) + \frac{3}{4} \sin \theta \, , \quad 0 \le \theta \le 2\pi$$

$$\text{(A.36)}$$

Thus, substitution into Equation (A.33) yields

$$\Phi_s{}' = -\frac{\Gamma_h \theta}{2\pi} + \frac{\gamma_c}{2\pi} \left[\frac{\pi - \theta}{2} (\cos \theta - 1) + \frac{3}{4} \sin \theta \right] + a_1 \sin \theta$$

$$\text{(A.37)}$$

Finally, substitution of Equation (A.30) and differentiation with respect to θ gives the surface velocity distribution on the unit circle due to F. That is,

$$w_{F_s}' = \frac{\partial \Phi_s'}{\partial \theta} = -\frac{\Gamma_h}{2\pi} + \frac{\gamma c}{2\pi} \left[\frac{1 - \cos\theta}{2} + \frac{\theta - \pi}{2} \sin\theta + \frac{3}{4}\cos\theta \right.$$

$$\left. + \left(\frac{1}{2} \ln \frac{16D}{c} - \frac{5}{4} \right) \cos\theta \right] \tag{A.38}$$

A.1.3 Fulfillment of the Kutta Condition

The value of the total circulation around the duct in hovering Γ_h will now be determined such that the Kutta condition of finite velocity is satisfied at the trailing edge of the duct. Mathematically, this requires that the trailing edge be a stagnation point in the transformed plane. That is, $w_s' = 0$ at $\theta = 0$. From Equation (A.38), with $\theta = 0$, we have at the duct trailing edge

$$\left(w_{F_s}' \right)_{\left(x_s = \frac{c}{2} \right)} \equiv w_{F_t}' = -\frac{\Gamma_h}{2\pi} - \frac{\gamma c}{2\pi} \left(1 - \ln \frac{16D}{c} \right) \tag{A.39}$$

This is only the part of w_t' which is due to the potential function F. However, w_{γ_t}', the part due to γ is zero, as shown below. From Equations (A.15) and (A.16) with $\theta = 0$, we find that the velocity components induced by γ at the trailing edge of the plate are

$$\left. \begin{aligned} u_{\gamma_t} &= \frac{\gamma}{4} \\[2ex] v_{\gamma_t} &= \frac{\gamma}{2\pi} \left[2 - \ln \frac{8D}{c} + \ln(1 - \cos\theta) \right] \end{aligned} \right\} \tag{A.40}$$

The complex velocity in the circle (ζ) plane is related to that in the physical plane by

$$u_\gamma{}' - iv_\gamma{}' = \left(u_\gamma - iv_\gamma\right)\frac{dz}{d\zeta} \tag{A.41}$$

Evaluation at $\theta = 0$ gives

$$u_{\gamma_t}{}' - iv_{\gamma_t}{}' = \left(u_{\gamma_t} - iv_{\gamma_t}\right)\frac{c}{2}\left(\sin^2\theta + i\sin\theta\cos\theta\right)\Big|_{\theta=0} \tag{A.42}$$

Hence, substitution into Equations (A.40) gives

$$u_{\gamma_t}{}' = \frac{c\gamma}{8}\sin\theta\cos\theta\,\ln(1-\cos\theta)\Big|_{\theta=0} \tag{A.43}$$

$$v_{\gamma_t}{}' = \frac{c\gamma}{4\pi}\sin^2\theta\,\ln(1-\cos\theta)\Big|_{\theta=0} \tag{A.44}$$

Evaluation of Equations (A.43) and (A.44) shows that they are each equal to zero; therefore, $w_{\gamma_t}{}'$ is zero.

Thus, if we set $w_{F_t}{}'$ equal to zero in Equations (A.39) to satisfy the Kutta condition, we find that

$$\frac{\Gamma_h}{2\pi} = \frac{\gamma c}{4\pi}\left(\ln\frac{16D}{c} - 1\right) \tag{A.45}$$

Finally, substitution of Equation (A.45) into Equation (A.38) gives the surface velocity on the circle

$$w_{F_s}{}' = \frac{\gamma c}{4\pi}\left[\left(2 - \ln\frac{16D}{c}\right)(1-\cos\theta) + (\theta-\pi)\sin\theta\right] \tag{A.46}$$

Hence, we find from Equation (A.41) that the surface velocity distribution on the plate due to γ is

$$w_{F_s} = w_{F_s}' \frac{d\theta}{dx_s} = -\frac{2w_{F_s}'}{c \sin \theta}$$

$$= -\frac{\gamma}{2\pi}\left[\left(2 - \ln \frac{16D}{c}\right)\tan \frac{\theta}{2} + (\theta - \pi)\right] \qquad (A.47)$$

We have now found the hovering velocity distribution $(w_h = u_{\gamma_s} + w_{F_s})$ induced by γ and γ_h. This result (Eq. (A.15) plus (A.47)) is identical with Equation (12) of Reference 1. Now we seek the averaged self-induced component $\overline{w}_{h_i}$, as discussed in Section 2.

A.1.4 Self-Induced Velocity $\overline{w}_{h_i}$

As described in Section 2, there is a surface velocity compo-
nent w_{h_i} which is self-induced by the bound vorticity γ_h due
to the fact that it lies on a ring rather than on a flat surface.
We shall find $\overline{w}_{h_i}$, its average value, by summing the elementary
velocity components induced by the vorticity $(\gamma_h \, d\xi_R)$ on each
elementary ring $d\xi_R$ of the duct (Sketch A.2).
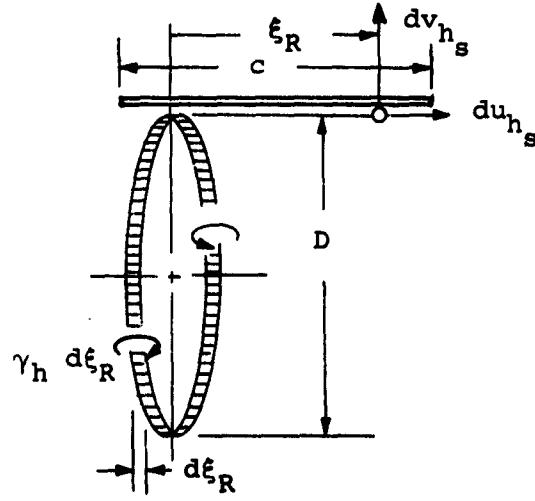
Sketch A.2.- Velocity components induced by a
vortex ring of constant strength.

Each elementary ring consists of a vortex ring of constant strength (with respect to ϕ) equal to $\gamma_h \, d\xi_R$ where ξ_R is the axial distance from the ring to a fixed point on the duct surface. Thus $-c < \xi_R < c$. For $c/D \ll 1$, we can write (see pp. 306 and 307 of Ref. 6)

$$\left.\begin{array}{l} du_{h_s} = \left(\ln\left| \dfrac{4D}{\xi_R} \right| - 1 \right) \dfrac{\gamma_h \, d\xi_R}{2\pi D} \\[3mm] dv_{h_s} = \dfrac{\gamma_h \, d\xi_R}{2\pi \xi_R} \end{array}\right\} \quad \xi_R \ll D \qquad (A.48)$$

Thus, dv_{h_s}, the radial velocity component, is equal to that for a straight line filament of infinite length ($D = \infty$) if $\xi_R \ll D$. Consequently, v_{h_s} and the boundary condition have been accounted for correctly in the foregoing (flat plate) analysis. However, we must account for u_{h_s}, the axial component of velocity which is self-induced by the bound vorticity on the duct, since u_{h_s} is zero for a straight line filament.

Following the method used in Reference 1, both the bound vorticity distribution γ_h and the self-induced velocity w_{h_i} will be averaged over the chord as follows. Corresponding to the surface velocity w_h, we obtain the bound vorticity distribution

$$\gamma_h = w_h(\theta) - w_h(2\pi - \theta) \qquad (A.49)$$

Thus, using Equations (A.15) and (A.47) for w_h, we have

$$\gamma_h = \frac{\gamma}{\pi} \left[\left(\ln \frac{16D}{c} - 2 \right) \tan \frac{\theta}{2} + \pi - \theta \right] \qquad (A.50)$$

The average value of γ_h over the chord is therefore

$$\bar{\gamma}_h = \frac{1}{c} \int_{-\frac{c}{2}}^{+\frac{c}{2}} \gamma_h \, dx_s = \frac{1}{2} \int_0^{\pi} \gamma_h \sin \theta \, d\theta = \frac{\gamma}{2} \left(\ln \frac{16D}{c} - 1 \right) \quad \text{(A.51)}$$

For this constant vorticity, Equation (A.48) gives

$$\bar{u}_{h_s} = \frac{\bar{\gamma}_h}{2\pi D} \int_{-\frac{c}{2}+x_s}^{\frac{c}{2}+x_s} \left(\ln 4D - 1 - \ln |\xi_R| \right) d\xi_R$$

$$= \frac{\bar{\gamma}_h}{2\pi D} \left\{ (\ln 4D - 1)c - \left(\frac{c}{2} - x_s \right) \left[\ln \left(\frac{c}{2} - x_s \right) - 1 \right] \right.$$

$$\left. - \left(\frac{c}{2} + x_s \right) \left[\ln \left(\frac{c}{2} + x_s \right) - 1 \right] \right\} \quad \text{(A.52)}$$

Averaging this expression over the chord gives the averaged self-induced velocity $\bar{w}_{h_i}$ as

$$\bar{w}_{h_i} = \frac{1}{c} \int_{-\frac{c}{2}}^{+\frac{c}{2}} \bar{u}_{h_s} \, dx_s = \frac{\bar{\gamma}_h c}{2\pi D} \left(\ln \frac{4D}{c} + \frac{1}{2} \right)$$

$$= \frac{\gamma c}{4\pi D} \left(\ln \frac{16D}{c} - 1 \right) \left(\ln \frac{4D}{c} + \frac{1}{2} \right) \quad \text{(A.53)}$$

This equation is identical with Equation (13) of Reference 1, except for the last term (+ 1/2) which is incorrectly given as (- 1/4) in Reference 1. The accuracy of the averaging process is examined in Appendix D.

## A.2 SURFACE VELOCITY DISTRIBUTION FROM V_o AT α_o

Here we shall find the second part of W shown in Figure 2, namely $w_\alpha + \overline{w}_{\alpha_i}$ which is due to the free stream V_o at angle of attack α_o. The first component w_α is induced by the bound vorticity γ_α which is generated to satisfy the boundary condition and the Kutta condition, and by the wake vortex filaments $d\Gamma_{\alpha_w}$ which are shed from the duct at angle of attack. Finally, as described in Section 2, $\overline{w}_{\alpha_i}$ is self-induced by γ_α which lies on a circle.

A.2.1 Determination of w_α

The elementary velocity induced by a semi-infinite trailing vortex filament in the duct wake ($d\Gamma_{\alpha_w}$ in Fig. 2 and Sketch A.3) is given by the Biot-Savart law (p. 304, Ref. 6). Consider the radial, axial, and tangential components of the induced velocity. The variation of the radial component along the chord is negligible because the trailing vortex filaments extend to $+\infty$. Consequently, we can set $c = 0$ as in Sketch A.3. Also, there is no axial component of induced velocity, and the effect of the tangential component is considered to be negligible here (as in Ref. 1).

The radial component of velocity induced at ϕ by the vortex filament $d\Gamma_{\alpha_w}$ at ϕ' is given by (p. 304, Ref. 6)

$$-dv_{w_s} = \frac{d\Gamma_{\alpha_w}}{4\pi D \tan\left(\frac{\phi - \phi'}{2}\right)} \qquad (A.54)$$
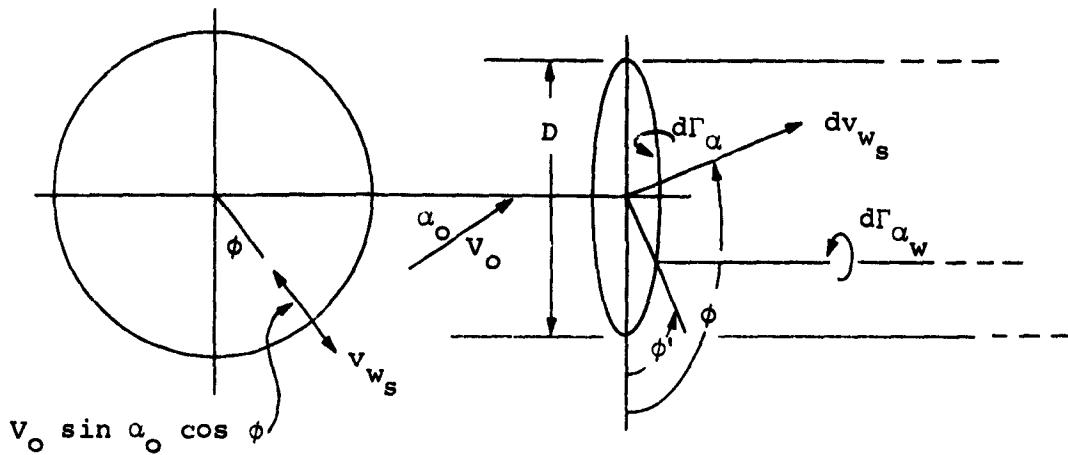
Sketch A.3.- Trailing vortex filament.

The strength of the trailing vortex filament $d\Gamma_{\alpha_w}$ is equal to
the decrease in Γ_α, the flight induced bound vorticity on the
duct, as one moves around the ring. Thus, we can write

$$dv_{w_s} = \frac{\left(\dfrac{d\Gamma_\alpha}{d\phi'}\right) d\phi'}{4\pi D \tan\left(\dfrac{\phi - \phi'}{2}\right)} \qquad (A.55)$$

Now, for a flat plate in uniform flow at angle of attack, the Kutta
condition gives the circulation as

$$\Gamma_{f_\alpha} = \pi c V_o \sin \alpha_o \qquad (A.56)$$

where $V_o \sin \alpha_o$ is the normal velocity component. The normal velocity at each chordwise strip of the duct due to both the free stream and the wake-induced velocity (Sketch A.3) is given by

$$V_o \sin \alpha_o \cos \phi - v_{w_s} \qquad (A.57)$$

Thus, the circulation about the duct chord is, from Equations (A.55) and (A.56),

$$\Gamma_\alpha = \pi c V_o \sin \alpha_o \cos \phi - \frac{c}{4D} \int_0^{2\pi} \left(\frac{d\Gamma_\alpha}{d\phi'}\right) \cot \frac{\phi - \phi'}{2} \, d\phi \qquad (A.58)$$

The method used in Reference 1 to solve this integral equation for $\Gamma_\alpha(\phi)$ is to assume initially that

$$\Gamma_\alpha = \Gamma_k \cos \phi \qquad (A.59)$$

where Γ_k is a constant, such that

$$\frac{d\Gamma_\alpha}{d\phi'} = -\Gamma_k \sin \phi' \qquad (A.60)$$

Substitution of this value and the trigonometric identity

$$\cot \frac{\phi - \phi'}{2} = \frac{1 + \cos(\phi - \phi')}{\sin(\phi - \phi')} \qquad (A.61)$$

into the integral in Equation (A.58) yields

$$\int_0^{2\pi} \sin \phi' \cot \frac{\phi - \phi'}{2} \, d\phi' = -2\pi \cos \phi \qquad (A.62)$$

Substitution of this value into Equation (A.58) then gives

$$\Gamma_k = \pi c \left(V_o \sin \alpha_o - \frac{\Gamma_k}{2D}\right) \qquad (A.63)$$

which satisfies the initial assumption that Γ_k does not depend on ϕ. Solving for Γ_k gives the ϕ variation of duct circulation from the free stream and wake when the Kutta condition is satisfied everywhere at the trailing edge. Thus, we have from Equations (A.59) and (A.63),

$$\Gamma_\alpha = \Gamma_k \cos\phi = \left(\frac{\pi c V_0 \sin\alpha_0}{1 + \frac{\pi c}{2D}}\right)\cos\phi \qquad (A.64)$$

The term $\pi c/2D$ in the denominator is due to the wake. The surface velocity distribution w_α induced on each chordwise strip of the duct by the free stream and wake is assumed to correspond with that for a flat plate at incidence so that (from Eqs. (A.78) and (A.80))

$$w_\alpha = V_0 \cos\alpha_0 + \frac{\Gamma_\alpha}{\pi c}\tan\frac{\theta}{2} \qquad (A.65)$$

and, with Equation (A.64), we find that

$$w_\alpha = V_0 \cos\alpha_0 + \frac{V_0 \sin\alpha_0}{1 + \frac{\pi c}{2D}}\cos\phi\tan\frac{\theta}{2} \qquad (A.66)$$

This equation is identical with Equation (17) of Reference 1.

A.2.2 Determination of $\overline{w}_{\alpha_i}$

Finally, the self-induced velocity $\overline{w}_{\alpha_i}$ due to the circulation Γ_α about the duct must be included. To do this, we shall first find an expression for the elementary axial velocity component induced at radius $r = D/2$ by an elementary vortex ring (Sketch A.4) having diameter D and circulation $d\Gamma_\alpha = d\Gamma_k \cos\phi'$, in accordance with Equation (A.59).
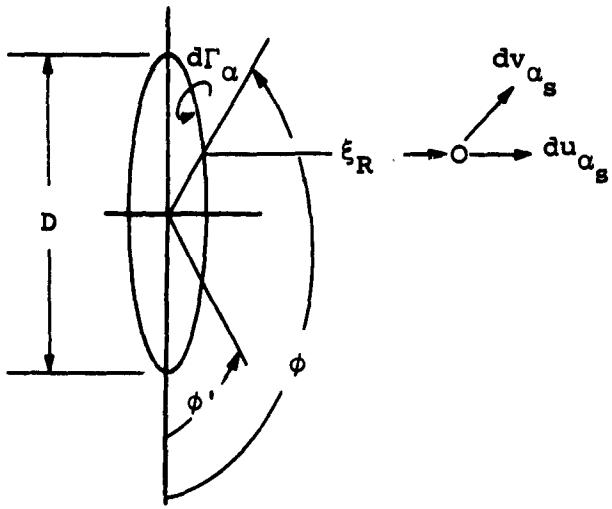
Sketch A.4.- Velocity components induced by a vortex ring
with variable strength.

Then, by using the results on pages 305 through 307 of Reference 6,
we can write

$$du_{\alpha_s} = -\frac{d\Gamma_k}{2\pi D} \int_0^{2\pi} \frac{[\cos(\phi - \phi') - 1] \cos \phi'}{\left[\dfrac{4\xi_R^2}{D^2} + 2 - 2\cos(\phi - \phi')\right]^{3/2}} \, d\phi' \qquad (A.67)$$

Further, by letting

$$k^2 \equiv \frac{1}{\dfrac{\xi_R^2}{D^2} + 1} \qquad (A.68)$$

and

$$\chi \equiv \frac{\phi - \phi' + \pi}{2} \qquad (A.69)$$

we can rewrite Equation (A.67) in the form

$$2\pi D \frac{du_{\alpha_s}}{d\Gamma_k} = \frac{k^3}{2} \int_{\frac{\phi+\pi}{2}}^{\frac{\phi-\pi}{2}} \frac{2 \cos \phi \cos^4 \chi - \cos \phi \cos^2 \chi + 2 \sin \phi \sin \chi \cos^3 \chi}{\left(1 - k^2 \sin^2 \chi \right)^{3/2}} \, d\chi$$

(A.70)

The limits of integration can now be shifted to $0 \rightarrow \pi$, and, since the last term integrates to zero, Equation (A.70) becomes

$$-2\pi D \frac{du_{\alpha_s}}{d\Gamma_k} = k^3 \cos \phi \int_0^{\pi/2} \frac{\cos^2 \chi - \frac{2}{k^2} \sin^2 \chi \left[(1 - k^2 \sin^2 \chi) + (k^2 - 1)\right]}{\left(1 - k^2 \sin^2 \chi \right)^{3/2}} \, d\chi$$

(A.71)

Now, using the relations given on page 306 of Reference 6 for the complete elliptic integrals, we find that the above equation can be written as

$$du_{\alpha_s} = \frac{-d\Gamma_\alpha}{2\pi D} \left[\left(\frac{3k^2 - 4}{k}\right) K + \left(\frac{4 - k^2}{k}\right) E \right]$$

(A.72)

where $K(k)$ and $E(k)$ are defined in the list of symbols. Finally, using the leading terms in the series expansions of K and E (Eqs. (A.8) and (A.9)) for $\xi_R \ll D$, $k^2 \approx 1$, we obtain the desired expression

$$du_{\alpha_s} = \frac{-d\Gamma_\alpha}{2\pi D} \left(3 - \ln \left| \frac{4D}{\xi_R} \right| \right)$$

(A.73)

This result is four times smaller than the corresponding expression given by Equation (19) of Reference 1. In a similar manner, it can be shown that the radial velocity component dv_{α_s} for the ring

filament is the same as for a line filament for $\xi_R \ll D$. Thus, it is not considered here, since it has already been accounted for in Equation (A.66).

Let us now find $\overline{w}_{\alpha_i}$ by the averaging process described in Section 2. The average vorticity (or circulation per unit length) along the chord length is, from Equation (A.64),

$$\overline{\gamma}_\alpha = \frac{\Gamma_\alpha}{c} = \frac{\pi V_o \sin \alpha_o}{1 + \frac{\pi c}{2D}} \cos \phi \qquad (A.74)$$

so that each elementary vortex ring (Sketch A.4) has strength

$$d\Gamma_\alpha = \overline{\gamma}_\alpha \, d\xi_R \qquad (A.75)$$

At x_s, a fixed point on the duct surface, the velocity induced by the bound vorticity $\overline{\gamma}_\alpha$ distributed over the chord is (from Eqs. (A. 73) and (A.75)):

$$\overline{u}_{\alpha_s} = -\frac{\overline{\gamma}_\alpha}{2\pi D} \int_{-\frac{c}{2} + x_s}^{\frac{c}{2} - x_s} \left(3 - \ln 4D + \ln \left|\xi_R\right|\right) d\xi_R$$

$$= -\frac{\overline{\gamma}_\alpha}{2\pi D} \left\{ (3 - \ln 4D)c + \left(\frac{c}{2} - x_s\right) \left[\ln \left(\frac{c}{2} - x_s\right) - 1\right] \right.$$

$$\left. + \left(\frac{c}{2} + x_s\right) \left[\ln \left(\frac{c}{2} + x_s\right) - 1\right] \right\} \qquad (A.76)$$

Averaging this expression over the chord gives the average induced velocity

$$\bar{w}_{\alpha_i} = \frac{1}{c} \int_{-\frac{c}{2}}^{+\frac{c}{2}} \bar{u}_{\alpha_s} \, dx_s = -\frac{\Gamma_\alpha}{2\pi D} \left(\frac{3}{2} - \ln \frac{4D}{c} \right)$$

$$= -\frac{V_0 \sin \alpha_0}{1 + \frac{\pi c}{2D}} \frac{c}{2D} \left(\frac{3}{2} - \ln \frac{4D}{c} \right) \cos \phi \qquad (A.77)$$

This result is four times smaller than the corresponding Equation (20) of Reference 1, and the term 3/2 appears here within the parentheses rather than the 9/4 of Reference 1. The accuracy of the averaging process used both here and in Reference 1 is examined in Appendix D.

A.3 SURFACE VELOCITY DUE TO PITCHING q

Here we shall find the third and last part of W indicated in Figure 2, that is, $w_q + \bar{w}_{q_i}$ which is due to the pitching motion of the duct q about its midchord diameter. Due to this motion, each chordwise strip of the duct translates horizontally and rotates about a midchord axis (Sketch A.5).
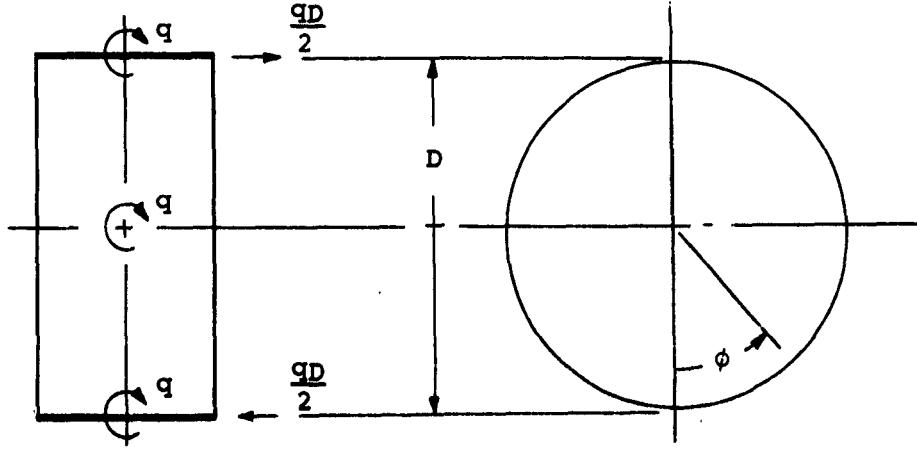
Sketch A.5.- Pitching motion of duct.

Thus, w_q will be considered in three parts:

w_{q_1} due to the rotation of each chordwise strip about its midchord axis

w_{q_2} due to the horizontal translation of each chordwise strip

w_{q_3} induced by the wake shed from the duct as described in Section 2.

Finally, $\overline{w}_{q_i}$ is self-induced by the bound vorticity γ_q which corresponds to w_q and which lies on a circle. We will neglect the effect of the yawing motion of the chordwise strips, so that for each strip w_{q_1} is due only to the pitching component of its rotation. This is consistent with Section A.2 where only the component of V_o at α_o which was normal to each strip was considered to be effective.

The final results show that the predominant effect of q is caused by w_{q_2} (the horizontal translation) when $c \ll D$. Thus, the net force and moment on the duct due to q are nearly the same as for a duct which distorts with each chordwise strip moving parallel to itself with a velocity $(qD/2) \cos \phi$ (see Sketch A.5). With the initial assumption that $c \ll D$, the flow over each chordwise strip is nearly two dimensional so that we can obtain w_q and $\overline{w}_{q_i}$ from flat-plate formulas. We shall, therefore, start the analysis by obtaining these formulas which will be useful later when we consider the flow over the chordwise strips of the duct.

A.3.1 Flat-Plate Formulas

Consider the flat plate in Sketch A.6 which is in a pure-pitch flight condition with α_0 not necessarily small,
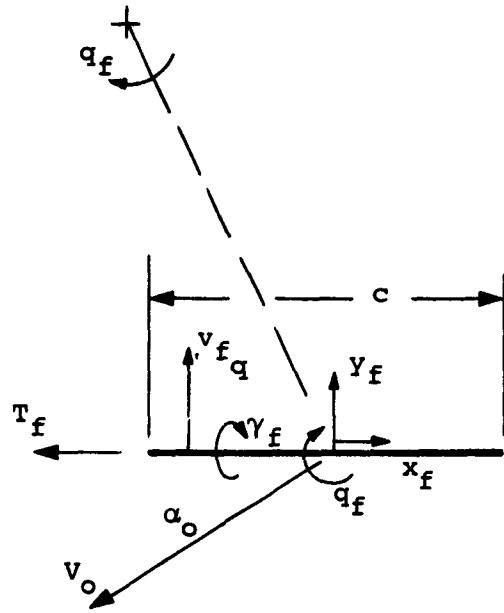
Sketch A.6.- Flat plate in pure pitch.

We wish to find the surface velocity distribution $w_f = w_{f_\alpha} + w_{f_q}$ and the bound vorticity distribution $\gamma_f = \gamma_{f_\alpha} + \gamma_{f_q}$ on the flat plate which are generated by the two parts of its motion, translation V_0 at angle α_0, and rotation q_f about its midchord axis. For the first part, V_0 at α_0, with the Kutta condition fulfilled, we have (Ref. 8, p. 38)

$$w_{f_\alpha} = V_0 \cos \alpha_0 + V_0 \sin \alpha_0 \tan \frac{\theta_f}{2} \qquad (A.78)$$

$$\gamma_{f_\alpha} = 2V_0 \sin \alpha_0 \tan \frac{\theta_f}{2} \qquad (A.79)$$

$$\Gamma_{f_\alpha} = \pi c V_0 \sin \alpha_0 \qquad (A.80)$$

and the thrust force due to leading edge suction is given by

$$T_f = \pi \rho c (V_0 \sin \alpha_0)^2 \qquad (A.81)$$

To find the second part, we shall use the well known "equivalent camber" rule as follows: The bound vorticity γ_{f_q} must induce a velocity normal to plate equal to the normal velocity component of the plate ($v_{f_q} = -qx_f$ in Sketch A.6) in order to satisfy the boundary condition of no flow through the plate. The same distribution of normal velocity is caused by a circular-arc camber (Sketch A.7) for which

$$y_c = h \left(1 - 4 \frac{x_c^2}{c^2} \right) \qquad (A.82)$$

Thus, the slope of the cambered airfoil is

$$\frac{dy_c}{dx_c} = - \frac{8h}{c^2} x_c \qquad (A.83)$$

and the normal velocity is

$$v_c = - \frac{8h}{c^2} x_c V_0 \cos \alpha_0 \qquad (A.84)$$

Thus, by equating v_c and v_{f_q}, we obtain the equivalent camber h corresponding to the pitch rate q_f of the plate. That is

$$\frac{h}{c} = \frac{q_f c}{8V_0 \cos \alpha_0} \qquad (A.85)$$

A.3.2 Determination of w_{q_1}

The pitching rate of each chordwise strip caused by pitching of the duct about its midchord diameter (Sketch A.5) is $q \cos \phi$. Therefore, using this value in Equation (A.87) for q_f gives the first component of w_q; namely,

$$w_{q_1} = \frac{\gamma_{q_1}}{2} = \frac{qc}{2} \cos \phi \sin \theta \qquad (A.88)$$

so that

$$\Gamma_{q_1} = \int_{-\frac{c}{2}}^{\frac{c}{2}} \gamma_{q_1} \, dx_s = - \int_{0}^{\pi} \gamma_{q_1} \left(\frac{c}{2} \sin \theta\right) d\theta = \left(\frac{\pi}{4} qc^2\right) \cos \phi$$

$$(A.89)$$

A.3.3 Determination of w_{q_2}

The translational velocity of each chordwise strip of the duct caused by its pitching about the midchord diameter (Sketch A.5) is $-q(D/2)\cos \phi$. This chordwise translation produces the surface velocity distribution

$$w_{q_2} = + \frac{qD}{2} \cos \phi \qquad (A.90)$$

which is clearly equal on inner and outer surface. Hence,

$$\gamma_{q_2} = \Gamma_{q_2} = 0 \qquad (A.91)$$

A.3.4 Determination of w_{q_3}

Since Γ_{q_1} varies with ϕ, there must be vortex filaments $d\Gamma_{q_w}$ which are shed parallel to the duct axis, as shown in Figure 2.

The effect of the duct wake which is generated by the q motion can therefore be found by analogy with the results obtained in Section A.2.1, since the wake due to angle of attack shows a similar character. The net duct circulation generated by the q motion is $\Gamma_q = \Gamma_{q_1}$ since Γ_{q_2} is zero; and Γ_{q_1} (Eq. (A.89)) is analogous to the first term on the right side of Equation (A.63) (where $qc/4$ now replaces $V_o \sin \alpha_o$).

Thus, we obtain the total circulation including the wake effect by analogy with Equation (A. 64):

$$\Gamma_q + \Gamma_{q_3} = \frac{\cos \phi}{1 + \frac{\pi c}{2D}} \left(\frac{\pi}{4} qc^2 \right) \tag{A.92}$$

The circulation due to the wake is (by subtraction of Eq. (A.89)):

$$\Gamma_{q_3} = - \frac{\pi c}{2D} \frac{\Gamma_q}{1 + \frac{\pi c}{2D}} \tag{A.93}$$

The q wake induces a nearly constant normal velocity over each chordwise strip of the duct, since each vortex filament in the wake extends to $+ \infty$ (Fig. 2). Thus, the chordwise distributions of surface velocity w_{q_3} and bound vorticity γ_{q_3} (i.e., $2w_{q_3}$) which compose Γ_{q_3} are (from Eqs. (A.78) and (A.80) with $\alpha_o = \pi/2$).

$$w_{q_3} = \frac{1}{2} \gamma_{q_3} = \frac{\Gamma_{q_3}}{\pi c} \tan \frac{\theta}{2} = - \frac{\pi qc^2 \cos \phi}{8D \left(1 + \frac{\pi c}{2D} \right)} \tan \frac{\theta}{2} \tag{A.94}$$

A.3.5 Determination of $\overline{w}_{q_i}$

The self induced velocity $\overline{w}_{q_i}$ due to the bound vorticity in pitch $(\gamma_q = \gamma_{q_1} + \gamma_{q_3})$ can be found by analogy with the results in Section A.2.2 for γ_α. If we replace $V_o \sin \alpha_o$ by $qc/4$, as in Section A.3.4, we obtain from Equation (A.77)

$$\overline{w}_{q_i} = -\frac{qc^2}{8D} \; \frac{\frac{3}{2} - \ln \frac{4D}{c}}{1 + \frac{\pi c}{2D}} \cos \phi \qquad (A.95)$$

APPENDIX B

INTEGRATION OF W^2 TO OBTAIN DUCT COEFFICIENTS AND DERIVATIVES

Expressions for the net force and moment on the duct will be developed here for the pure-pitch flight condition (Fig. 2) by integration of the pressure distribution p_s over its surface. These expressions are then used to obtain the static coefficients and q stability derivatives of the duct in the presence of the propeller.

The pressure distribution $p_s(\theta, \phi)$ is related to the surface velocity distribution W by the pressure equation in moving coordinates (p. 87, Ref.12) as applied to the pure-pitch motion (Fig. 2)

$$p_s = p_o + \frac{\rho}{2}\left(V_o^2 - W^2 - V_s^2\right) \qquad (B.1)$$

where V_s is the velocity (in a fixed frame of reference) of the point in question on the duct surface. Since the first two terms on the right side are constant over the duct surface, they do not contribute to the net force $N_{D(P)}$ or moment $\left(M_N\right)_{D(P)}$. Furthermore, the velocity V_s is the same on the inner and outer surface and hence does not contribute to $N_{D(P)}$ or $\left(M_N\right)_{D(P)}$. Thus, the duct force and moment can be found by substituting $-(\rho/2)W^2$ for p_s in the following expressions:

$$N_{D(P)} = \oint p_s \, dx_s \, \frac{D}{2} \cos\phi \, d\phi = -\frac{cD}{4} \int_0^{2\pi} \int_0^{2\pi} p_s \sin\theta \cos\phi \, d\theta \, d\phi$$

$$(B.2)$$

$$\left(M_N\right)_{D(P)} = -\oint p_s x_s \, dx_s \, \frac{D}{2} \cos \phi \, d\phi$$

$$= +\frac{c^2 D}{8} \int_0^{2\pi} \int_0^{2\pi} p_s \cos \theta \sin \theta \cos \phi \, d\theta \, d\phi \qquad (B.3)$$

The duct force and moment due to leading-edge suction T are given by

$$T_D = \int_0^{2\pi} \frac{D}{2} \, (T) \, d\phi \qquad (B.4)$$

$$\left(M_T\right)_{D(P)} = \int_0^{2\pi} \frac{D}{2} \, (T) \, \frac{D}{2} \cos \phi \, d\phi \qquad (B.5)$$

where T will be evaluated subsequently. The net moment on the duct in the presence of the propeller (Fig. 1a) is then

$$M_{D(P)} = \left(M_N\right)_{D(P)} + \left(M_T\right)_{D(P)} \qquad (B.6)$$

Let us proceed by finding W^2 and integrating it over the duct surface to obtain Equations (B.33) and (B.35) for $N_{D(P)}$ and $\left(M_N\right)_{D(P)}$ as functions of α_o and qD/V_o. Finally, T_D and $\left(M_T\right)_{D(P)}$ are evaluated in Section B.4.

B.1 INTEGRATION OF W^2 TO FIND DUCT FORCE AND MOMENT

The surface velocity distribution on the duct during pure-pitch flight from Equation (7) is

$$W = w_h + \overline{w}_{h_i} + w_\alpha + \overline{w}_{\alpha_i} + w_q + \overline{w}_{q_i} \qquad (B.7)$$

where

$$w_q = w_{q_1} + w_{q_2} + w_{q_3} \qquad (B.8)$$

and the components are given by the following equations:

$w_h + \bar{w}_{h_i}$	$\bar{w}_{h_i}$	w_α	$\bar{w}_{\alpha_i}$	w_{q_1}	w_{q_2}	w_{q_3}	$\bar{w}_{q_i}$
(A.1)	(A.53)	(A.66)	(A.77)	(A.88)	(A.90)	(A.94)	(A.95)

By substitution of these equations, we can write

$$W = \frac{\gamma}{2\pi} f_1(\theta) + f_2(\theta) \cos \phi + c_1 \qquad (B.9)$$

where

$$f_1(\theta) = -\theta + \frac{c}{2D} (1 - \cos \theta) \ln \frac{c}{8D} (1 - \cos \theta)$$

$$- \left(2 + \ln \frac{c}{16D}\right) \tan \frac{\theta}{2} \qquad (B.10)$$

$$f_2(\theta) = c_2 \tan \frac{\theta}{2} + \frac{qc}{2} \sin \theta + c_3 \qquad (B.11)$$

$$c_1 = \bar{w}_{h_i} + V_o \cos \alpha_o + \frac{3\gamma}{4} \qquad (B.12)$$

$$c_2 = \frac{V_o \sin \alpha_o - (\pi q c^2 / 8D)}{1 + (\pi c / 2D)} \qquad (B.13)$$

$$c_3 = \frac{qD}{2} + \frac{\bar{w}_{\alpha_i} + \bar{w}_{q_i}}{\cos \phi} \qquad (B.14)$$

and the c's do not depend on ϕ or θ.

The duct normal force and pitching moment, from Equations (B.2) and (B.3) are given by

$$N_{D(P)} = \frac{\rho c D}{8} \int_0^{2\pi} \sin\theta \, d\theta \int_0^{2\pi} W^2 \cos\phi \, d\phi \qquad (B.15)$$

$$= \frac{\rho c A}{D} \int_0^{2\pi} f_2(\theta) \left[\frac{\gamma}{2\pi} f_1(\theta) + c_1 \right] \sin\theta \, d\theta \qquad (B.16)$$

and

$$\left(M_N\right)_{D(P)} = -\frac{\rho c^2 D}{16} \int_0^{2\pi} \cos\theta \sin\theta \, d\theta \int_0^{2\pi} W^2 \cos\phi \, d\phi \qquad (B.17)$$

$$= -\frac{\rho c^2 A}{2D} \int_0^{2\pi} f_2(\theta) \left[\frac{\gamma}{2\pi} f_1(\theta) + c_1 \right] \cos\theta \sin\theta \, d\theta \qquad (B.18)$$

Note that terms which integrate to zero have been omitted in the above expressions. We shall now evaluate the remaining integrals by letting $2\beta \equiv \theta$ and making use of the expressions which follow them.

$$I_1 = \int_0^{2\pi} c_1 f_2 \sin\theta \, d\theta$$

$$= c_1 \int_0^{2\pi} \left[c_2(1 - \cos\theta) + \frac{qc}{2} \sin^2\theta + c_3 \sin\theta \right] d\theta$$

$$= 2\pi c_1 \left(c_2 + \frac{qc}{4} \right) \qquad (B.19)$$

$$I_2 = \int_0^{2\pi} c_1 f_2 \cos\theta \sin\theta \, d\theta = -\pi c_1 c_2 \qquad (B.20)$$

$$I_3 = \int_0^{2\pi} \frac{\gamma}{2\pi} f_1 f_2 \sin \theta \, d\theta \qquad\qquad (B.21)$$

$$I_3 = \frac{\gamma}{2\pi} \int_0^{2\pi} \left[-\theta + \frac{c}{2D} (1 - \cos \theta) \ln \frac{c}{8D} (1 - \cos \theta) \right.$$
$$\left. - \left(2 + \ln \frac{c}{16D}\right) \tan \frac{\theta}{2} \right] \left[c_2 (1 - \cos \theta) + \frac{qc}{2} \sin^2\theta + c_3 \sin \theta \right] d\theta$$
$$\qquad\qquad (B.22)$$

$$I_3 = \frac{2\gamma}{\pi} \int_0^{2\pi} \left[-2\beta + \left(\frac{c}{D} \ln \frac{c}{4D}\right) \sin^2\beta + \frac{2c}{D} \sin^2\beta \, \ln \sin \beta \right.$$
$$\left. - \left(2 + \ln \frac{c}{16D}\right) \frac{\sin \beta}{\cos \beta} \right] \left[(c_2 + qc) \sin^2\beta - qc \sin^4\beta \right.$$
$$\left. + c_3 \sin \beta \cos \beta \right] d\beta \qquad\qquad (B.23)$$

$$I_3 = \frac{2\gamma}{\pi} \left\{ \begin{array}{l} -2 \int_0^{\pi} \left[(c_2 + qc)\beta \sin^2\beta - qc\beta \sin^4\beta + c_3\beta \sin \beta \cos \beta \right] d\beta \\[2em] + \frac{c}{D} \ln \frac{c}{4D} \int_0^{\pi} \left[(c_2 + qc) \sin^4\beta - qc \sin^6\beta \right] \\[2em] + \frac{2c}{D} \int_0^{\pi} \left[(c_2 + qc) \sin^4\beta - qc \sin^6\beta \right] \ln \sin \beta \, d\beta \\[2em] - \left(2 + \ln \frac{c}{16D}\right) \int_0^{\pi} c_3 \sin^2\beta \, d\beta \end{array} \right.$$

$$\qquad\qquad (B.24)$$

$$I_3 = 2\gamma \left\{ (c_2 + qc) \left[-\frac{\pi}{2} + \frac{c}{8D} \left(3 \ln \frac{c}{16D} + \frac{7}{2} \right) \right] + qc \left[\frac{3\pi}{8} \right. \right.$$

$$\left. \left. - \frac{c}{16D} \left(5 \ln \frac{c}{16D} + \frac{37}{6} \right) \right] - c_3 \frac{1}{2} \left(1 + \ln \frac{c}{16D} \right) \right\}$$

$$= c_2 \left[-\gamma\pi + \frac{3\gamma c}{4D} \left(\ln \frac{c}{16D} + \frac{7}{6} \right) \right] + \frac{qc}{4} \left[-\gamma\pi + \frac{\gamma c}{2D} \left(\ln \frac{c}{16D} + \frac{5}{6} \right) \right]$$

$$- \left(\frac{qD}{2} + \frac{w_{\alpha_i} + w_{q_i}}{\cos \phi} \right) \gamma \left(1 + \ln \frac{c}{16D} \right) \qquad (B.25)$$

$$I_4 = \frac{\gamma}{2\pi} \int_0^{2\pi} f_1 f_2 \sin \theta \cos \theta \, d\theta \qquad (B.26)$$

$$I_4 = \frac{2\gamma}{\pi} \int_0^{2\pi} f_1 \left[(c_2 + qc)(\sin^2\beta - 2 \sin^4\beta) - qc(\sin^4\beta - 2 \sin^6\beta) \right.$$

$$\left. + c_3 (\sin \beta - 2 \sin^3\beta) \cos \beta \right] d\beta \qquad (B.27)$$

$$I_4 = \frac{2\gamma}{\pi} \int_0^{\pi} \left[-2\beta + \left(\frac{c}{D} \ln \frac{c}{4D} \right) \sin^2\beta + \frac{2c}{D} \sin^2\beta \ln \sin \beta \right.$$

$$\left. - \left(2 + \ln \frac{c}{16D} \right) \frac{\sin \beta}{\cos \beta} \right] \left[(c_2 + qc) \sin^2\beta - (2c_2 + 3qc) \sin^4\beta \right.$$

$$\left. + 2qc \sin^6\beta + c_3 (\sin \beta - 2 \sin^3\beta) \cos \beta \right] d\beta \qquad (B.28)$$

$$
I_4 = \frac{2\gamma}{\pi} \left\{
\begin{aligned}
&-2 \int_0^\pi \left[(c_2 + qc)\beta \sin^2\beta - (2c_2 + 3qc)\beta \sin^4\beta + 2qc\,\beta \sin^6\beta \right. \\
&\left. + c_3(\beta \sin\beta - 2\beta \sin^3\beta)\cos\beta \right] d\beta \\[6pt]
&+ \frac{c}{D} \ln \frac{c}{4D} \int_0^\pi \left[(c_2+qc)\sin^4\beta - (2c_2+3qc)\sin^6\beta + 2qc\,\sin^8\beta \right] d\beta \\[6pt]
&+ \frac{2c}{D} \int_0^\pi \left[(c_2+qc)\sin^4\beta - (2c_2+3qc)\sin^6\beta + 2qc\,\sin^8\beta \right] \ln\sin\beta\, d\beta \\[6pt]
&- \left(2 + \ln \frac{c}{16D}\right) \int_0^\pi + c_3\left(\sin^2\beta - 2\sin^4\beta\right) d\beta
\end{aligned}
\right.
$$

$$
\text{(B.29)}
$$

$$
I_4 = 2\gamma \left\{ (c_2 + qc)\left[-\frac{\pi}{2} + \frac{c}{16D}\left(6 \ln \frac{c}{16D} + 7\right) \right] + (2c_2 + 3qc)\left[\frac{3\pi}{8} \right.\right.
$$

$$
\left. + \frac{c}{16D}\left(-5 \ln \frac{c}{16D} - \frac{37}{6}\right) \right] + qc\left[-\frac{5}{8}\pi + \frac{c}{16D}\left(35 \ln \frac{c}{16D} + \frac{533}{12}\right) \right]
$$

$$
\left. + \frac{c_3}{4}\left(\frac{5}{2} + \ln \frac{c}{16D}\right) \right\}
\qquad \text{(B.30)}
$$

$$
I_4 = \gamma \left\{ c_2\left[\frac{\pi}{2} - \frac{c}{2D}\left(\ln \frac{c}{16D} + \frac{4}{3}\right) \right] - \frac{qc^2}{32D}\left(\ln \frac{c}{16D} + \frac{19}{12}\right) + \frac{c_3}{2}\left(\frac{5}{2} + \ln \frac{c}{16D}\right) \right\}
$$

$$
\text{(B.31)}
$$

The following expressions have been used in evaluating the above integrals:

$$\int_0^{\pi} \beta \sin^m \beta \, d\beta = \frac{m-1}{m} \int_0^{\pi} \beta \sin^{m-2} \beta \, d\beta$$

$$\int_0^{\pi} \beta \sin^2 \beta \, d\beta = \frac{\pi^2}{4}$$

$$\int_0^{\pi} \beta \sin^4 \beta \, d\beta = \frac{3\pi^2}{16}$$

$$\int_0^{\pi} \beta \sin^6 \beta \, d\beta = \frac{5\pi^2}{32}$$

$$\int_0^{\pi} \beta \sin^8 \beta \, d\beta = \frac{35\pi^2}{256}$$

$$\int_0^{\pi} \beta \cos \beta \sin \beta \, d\beta = -\frac{\pi}{4}$$

$$\int_0^{\pi} \beta \cos \beta \sin^3 \beta \, d\beta = -\frac{3\pi}{32}$$

$$\int_0^{\pi} \beta \cos \beta \sin^5 \beta \, d\beta = -\frac{5\pi}{96}$$

$$\int_0^{\pi} \sin^m \beta \; d\beta = \frac{m-1}{m} \int_0^{\pi} \sin^{m-2} \beta \; d\beta$$

$$\int_0^{\pi} \sin^2 \beta \; d\beta = \frac{\pi}{2}$$

$$\int_0^{\pi} \sin^4 \beta \; d\beta = \frac{3\pi}{8}$$

$$\int_0^{\pi} \sin^6 \beta \; d\beta = \frac{5\pi}{16}$$

$$\int_0^{\pi} \sin^8 \beta \; d\beta = \frac{35\pi}{128}$$

$$\int_0^{\pi} \sin^m \beta \cos \beta \; d\beta = 0 \quad \text{from symmetry}$$

$$\int_0^{\pi} \frac{\sin^7 \beta}{\cos \beta} \; d\beta = \int_0^{\pi} \frac{\sin^5 \beta}{\cos \beta} \; d\beta = \int_0^{\pi} \frac{\sin^3 \beta}{\cos \beta} \; d\beta$$

$$= \int_0^{\pi} \frac{\sin \beta}{\cos \beta} \; d\beta = - \ln \left| \cos \beta \right| \Big]_0^{\pi} = 0 \quad \text{from symmetry}$$

$$\int_0^\pi \sin^k \beta \, \ln \sin \beta \, d\beta = \frac{\sqrt{\pi} \, \Gamma\left(\frac{k+1}{2}\right)}{2\Gamma\left(\frac{k+2}{2}\right)} \left[\psi\left(\frac{k+1}{2}\right) - \psi\left(\frac{k+2}{2}\right) \right]$$

$$\int_0^\pi \sin^4 \beta \, \ln \sin \beta \, d\beta = \frac{\sqrt{\pi} \, \Gamma(5/2)}{2\Gamma(3)} \left[\psi\left(\frac{5}{2}\right) - \psi(3) \right]$$

$$= \frac{\pi}{16}\left(-3 \ln 4 + \frac{7}{2} \right)$$

$$\int_0^\pi \sin^6 \beta \, \ln \sin \beta \, d\beta = \frac{\sqrt{\pi} \, \Gamma(7/2)}{2\Gamma(4)} \left[\psi\left(\frac{7}{2}\right) - \psi(4) \right]$$

$$= \frac{\pi}{32}\left(-5 \ln 4 + \frac{37}{6} \right)$$

$$\int_0^\pi \sin^8 \beta \, \ln \sin \beta \, d\beta = \frac{\sqrt{\pi} \, \Gamma(9/2)}{2\Gamma(5)} \left[\psi\left(\frac{9}{2}\right) - \psi(5) \right]$$

$$= \frac{\pi}{256}\left(-35 \ln 4 + \frac{533}{12} \right)$$

where

$$\Gamma\left(n + \frac{1}{2}\right) = 1 \ldots\ldots\ldots (2n-1) \frac{\sqrt{\pi}}{2n}$$

$$\Gamma(n) = (n-1)! \quad n \text{ is an integer } > 0$$

$$\psi(n+1) = -\epsilon + 1 + \frac{1}{2} + \ldots\ldots\ldots + \frac{1}{n}$$

$$\psi\left(\frac{1}{2}\right) = -\epsilon - \ln 4$$

$$\psi\left(\frac{3}{2}\right) = -\epsilon - \ln 4 + 2$$

$$\psi\left(\frac{5}{2}\right) = -\epsilon - \ln 4 + \frac{8}{3}$$

$$\psi\left(\frac{7}{2}\right) = -\epsilon - \ln 4 + \frac{46}{15}$$

$$\psi\left(\frac{9}{2}\right) = -\epsilon - \ln 4 + \frac{352}{105}$$

ϵ = Euler's constant

$$\int_0^\pi \sin^m \beta (\ln \sin \beta) \cos \beta \, d\beta = 0 \quad \text{from symmetry}$$

$$\cos \theta (1 - \cos \theta) = 2 \sin^2 \beta - 4 \sin^4 \beta$$

$$\sin^2 \theta \cos \theta = 4(\sin^2 \beta - 3 \sin^4 \beta + 2 \sin^6 \beta)$$

$$\sin \theta \cos \theta = 2(\sin \beta - 2 \sin^3 \beta) \cos \beta$$

By substitution of the above expressions into Equations (B.16) and (B.18) we obtain finally the duct normal force

$$N_{D(P)} = \frac{\rho cA}{D} \left\{ c_2 \left[2\pi c_1 - \gamma\pi + \frac{3\gamma c}{4D}\left(\ln \frac{c}{16D} + \frac{7}{6} \right) \right] + \frac{qc}{4}\left[2\pi c_1 - \gamma\pi \right.\right.$$

$$\left.\left. + \frac{\gamma c}{2D}\left(\ln \frac{c}{16D} + \frac{5}{6} \right) \right] - \gamma \left(q\frac{D}{2} + \frac{\overline{w}_{\alpha_i} + \overline{w}_{q_i}}{\cos \phi} \right)\left(1 + \ln \frac{c}{16D} \right) \right\} \quad \text{(B.32)}$$

$$N_{D(P)} = \frac{2\rho cAV_o}{D} \left\{ \frac{\sin \alpha_o - (\pi qc^2/8V_o D)}{1 + (\pi c/2D)} \left[\pi\left(\overline{w}_{h_i} + V_o \cos \alpha_o + \frac{\gamma}{4} \right) \right.\right.$$

$$\left. + \frac{3\gamma c}{8D}\left(\ln \frac{c}{16D} + \frac{7}{6} \right) \right] - \frac{\gamma}{2}\left(\frac{Dq}{2V_o} + \frac{\overline{w}_{\alpha_i} + \overline{w}_{q_i}}{V_o \cos \phi} \right)\left(1 + \ln \frac{c}{16D} \right)$$

$$\left. + \frac{qc}{4V_o}\left[\pi\left(\overline{w}_{h_i} + V_o \cos \alpha_o + \frac{\gamma}{4} \right) + \frac{\gamma c}{4D}\left(\frac{5}{6} + \ln \frac{c}{16D} \right) \right] \right\} \quad \text{(B.33)}$$

and the duct moment due to $N_{D(P)}$

$$\left(M_N\right)_{D(P)} = -\frac{\rho c^2 A}{2D} \left\{ c_2 \left[-\pi c_1 + \frac{\gamma \pi}{2} - \frac{\gamma c}{2D}\left(\ln\frac{c}{16D} + \frac{4}{3}\right)\right]\right.$$

$$\left. - \frac{\gamma q c^2}{32D}\left(\ln\frac{c}{16D} + \frac{19}{12}\right) + c_3 \frac{\gamma}{2}\left(\frac{5}{2} + \ln\frac{c}{16D}\right)\right\} \qquad (B.34)$$

$$\left(M_N\right)_{D(P)} = \frac{\rho c^2 A V_o \gamma}{4D}\left\{ \frac{\sin\alpha_o - (\pi q c^2/8V_o D)}{1 + (\pi c/2D)}\left[\frac{2\pi}{\gamma}\left(\overline{w}_{h_i} + V_o \cos\alpha_o + \frac{\gamma}{4}\right)\right.\right.$$

$$\left.\left. + \frac{c}{D}\left(\ln\frac{c}{16D} + \frac{4}{3}\right)\right] + \frac{q c^2}{16V_o D}\left(\ln\frac{c}{16D} + \frac{19}{12}\right)\right.$$

$$\left. - \left(\frac{Dq}{2V_o} + \frac{\overline{w}_{\alpha_i} + \overline{w}_{q_i}}{V_o \cos\phi}\right)\left(\ln\frac{c}{16D} + \frac{5}{2}\right)\right\} \qquad (B.35)$$

B.2 STATIC (α) COEFFICIENTS OF DUCT

As described in Section 2, we find the static (α) coefficients of the duct by setting $q = 0$ in Equations (B.33) and (B.35). This gives

$$\left(C_N\right)_{D(P)}(\alpha_o,0,0) = 4\frac{c}{D}\left\{\frac{\sin\alpha_o}{1 + (\pi c/2D)}\left[\pi\frac{\overline{w}_{h_i}}{V_o} + \pi\cos\alpha_o + \pi\frac{\gamma}{4V_o}\right.\right.$$

$$\left.\left. + \frac{3c\gamma}{8DV_o}\left(\ln\frac{c}{16D} + \frac{7}{6}\right)\right] - \frac{\gamma\overline{w}_{\alpha_i}}{2V_o^2\cos\phi}\left(1 + \ln\frac{c}{16D}\right)\right\}$$

$$(B.36)$$

and

$$\left(C_{M_N}\right)_{D(P)} (\alpha_o, 0, 0) = \frac{c^2}{D^2} \left\{ \frac{\sin \alpha_o}{1 + (\pi c/2D)} \left[2\pi \left(\frac{\bar{w}_{h_i}}{V_o} + \cos \alpha_o \right) + \frac{\pi \gamma}{2V_o} \right. \right.$$

$$\left. \left. + \frac{c}{D} \left(\ln \frac{c}{16D} + \frac{4}{3} \right) \frac{\gamma}{V_o} \right] - \frac{\bar{w}_{\alpha_i}}{V_o \cos \phi} \left(\ln \frac{c}{16D} + \frac{5}{2} \right) \frac{\gamma}{V_o} \right\}$$

$$(B.37)$$

Equation (B.36) is identical with Equation 28 of Reference 1 except for the addition of the amount $\left(\frac{7}{16} - \frac{3}{8} \ln 2 \right) \frac{c\gamma}{DV_o}$ in the square bracket. Equation (B.37) is identical with Equation 30 of Reference 1 except for the sign of the $\bar{w}_{h_i}$ term and the addition of the amount $\left(\frac{4}{3} - \ln 2 \right) \frac{c\gamma}{DV_o}$ in the square bracket. All of these differences appear only in higher order terms in c/D which will be dropped later.

B.3 DUCT q DERIVATIVES

As described in Section 2, we find the q derivatives of the duct by differentiating Equations (B.33) and (B.35) with respect to Dq/V_o holding V_o and α_o constant. After substitution of Equations (A.53) and (A.77) for w_{h_i} and w_{α_i} this gives

$$\left(C_{N_q}\right)_{D(P)} = -\frac{(\pi c^3/2D^3)\gamma}{\left(1 + \frac{\pi c}{2D}\right)V_o} \left[\frac{V_o}{\gamma} \pi \cos \alpha_o + \frac{1}{4} + \frac{c}{4D} \left(\ln \frac{16D}{c} - 1 \right) \left(\ln \frac{4D}{c} \right. \right.$$

$$\left. \left. + \frac{1}{2} \right) - \frac{3c}{8D} \ln \frac{16D}{c} + \frac{7c}{16D} \right] + \frac{\gamma c}{V_o D} \left(\ln \frac{16D}{c} - 1 \right) + \frac{\pi \gamma c^2}{4V_o D^2}$$

$$- \frac{\gamma c^3}{4V_o D^3} \left(\ln \frac{16D}{c} - 1 \right) \frac{\frac{3}{2} - \ln \frac{4D}{c}}{1 + \frac{\pi c}{2D}} - \frac{c^3 \gamma}{4D^3 V_o} \left[+ \ln \frac{16D}{c} - \frac{5}{6} \right.$$

$$\left. - \left(\ln \frac{16D}{c} - 1 \right) \left(\ln \frac{4D}{c} + \frac{1}{2} \right) \right] + \frac{\pi c^2}{D^2} \cos \alpha_o \qquad (B.38)$$

$$\left(C_{m_{N_q}}\right)_{D(P)} = \frac{\gamma c^2}{V_o D^2}\left\{-\frac{\pi^2 c^2 V_o \cos\alpha_o}{4D^2\gamma\left(1 + \frac{\pi c}{2D}\right)} \underline{-\frac{5}{4} + \frac{1}{2}\ln\frac{16D}{c}}\right.$$

$$+ \frac{c^2}{8D^2}\left(\frac{5}{2} - \ln\frac{16D}{c}\right)\frac{\frac{3}{2} - \ln\frac{4D}{c}}{1 + \frac{\pi c}{2D}} - \frac{\pi c^2/8D^2}{1 + \frac{\pi c}{2D}}\left[\frac{\pi}{2} + \frac{c}{2D}\cdot\right.$$

$$\left.\left(\ln\frac{16D}{c} - 1\right)\left(\ln\frac{4D}{c} + \frac{1}{2}\right) + \frac{c}{D}\left(-\ln\frac{16D}{c} + \frac{4}{3}\right)\right]$$

$$\left.- \frac{c^2}{16D^2}\left(\ln\frac{16D}{c} - \frac{19}{12}\right)\right\} \tag{B.39}$$

Only the leading terms in Equations (B.38) and (B.39) will be used in the subsequent analysis. These are of lowest order in c/D and are underlined.

B.4 DUCT FORCE AND MOMENT DUE TO LEADING-EDGE SUCTION

The thrust force $T_{D(P)}$ and moment $\left(M_T\right)_{D(P)}$ on the duct arising from leading suction will now be determined. The only parts of W in Equation (B.7) which are singular at the leading edge are w_h, w_α, and w_{q_3}, which are proportional to $\tan(\theta/2)$. Hence by analogy with the flat-plate formulas (Eqs. (A.78) and (A.81)) we find that the thrust force on each chordwise strip of the duct is proportional to the square of the coefficient of the singularity and is given by

$$T = \pi\rho c\left[\frac{\gamma}{2\pi}\left(\ln\frac{16D}{c} - 2\right) + \frac{\left(V_o\sin\alpha_o - \frac{\pi q c^2}{8D}\right)\cos\phi}{1 + \frac{\pi c}{2D}}\right]^2 \tag{B.40}$$

The total thrust force on the duct is obtained by integrating with respect to ϕ. Thus from Equation (B.4) we find

$$T_{D(P)} = \frac{cD}{2} \left(\frac{\rho\gamma^2}{2} \right) \left(\ln \frac{16D}{c} - 2 \right)^2$$

$$+ \pi^2 cD \left(\frac{\rho V_o^2}{2} \right) \left(\frac{\sin \alpha_o - \frac{\pi q c^2}{8DV_o}}{1 + \frac{\pi c}{2D}} \right)^2 \tag{B.41}$$

The corresponding moment on the duct, from Equation (B.5), is given by

$$\left(M_T \right)_{D(P)} = \frac{\rho A \gamma c}{1 + \frac{\pi c}{2D}} \left(V_o \sin \alpha_o - \frac{\pi q c^2}{8D} \right) \left(\ln \frac{16D}{c} - 2 \right) \tag{B.42}$$

APPENDIX C

VARIATION OF ACTUATOR-DISK LOCATION

To determine the effect of actuator-disk location upon the net aerodynamic reaction on the duct, we shall calculate the surface vorticity distribution γ_h during hovering flight for two alternate disk locations, the duct leading edge and midchord. It is recalled that the actuator disk was assumed to be at the duct trailing edge in Section 3.

The leading-edge location is considered first. In this case it can be seen (Sketch A.1) that Equation (A.14) is replaced by

$$x_s = \xi_t - \frac{c}{2} \tag{C.1}$$

By following through the analysis in Section A.1 with this modification we find that the equations therein are changed slightly as indicated below.

Equations (A.15) and (A.16) become

$$u_{\gamma_s} = \frac{\gamma}{2\pi} \left\{ \frac{\pi}{2} - \frac{c}{2D} (\cos\theta + 1) \ln\left[\frac{c}{8D} (\cos\theta + 1)\right] \right\} \tag{C.2}$$

$$v_{\gamma_s} = \frac{\gamma}{2\pi} \left\{ 2 + \ln\left[\frac{c}{8D} (\cos\theta + 1)\right] \right\} \tag{C.3}$$

C-2

Substitution of $\beta = \theta + \pi$ into the identity used to obtain Equation (A.26) gives

$$\ln(1 + \cos \beta) = -\ln 2 - 2 \sum_{n=1}^{\infty} \frac{1}{n} (-1)^n \cos n\beta \qquad (C.4)$$

By use of this, Equation (A.16) can be written

$$v_{\gamma_s} = \frac{\gamma}{2\pi} \left(2 - \ln \frac{16D}{c}\right) \sin \theta - \frac{\gamma}{2\pi} \sum_{n=1}^{\infty} \frac{2}{n} (-1)^n \cos n\theta \sin \theta \qquad (C.5)$$

and Equation (A.26) becomes

$$v_{\gamma_s} \sin \theta = \frac{\gamma}{2\pi} \left\{ \left(2 - \ln \frac{16D}{c}\right) \sin \theta \right.$$

$$\left. - \sum_{n=1}^{\infty} \frac{1}{n} (-1)^n \left[\sin(n + 1)\theta - \sin(n - 1)\theta\right] \right\} \qquad (C.6)$$

Thus the factor $(-1)^{n+1}$ is inserted into the summation symbol in Equations (A.32) and (A.33). Using $\theta = \beta + \pi$ in the identity from Reference 22, we obtain

$$\sum_{n=1}^{\infty} \frac{(-1)^n \sin n\beta}{n} = -\frac{\beta}{2} \qquad (C.7)$$

when

$$-\pi \leq \beta \leq \pi$$

Multiplying by $(\cos \beta + 1)$, reducing and re-indexing gives the identity

$$\sum_{n=2}^{\infty} \frac{(-1)^{n+1} \sin n\beta}{n(n^2 - 1)} = + \frac{3}{4} \sin \beta - (\cos \beta + 1) \frac{\beta}{2} \qquad (C.8)$$

when

$$-\pi \leq \beta \leq \pi$$

By use of this, the main equations in the series, Equations (A.33) through (A.47) become

$$\Phi_s' = - \frac{\Gamma_h \theta}{2\pi} + \frac{\gamma c}{2\pi} \left[-\frac{\theta}{2} (\cos \theta + 1) + \frac{3}{4} \sin \theta \right] + a_1 \sin \theta \qquad (C.9)$$

$$w_{F_s}' = - \frac{\Gamma_h}{2\pi} + \frac{\gamma c}{2\pi} \left[- \frac{1 + \cos \theta}{2} + \frac{\theta}{2} \sin \theta + \frac{3}{4} \cos \theta \right.$$

$$\left. + \left(\frac{1}{2} \ln \frac{16D}{c} - \frac{5}{4} \right) \cos \theta \right] \qquad (C.10)$$

$$w_{F_t}' = - \frac{\Gamma_h}{2\pi} - \frac{\gamma c}{4\pi} \left(3 - \ln \frac{16D}{c} \right) \qquad (C.11)$$

$$u_{\gamma_t} = \frac{\gamma}{2\pi} \left(\frac{\pi}{2} + \frac{c}{D} \ln \frac{4D}{c} \right) \qquad (C.12)$$

$$v_{\gamma_t} = \frac{\gamma}{2\pi} \left(2 - \ln \frac{4D}{c} \right) \qquad (C.13)$$

$$\frac{\Gamma_h}{2\pi} = \frac{\gamma c}{4\pi}\left(\ln\frac{16D}{c} - 3\right) \tag{C.14}$$

$$w_{F_s} = -\frac{\gamma}{2\pi}\left(2 - \ln\frac{16D}{c}\tan\frac{\theta}{2} + \theta\right) \tag{C.15}$$

Finally Equation (A.50) for the bound vorticity distribution along the duct chord becomes (with the actuator disk at the duct leading edge)

$$\gamma_h = \frac{\gamma}{\pi}\left[\left(\ln\frac{16D}{c} - 2\right)\tan\frac{\theta}{2} - \theta\right] \tag{C.16}$$

where

$$0 \le \theta \le \pi$$

Now following through the analysis in Section A.1 with the disk _at the midchord_ of the duct, we find that the equations in Section A.1 are changed as follows. Equation (A.14) becomes

$$x_s = \xi_t \tag{C.17}$$

With this modification Equations (A.15) and (A.16) become

$$u_{\gamma_s} = \frac{\gamma}{2\pi}\left[\frac{\pi}{2} + \frac{c}{2D}\cos\theta\left(\frac{1}{2}\ln\cos^2\theta - \ln\frac{8D}{c}\right)\right] \tag{C.18}$$

$$v_{\gamma_s} = \frac{\gamma}{2\pi}\left(2 + \frac{1}{2}\ln\cos^2\theta - \ln\frac{8D}{c}\right) \tag{C.19}$$

Using the identity from page 188, Reference 22,

$$-\sum_{n=1}^{\infty}\frac{(-1)^n}{n}\cos 2n = \frac{1}{2}\ln(4\cos^2\theta) = \ln 2 + \frac{1}{2}\ln\cos^2\theta \tag{C.20}$$

we can write

$$v_{\gamma_s} \sin \theta = \frac{\gamma}{2\pi} \left[\left(2 - \ln \frac{16D}{c} \right) \sin \theta - \sum_{n=1}^{\infty} \frac{(-1)^n}{n} \cos 2n\theta \, \sin \theta \right] \quad (C.21)$$

$$\left. \begin{array}{l} a_o = a_n \quad \text{for even} \quad n = 0 \\[3mm] a_1 = -\frac{\gamma c}{4\pi} \left(\frac{3}{2} - \ln \frac{16D}{c} \right) \\[3mm] a_n = -\frac{\gamma c (-1)^n}{4\pi 2n(n-1)} \quad \text{for odd} \quad n > 1 \end{array} \right\} \quad (C.22)$$

$$\Phi_s' = -\frac{\Gamma_h \theta}{2\pi} - \frac{\gamma c}{4\pi} \left[\sum_{n=2}^{\infty} \frac{(-1)^n \sin(2n-1)\theta}{2n(n-1)} + \left(\frac{3}{2} - \ln \frac{16D}{c} \right) \sin \theta \right] \quad (C.23)$$

Using the series from page 188, Reference 22,

$$\sum_{n=1}^{\infty} \frac{1}{n} \sin n\beta = \frac{\pi - \beta}{2} \quad (C.24)$$

for

$$0 \leq \beta \leq 2\pi$$

and letting $\beta = \theta + \pi$, we obtain

$$\sum_{n=1}^{\infty} \frac{(-1)^n \sin 2n\theta}{n} = -\theta \quad (C.25)$$

for

$$\frac{\pi}{2} \leq \theta \leq \frac{\pi}{2}$$

Forming the product $-\theta \cos \theta$ and simplifying gives for $-\pi/2 \le \theta \le +\pi/2$

$$2\theta \cos \theta - \sin \theta = \sum_{n=2}^{\infty} \frac{(-1)^n \sin(2n-1)\theta}{n(n-1)} \qquad (C.26)$$

By use of this, the main equations in the series, (A.33) through (A.47) become

$$\Phi_s' = -\frac{\Gamma_h \theta}{2\pi} - \frac{\gamma c}{4\pi} \left[\theta \cos \theta + \left(1 - \ln \frac{16D}{c} \right) \sin \theta \right] \qquad (C.27)$$

and

$$w_{F_s}' = -\frac{\Gamma_h}{2\pi} + \frac{\gamma c}{4\pi} \left[\left(\ln \frac{16D}{c} - 2 \right) \cos \theta + \theta \sin \theta \right] \qquad (C.28)$$

when $-\pi/2 < \theta < +\pi/2$, and when $\pi/2 \le \theta \le 3\pi/2$

$$\Phi_s' = -\frac{\Gamma_h \theta}{2\pi} - \frac{\gamma c}{4\pi} \left[(\theta - \pi) \cos \theta + \left(1 - \frac{16D}{c} \right) \sin \theta \right] \qquad (C.29)$$

and

$$w_{F_s}' = -\frac{\Gamma_h}{2\pi} + \frac{\gamma c}{4\pi} \left[\ln \frac{16D}{c} - 2 + (\theta - \pi) \sin \theta \right] \qquad (C.30)$$

We also find

$$w_{F_t}' = -\frac{\Gamma_h}{2\pi} + \frac{\gamma c}{4\pi} \left(\ln \frac{16D}{c} - 2 \right) \qquad (C.31)$$

$$u_{\gamma_t} = \frac{\gamma}{2\pi} \left(\frac{\pi}{2} + \frac{c}{2D} \ln \frac{c}{8D} \right) \qquad (C.32)$$

$$v_{\gamma_t} = \frac{\gamma}{2\pi} \left(2 + \ln \frac{c}{8D} \right) \qquad (C.33)$$

$$\frac{\Gamma_h}{2\pi} = \frac{\gamma c}{4\pi} \left(\ln \frac{16D}{c} - 2 \right) \qquad (C.34)$$

Finally Equation (A.50) for the bound vorticity distribution along the duct chord becomes (with the actuator disk at the duct mid-chord)

$$\gamma_h = \frac{\gamma}{\pi} \left[\left(\ln \frac{16D}{c} - 2 \right) \tan \frac{\theta}{2} - \theta \right]$$

$$\text{for} \quad -\frac{\pi}{2} \leq \theta \leq +\frac{\pi}{2}$$

and   (C.35)

$$\gamma_h = \frac{\gamma}{\pi} \left[\left(\ln \frac{16D}{c} - 2 \right) \tan \frac{\theta}{2} + \pi - \theta \right]$$

$$\text{for} \quad \frac{\pi}{2} \leq \theta \leq \frac{3\pi}{2}$$

It can be seen from Equations (A.50), (C.16), and (C.35) for the three alternate locations of the actuator disk that the net vorticity distribution $\gamma + \gamma_h$ is invariant with disk location. That is, as the disk moves forward in the duct, its trailing vorticity γ is subtracted from γ_h so that the sum $\gamma + \gamma_h$ is invariant. Thus, it becomes evident that with the present flow model the flow pattern (and net duct reaction) is independent of the actuator-disk location for all flight conditions (not only hovering) so long as the disk is located within the duct. The static pressure rise through the actuator disk merely causes hoop tension in the duct downstream of the disk and does not directly affect the resultant force on the duct in the present analysis since its diameter is constant. For diverging ducts this pressure rise does contribute directly to duct thrust, however.

APPENDIX D

INVESTIGATION OF AVERAGING PROCESSES

Two averaging processes have been used in Reference 1 and in Appendix A herein to obtain the axial velocity distribution on the duct surface $(\bar{w}_i = \bar{w}_{h_i} + \bar{w}_{\alpha_i} + \bar{w}_{q_i})$ which is self-induced by the bound vorticity distribution on the duct $(\gamma_h + \gamma_\alpha + \gamma_q)$. Specifically: (1) the bound vorticity (γ) was first averaged over the chord length to give $\bar{\gamma}$ and (2) the surface velocity distribution induced by $\bar{\gamma}$ was averaged over the chord length to give $\bar{w}_i$.[1]

To assess the inaccuracy which is introduced into the final results of the analysis by these approximations, we shall use the actual chordwise distribution of bound vorticity γ to calculate the actual value of the self-induced surface velocity w_i at the duct.

D.1. HOVERING COMPONENT, w_{h_i}

The bound vorticity on the duct during hovering (or axial) flight is (Eq. (A.50))

$$\gamma_h = \frac{\gamma}{\pi}\left[\left(\ln \frac{16D}{c} - 2\right)\tan \frac{\theta'}{2} + \pi - \theta'\right] \tag{D.1}$$

We shall now find w_{h_i} the velocity induced by γ_h at three points along the chord and compare these three values with the average value $\bar{w}_{h_i}$ which was used in Section 3.

---

[1]Only the axial velocity component was considered because the radial component induced by a vortex ring for small c/D is nearly the same as that induced by a straight line filament $(D = \infty)$ Hence the radial component of the self-induced velocity is zero.
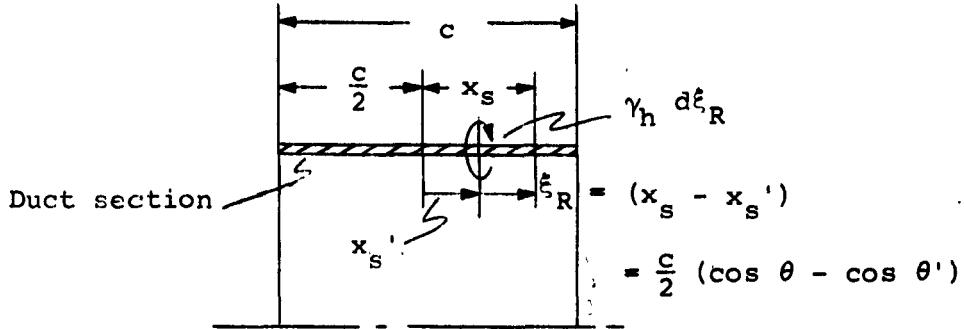
Sketch D.1.- Duct nomenclature.

From Equation A.48 (with $\xi_R = c/2\ (\cos\theta - \cos\theta')$ from Sketch D.1) we find that each elementary vortex ring $\gamma_h\ d\xi_R$ induces at x_s the axial velocity component

$$du_{h_s} = \frac{\gamma_h\ d\xi_R}{2\pi D}\left[\ln\left|\frac{8D}{c(\cos\theta - \cos\theta')}\right| - 1\right] \tag{D.2}$$

The total induced axial velocity at x_s is therefore obtained by integration over the duct. That is,

$$w_{h_i} = \frac{\gamma}{2\pi^2 D}\int_{-\left(\frac{c}{2} - x_s\right)}^{\frac{c}{2} + x_s}\left[\left(\ln\frac{16D}{c} - 2\right)\tan\frac{\theta'}{2} + \pi - \theta'\right]\left(\ln\frac{8D}{c} - 1\right.$$

$$\left. - \ln\left|\cos\theta - \cos\theta'\right|\right)d\xi_R \tag{D.3}$$

$$w_{h_i} = \frac{\gamma c}{4\pi^2 D}\int_0^{\pi}\left[\left(\ln\frac{16D}{c} - 2\right)\left(1 - \cos\theta'\right) + \pi\sin\theta'\right.$$

$$\left. - \theta'\sin\theta'\right]\left(\ln\frac{8D}{c} - 1 - \ln\left|\cos\theta - \cos\theta'\right|\right)d\theta' \tag{D.4}$$

Evaluating this expression at three locations we obtain:

at <u>midchord</u> $(2x_s/c = \cos\theta = 0)$

$$w_{h_i} = \frac{\gamma c}{4\pi D}\left[\left(\ln\frac{16D}{c}-1\right)\left(\ln\frac{8D}{c}-1\right)+\ln 2\left(\ln\frac{16D}{c}-2\right)+1\right]$$

(D.5)

at the <u>trailing edge</u> $(2x_s/c = \cos\theta = 1)$

$$w_{h_i} = \frac{\gamma c}{4\pi D}\left[\left(\ln\frac{16D}{c}-1\right)\left(\ln\frac{8D}{c}-1\right)+\left(\ln\frac{16D}{c}-2\right)\left(\ln 2-1\right)+\ln 2\right]$$

(D.6)

and at the <u>leading edge</u> $(2x_s/c = \cos\theta = -1)$

$$w_{h_i} = \frac{\gamma c}{4\pi D}\left[\left(\ln\frac{16D}{c}-1\right)\left(\ln\frac{8D}{c}-1\right)+\left(\ln\frac{16D}{c}-2\right)\left(\ln 2+1\right)\right.$$
$$\left.+2-3\ln 2\right]$$

(D.7)

Now from Equation (A.53), we have for the averaged value

$$\bar{w}_{h_i} = \frac{\gamma c}{4\pi D}\left[\left(\ln\frac{16D}{c}-1\right)\left(\ln\frac{8D}{c}-1\right)+\left(\ln\frac{16D}{c}-1\right)\left(\frac{3}{2}-\ln 2\right)\right]$$

(D.8)

Note that the first term in the bracket of Equations D.5 through D.8 is identical, and for very small values of c/D, the remainder of the bracket is negligible. However, the actual value of the remainder can be expressed in the form

$$A\left(\ln\frac{16D}{c}-1\right)+B$$

(D.9)

in each case with the value of A and B tabulated as follows.

Chordwise location	A	B
Leading edge	ln 2 + 1 = 1.69	1 - 4 ln 2 = -1.77
Midchord	ln 2 = 0.69	1 - ln 2 = 0.31
Trailing edge	ln 2 - 1 = -0.31	1
Averaged value used	3/2 - ln 2 = 0.81	0

Evaluation of Equations (D.5) through (D.8) for two values of c/D gives the values for $4\pi D \ w_{h_i}/c\gamma$ tabulated below

Chordwise location	c = 0.2D	c = 0.1D
Leading edge	13.09	18.92
Midchord	11.87	16.92
Trailing edge	9.08	13.54
Averaged value used	11.86	17.09

Thus, the averaging process introduces an error in the local value of w_{h_i} of about 30 percent for c = 0.2D.

D.2 ANGLE-OF-ATTACK COMPONENT, w_{α_i}

From Equation (A.65), we have for the bound vorticity on the duct induced by the free stream at angle of attack α_o.

$$\gamma_\alpha = w_\alpha(\theta') - w_\alpha(2\pi - \theta') = \frac{2\Gamma_\alpha}{\pi c} \tan \frac{\theta'}{2} = \frac{d\Gamma_\alpha}{d\ell_R} \qquad (D.10)$$

Now substituting for $d\Gamma_\alpha$ and using $\xi_R = c/2\ (\cos\theta - \cos\theta')$ in Equation (A.73) we obtain the total induced axial velocity at x_s

$$w_{\alpha_i} = -\frac{\Gamma_\alpha}{2\pi^2 D}\int_0^\pi (1 - \cos\theta')\left(3 - \ln\frac{8D}{c} + \ln\left|\cos\theta - \cos\theta'\right|\right)d\theta'$$

(D.11)

Evaluation of this integral gives:

$$\frac{2\pi D}{\Gamma_\alpha} w_{\alpha_i} = \ln\frac{16D}{c} - G_1$$

(D.12)

where $G_1 = 2,3,4$ at the duct leading edge, midchord, and trailing edge, respectively.

Also from Equation (A.77), we can write the averaged value of w_{α_i} as

$$\frac{2\pi D}{\Gamma_\alpha}\bar{w}_{\alpha_i} = \ln\frac{16D}{c} - \frac{3}{2} - \ln 4 = \ln\frac{16D}{c} - 2.89$$

(D.13)

This value is nearly equal to the value at midchord. The following values of $(2\pi D/\Gamma_\alpha)w_{\alpha_i}$ are obtained from Equations (D.12) and (D.13) for two values of c/D.

Chordwise location	c = 0.2D	c = 0.1D
Leading edge	2.39	3.07
Midchord	1.39	2.07
Trailing edge	0.39	1.07
Averaged value used	1.50	2.18

It can be seen that the actual values depart considerably from the averaged value which was used.

D.3. PITCHING COMPONENT, w_{q_i}

The bound vorticity on the duct γ_q induced by the pitching motion q (from Eqs. (A.88) and (A.94)) is

$$\gamma_q = \gamma_{q_1} + \gamma_{q_3} = qc \cos \phi \left(\sin \theta' - \frac{\pi c/4D}{1 + \frac{\pi c}{2D}} \tan \frac{\theta'}{2} \right) \qquad (D.14)$$

Using Equation (A.73) (with $d\Gamma = \gamma_q d\xi_R$ and $\xi_R = c/2 \, (\cos \theta - \cos \theta')$) we obtain the total induced axial velocity at x_s

$$w_{q_i} = \frac{qc^2}{4\pi D} \cos \phi \int_0^\pi \left[\sin^2\theta' - \frac{\pi c/4D}{1 + \frac{\pi c}{2D}} (1 - \cos \theta') \right] \left(\ln \frac{8D}{c} - 1 \right.$$

$$\left. - \ln \left| \cos \theta - \cos \theta' \right| \right) \partial\theta' \qquad (D.15)$$

Evaluation of this integral gives:

at <u>midchord</u> $(2x_s/c = \cos \theta = 0)$

$$w_{q_i} = \frac{qc^2}{8D} \left[\left(\ln \frac{8D}{c} - 3 \right) + \ln 2 + \frac{1}{2} - \frac{\pi c/2D}{1 + \frac{\pi c}{2D}} \left(\ln \frac{16D}{c} - 3 \right) \right] \cos \phi$$

$$(D.16)$$

at the <u>trailing edge</u> $(2x_s/c = \cos \phi = 1)$

$$w_{q_i} = \frac{qc^2}{8D} \left[\left(\ln \frac{8D}{c} - 3 \right) + \ln 2 - \frac{1}{2} - \frac{\pi c/2D}{1 + \frac{\pi c}{2D}} \left(\ln \frac{16D}{c} - 4 \right) \right] \cos \phi$$

$$(D.17)$$

and at the <u>leading edge</u> $(2x_s/c = \cos \theta = -1)$

$$w_{q_i} = \frac{qc^2}{8D} \left(\ln \frac{8D}{c} - 3 \right) + \ln 2 - \frac{1}{2} - \frac{\pi c/2D}{1 + \frac{\pi c}{2D}} \left(\ln \frac{16D}{c} - 2 \right) \right] \cos \phi$$

$$(D.18)$$

Now from Equation (A.95), we can write for the averaged value

$$\bar{w}_{q_i} = \frac{qc^2}{8D} \frac{1}{1 + \frac{\pi c}{2D}} \left[\left(\ln \frac{8D}{c} - 3 \right) + \frac{3}{2} - \ln 2 \right] \cos \phi \qquad (D.19)$$

By use of

$$\left(\frac{8D}{qc^2 \cos \phi} \right) w_{q_i} \equiv G_2 \qquad (D.20)$$

evaluation of Equations (D.16) through (D.20) for two values of c/D gives the following values of G_2

Chordwise location	c = 0.2D	c = 0.1D
Leading edge	0.31	1.16
Midchord	1.55	2.30
Trailing edge	0.79	1.44
Averaged value used	1.14	1.90

It is found that the components w_i vary as much as 100 percent (but not by an order of magnitude) from the average values $\bar{w}_i$ previously obtained. The self-induced velocity components generally have only small effects upon most of the final stability

derivatives. All of them affect only higher-order terms in c/D for the pitching derivatives. The α coefficients $M_{D(P)}$ and $T_{D(P)}$ are unaffected because neither w_{h_i} nor w_{α_i} affect the leading-edge singularity. The error, from averaging w_{h_i} and w_{α_i}, in Equation (B.14) for N_D may be appreciable, however. Inasmuch as the derivative $\left(C_{N_\alpha}\right)_{D(P)}$ is found to dominate the dynamic stability of a torpedo-like configuration, this averaging error would seem to warrant further attention.

APPENDIX E

HULL-BOUNDARY-LAYER CALCULATIONS

In order to determine the center of pressure of the hull at angle of attack (a/L in Section 3.5.1 and Fig. 5), the volume of the hull combined with the displacement thickness of its boundary layer is required, as seen from Equation (76). This volume will now be determined by using the "effective" hull radius. Thus, we let

$$r_H^* = r_H + \delta^* \qquad (E.1)$$

where r_H is the actual hull radius. Now, for the assumed flat-plate turbulent boundary layer, we have for the displacement thickness δ^*

$$\delta^* = 0.37 \left(\text{Re} \right)^{-1/5} \left(\frac{L}{2} - x_H \right) \qquad (E.2)$$

and

$$\frac{\delta^*}{r_m} = \frac{\delta_L^*}{r_m} \left(\frac{1}{2} - \frac{x_H}{L} \right)^{4/5} \qquad (E.3)$$

Thus, we find from Equations (E.1), (E.2), and (78) that

$$\left(\frac{r_H^*}{r_m} \right)^2 = \left[1 - \left(2 \frac{x_H}{L} \right)^2 \right]^2 + 2 \frac{\delta_L^*}{r_m} \left(\frac{1 - 2 \frac{x_H}{L}}{2} \right)^{4/5} \left[1 - \left(2 \frac{x_H}{L} \right)^2 \right]$$

$$+ \left(\frac{\delta_L^*}{r_m} \right)^2 \left(\frac{1 - 2 \frac{x_H}{L}}{2} \right)^{8/5} \qquad (E.4)$$

E-2

The volume of the hull and boundary layer is then given by

$$\text{Vol*} = \pi r_m^2 \frac{L}{2} \int_{-1}^{+1} \left(\frac{r_H^*}{r_m}\right)^2 d\frac{2x_H}{L} \qquad (E.5)$$

Thus, letting $\xi \equiv 2(x_H/L)$, we obtain

$$\frac{2\text{Vol*}}{\pi r_m L} = \int_{-1}^{+1} \left(1 - \xi^2\right)^2 d\xi + 4\frac{\delta_L^*}{r_m} \int_{-1}^{+1} (1 + \xi)\left(\frac{1-\xi}{2}\right)^{9/5} d\xi$$

$$+ \left(\frac{\delta_L^*}{r_m}\right)^2 \int_{-1}^{+1} \left(\frac{1-\xi}{2}\right)^{8/5} d\xi \qquad (E.6)$$

$$\frac{\text{Vol*}}{\pi r_m^2 L} = \frac{8}{15} + \left(\frac{40}{14} - \frac{40}{19}\right)\frac{\delta_L^*}{r_m} + \frac{5}{13}\left(\frac{\delta_L^*}{r_m}\right)^2 \qquad (E.7)$$

for $\text{Re}_L = 4\times10^7$ we have from Equation (86)

$$\frac{\delta_L^*}{r_m} = \frac{0.111}{0.5} = 0.223 \qquad (E.8)$$

$$\frac{\text{Vol*}}{\pi r_m^2 L} = 0.523 + 0.167 + 0.019 = 0.709 \qquad (E.9)$$

In addition to the volume the following integral is needed in Section 3.5.1 for use in Equation (95).

$$4C_{22}{}^* \equiv 4 \int_{-\frac{1}{2}}^{+\frac{1}{2}} \left(\frac{r_H{}^*}{r_m}\right)^2 \frac{x_H}{L} \, d\, \frac{x_H}{L} \qquad (E.10)$$

$$4C_{22}{}^* = \int_{-1}^{+1} \left(1 - \xi^2\right)^2 \xi \, d\xi + 4\,\frac{\delta_L{}^*}{r_m} \int_{-1}^{+1} (1 - \xi)\left(\frac{1-\xi}{2}\right)^{9/5} \xi \, d\xi$$

$$+ \left(\frac{\delta_L{}^*}{r_m}\right)^2 \int_{-1}^{+1} \left(\frac{1-\xi}{2}\right)^{8/5} \xi \, d\xi \qquad (E.11)$$

$$4C_{22}{}^* = 0 - \frac{100}{19 \times 42}\,\frac{\delta_L{}^*}{r_m} - \frac{40}{9 \times 13}\left(\frac{\delta_L{}^*}{r_m}\right)^2 \qquad (E.12)$$

$$4C_{22}{}^* = -\,0.576 \quad \text{for} \quad \frac{\delta_L{}^*}{r_m} = 0.223 \qquad (E.13)$$

The radius of gyration of the hull K_y will now be determined for use in Section 3.5.1. The mass of the hull is given by

$$m_H = \rho \ \text{Vol} = \frac{8}{15}\,\pi r_m{}^2 L \rho \qquad (E.14)$$

and about the hull centroid, at $x_H = 0$, we have

$$m_H K_y{}'^2 = 2\rho \pi r_m{}^2 L^3 \int_0^{1/2} \frac{r_H{}^2}{r_m{}^2}\left(\frac{x_H}{L}\right)^2 d\,\frac{x_H}{L} \qquad (E.15)$$

$$m_H K_y{}'^2 = \frac{\rho}{4}\,\pi r_m{}^2 L^3 \int_0^1 \left[1 - \left(2\,\frac{x_H}{L}\right)^2\right]^2 \left(\frac{2x_H}{L}\right)^2 d\,\frac{2x_H}{L} \qquad (E.16)$$

$$m_H K_y'^2 = \frac{\rho}{4} \pi r_m^2 L^3 \int_0^1 \left(\xi^2 - 2\xi^4 + \xi^6\right) d\xi \qquad (E.17)$$

$$m_H K_y'^2 = \frac{\rho}{4} \pi r_m^2 L^3 \left(\frac{1}{3} - \frac{2}{5} + \frac{1}{7}\right) \qquad (E.18)$$

$$m_H K_y'^2 = \frac{\rho}{4} \pi r_m^2 L^3 \left(\frac{8}{105}\right) \qquad (E.19)$$

$$K_y'^2 = \frac{L^2}{28} \qquad (E.20)$$

Now, about the hull center of gravity, at $x_H = L/10$, we find for the radius of gyration

$$K_y''^2 = \frac{L^2}{28} + \frac{L^2}{100} = 0.0457\ L^2 \qquad (E.21)$$

$$K_y'' = 0.214\ L = 2.14\ ft \qquad (E.22)$$

TABLE I.- STATIC STABILITY DERIVATIVES OF A PROPELLER.

$$\sigma \frac{V_o}{\omega D} = 1 \ , \qquad C_{T_{P(D)}} = 2.17 \ , \qquad \gamma = 0.78 \ V_o$$

β (deg)	$\left(C_{N_\alpha}\right)_P$ Dual propeller (refined)	(approx.)	$\left(C_{n^*_\alpha}\right)_P$ Single propeller (refined)
10	0.051	0.142	0.401
20	.105	.279	.402
30	.158	.408	.398

TABLE II.- STABILITY DERIVATIVES OF A SINGLE PITCHING PROPELLER.

$$\sigma \frac{V_o}{\omega D} = 1 \ , \qquad C_{T_{P(D)}} = 2.17 \ , \qquad \gamma = 0.78 \ V_o$$

β (deg)	$-\left(C_{Y_q}\right)_P$ (refined)	(approx.)	$-\left(C_{m_q}\right)_P$ (refined)	(approx.)
10	0.155	0.32	0.17	0.28
20	.128	.31	.17	.28
30	.122	.29	.17	.28

TABLE III.- COMPARISON OF DUCT AND PROPELLER STABILITY
DERIVATIVES DUE TO ANGLE OF ATTACK.

Stab. Deriv.	D(P)	P(D)
C_{N_α}	1.95	< 0.15
C_{m_α}	.072	.130
$C_{n^*_\alpha}$	0	< .4
$C_{m'_\alpha}$	-19.4	$\|\ \|$ < 1.5

TABLE IV.- COMPARISON OF DUCT AND PROPELLER STABILITY DERIVATIVES DUE TO PITCH.

Stab. Deriv.	D(P)	P(D)
C_{N_q}'	9.91	< 0.8 (due to α_o')
C_{Y_q}'	0	||< .15 (due to q)
C_{m_q}	.364	.065 (due to α_o') < .5 (due to q)
$C_{n_q}^*$	0	||< 2 (due to α_o')
C_{m_q}'	-98.7	||< 8

TABLE V.- STABILITY DERIVATIVES ABOUT HULL CENTROID (0.5L) FOR THE CONFIGURATION OF FIGURE 4.

Flight condition	Stability derivative	Hull H	Duct D(P)	Propeller P(D)
α	C_{N_α}	0.099	1.95	< 0.15
	C_{m_α}'	28.0	-19.4	| | < 1.5 $C_{n*_\alpha}' < C_{m_\alpha}'$
q	C_{N_q}'	.495	9.91	< .8 $-C_{Y_q}' < .15$
	C_{m_q}'	52.6	-98.7	< 8 $C_{n*_q}' << C_{m_\alpha}'$
α̇	$C_{N_{\dot\alpha}}$	14.2	.126	Small compared with duct
	$C_{m_{\dot\alpha}}'$	-57.6	-1.26	Small compared with duct
q + α̇	$C_{m_q}' + C_{m_{\dot\alpha}}'$	-5.0	-100.0	Small compared with duct

TABLE VI.- STABILITY DERIVATIVES ABOUT THE VEHICLE CENTER OF
GRAVITY (0.4L) FOR THE COMPLETE CONFIGURATION OF FIGURE 4.

Flight condition	Stability derivative	Hull H	Ducted propeller D(P)	Fin F	Total HDPF
α	C_{N_α}	0.099	1.95	0.86	2.91
	C_{m_α} "	27.8	-23.3	-10.3	-5.8
q	C_{N_q} "	.594	11.9	5.15	17.6
	C_{m_q} "	79.4	-141.8	-61.9	-124.3
$\dot{\alpha}$	$C_{N_{\dot{\alpha}}}$	14.2	.126	.038	14.4
	$C_{m_{\dot{\alpha}}}$ "	-86.0	-1.51	-.45	-88.0
$q + \dot{\alpha}$	$C_{m_q} + C_{m_{\dot{\alpha}}}$	-6.6	-143.3	-61.5	-212.3

TABLE VII.- COMPARISON OF PRESENT THEORY WITH EXPERIMENTAL
DATA BY GILL, REFERENCE 13, FOR AXIAL FLOW.

$\dfrac{V_j}{V_o}$	$C_{T_{P(D)}}$ exper.	$\dfrac{\gamma}{V_o}$	$\dfrac{T_{D(P)}}{T_{P(D)}}$ exper.	$\dfrac{T_{D(P)}}{T_{P(D)}} = \dfrac{0.78}{1+2(V_o/\gamma)}$ (pred.) Eq.(203)	η_p exper. Eq.(205)	$\eta_p = \dfrac{2}{(V_j/V_o)+1}$ (pred.) Eq.(206)
4.1	16	3.1	0.25	0.47	0.25	0.39
2.4	5.0	1.4	.12	.33	.44	.59
1.8	2.2	0.8	.16	.22	.51	.71

TABLE VIII.- COMPARISON OF PRESENT THEORY WITH EXPERIMENTAL DATA BY HORN, REFERENCE 17, FOR AXIAL FLOW.

$\dfrac{V_o}{nD}$	$C_{T_{P(D)}}$ exper.	$\dfrac{\gamma}{V_o}$	$\dfrac{T_{D(P)}}{T_{P(D)}}$ exper.	$\dfrac{T_{D(P)}}{T_{P(D)}} = \dfrac{0.7}{1+2(V_o/\gamma)}$ (pred.) Eq.(203)	η_P exper.	$\eta_P = \dfrac{2}{(V_j/V_o)+1}$ (pred.) Eq.(206)
0			0.46			
0.25	1.14	0.46	.32	0.125	0.31	0.81
.50	.22	.11	.18	.036	.51	.95
.75	.068	.034	0	.012	.59	.97
1.0	.018	.009	-.57	.006	.27	1.0

TABLE IX.- COMPARISON OF PRESENT THEORY WITH EXPERIMENTAL DATA BY ALLEN, REFERENCE 21, FOR AXIAL FLOW.

$\beta°$	$\dfrac{V_o}{nD}$	$C_{T_{P(D)}}$ exper.	$\dfrac{\gamma}{V_o}$	$\dfrac{T_{D(P)}}{T_{P(D)}}$ exper.	$\dfrac{T_{D(P)}}{T_{P(D)}} \simeq \dfrac{0.7}{1+2(V_o/\gamma)}$ (pred.) Eq.(203)	η_P exper.	$\eta_P = \dfrac{2}{(V_j/V_o)+1}$ (pred.) Eq.(206)
20	0.40	0.92	0.38	0.087	0.11	0.70	0.84
25	.60	.40	.19	.089	.061	.77	.91

TABLE X.– COMPARISON OF PRESENT THEORY WITH EXPERIMENTAL DATA BY KRUGER, REFERENCE 19, FOR AXIAL FLOW.

$\beta°$	$\dfrac{V_o}{\omega R}$	$C_{T_{P(D)}}$ exper.	$\dfrac{\gamma}{V_o}$	$\dfrac{T_{D(P)}}{T_{P(D)}}$ exper.	$\dfrac{T_{D(P)}}{T_{P(D)}} \simeq \dfrac{0.75}{1+2(V_o/\gamma)}$ (pred.) Eq.(203)	η_P exper.	$\eta_P = \dfrac{2}{(V_j/V_o)+1}$ (pred.) Eq.(206)
15	0.14	3	3	0.3	0.45	0.42	0.50
25	.19	2	0.73	.5	.25	.43	.73
25	.26	1	.41	.6	.13	.50	.83
25	.32	0.5	.22	.6	.08	.56	.90
35	.48	.22	.10	.8	.04	.58	.95

### TABLE XI.– COMPARISON OF PRESENT THEORY WITH EXPERIMENTAL DATA BY GROSE, REFERENCE 14, FOR AXIAL FLOW.

$\beta°$	$\dfrac{V_o}{nD}$	$C_{T_{P(D)}}$ exper.	$\dfrac{\gamma}{V_o}$	$\dfrac{T_{D(P)}}{T_{P(D)}}$ exper.	$\dfrac{T_{D(P)}}{T_{P(D)}} \simeq \dfrac{0.70}{1+2(V_o/\gamma)}$ (pred.) Eq.(203)	η_P exper.	$\eta_P = \dfrac{2}{(V_j/V_o)+1}$ (pred.) Eq.(206)
22	0.72	0.64	0.28	0.044	0.084	0.77	0.88
22	.63	.97	.39	.086	.115	.70	.84
27	.72	1.09	.45	.095	.127	.70	.82

TABLE XII.- COMPARISON OF PRESENT THEORY WITH EXPERIMENTAL
DATA BY GROSE, REFERENCE 14, AT ANGLE OF ATTACK.

$\beta°$	$\dfrac{V_o}{nD}$	$C_{T_{P(D)}}$ exper.	$\dfrac{\gamma}{V_o}$	$\left(C_{L_\alpha}\right)_{D(P)}$ (per rad) exper.	$\left(C_{L_\alpha}\right)_{D(P)}$ (per rad) (pred.) Eq.(208)
22	0.85	0.25	0.12	3.58	3.60
32	1.3	.16	.08	3.56	3.54

TABLE XIII.- COMPARISON OF PRESENT THEORY WITH EXPERIMENTAL
DATA BY GILL, REFERENCE 13, AT ANGLE OF ATTACK.

α_o	$\dfrac{V_j}{V_o}$	$\beta°$	$\left(C_N\right)_{D(P)}$ exper.	pred. Eq.(209)	$T_{D(P)}/T_{P(D)}$ exper.	pred. Eq.(210)	$\left(C_m\right)_{D(P)}$ exper.	pred. Eq.(211)
50	3.40	18	1.76	2.02	0.11	0.56	0.42	2.52
50	1.80	9	.88	1.32	.20	.75	.23	1.13
80	3.25	15	1.12	2.12	.15	.82	.44	3.68
80	2.05	9	1.07	1.47	.10	1.12	.30	2.41
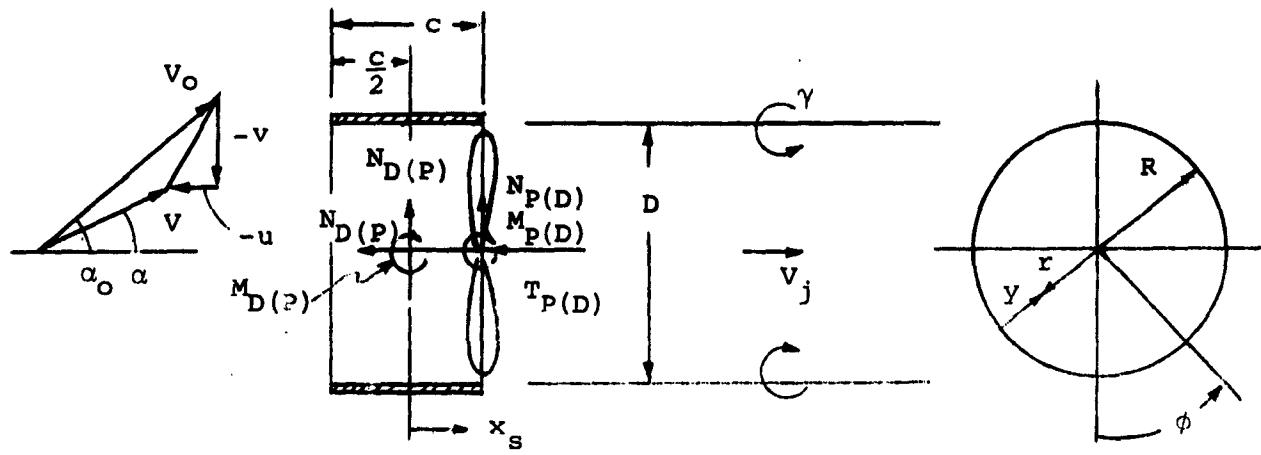
(a) Ducted actuator disk nomenclature.

$$z = \frac{c}{4} \left(\zeta + \frac{1}{\zeta}\right)$$

On inner surface $0 < \theta < \pi$

On outer surface $\pi < \theta < 2\pi$

$$x_s = c/2 \cos \theta$$

(b) ζ plane transformation.

Figure 1.- Mathematical representation of ducted propeller.
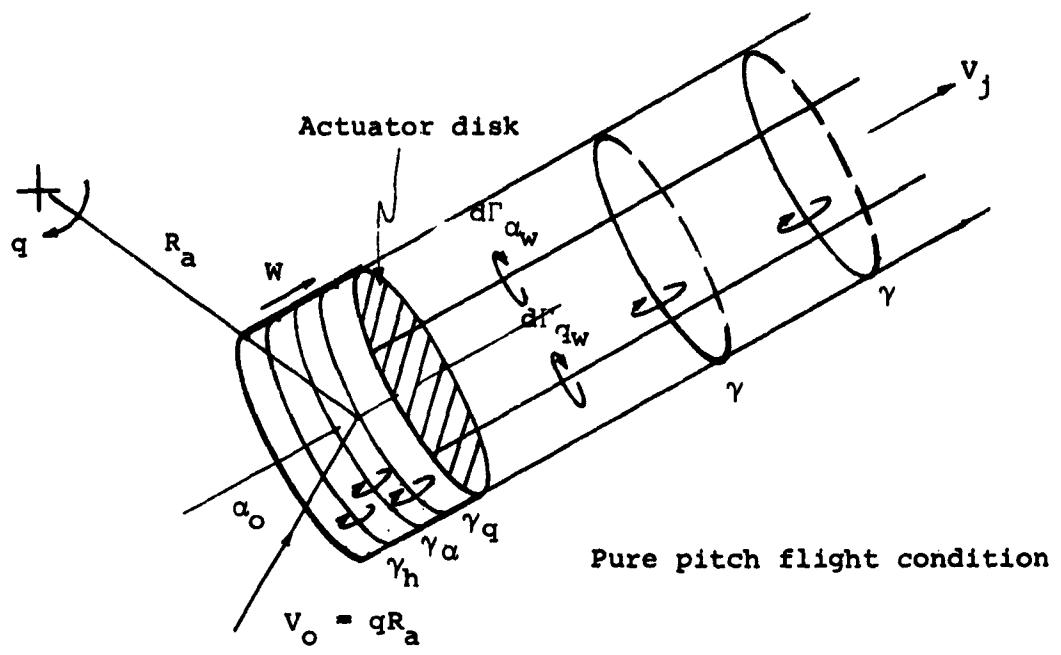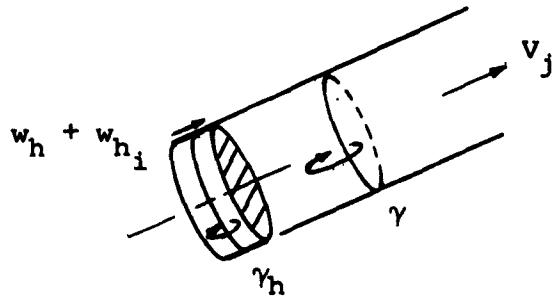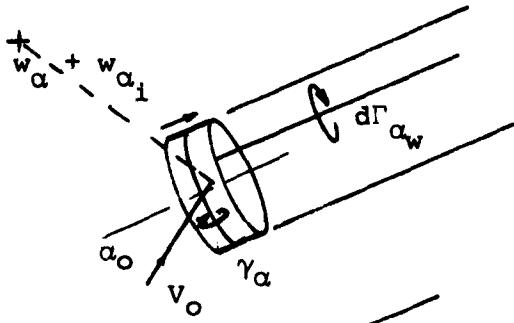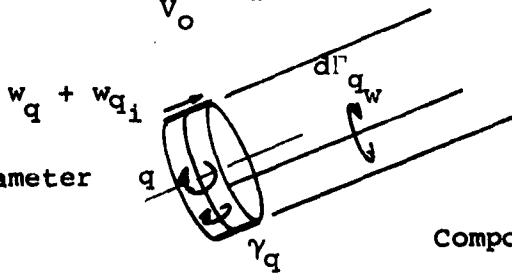
Figure 2.- Nomenclature for ducted actuator disk
in pure pitch flight.
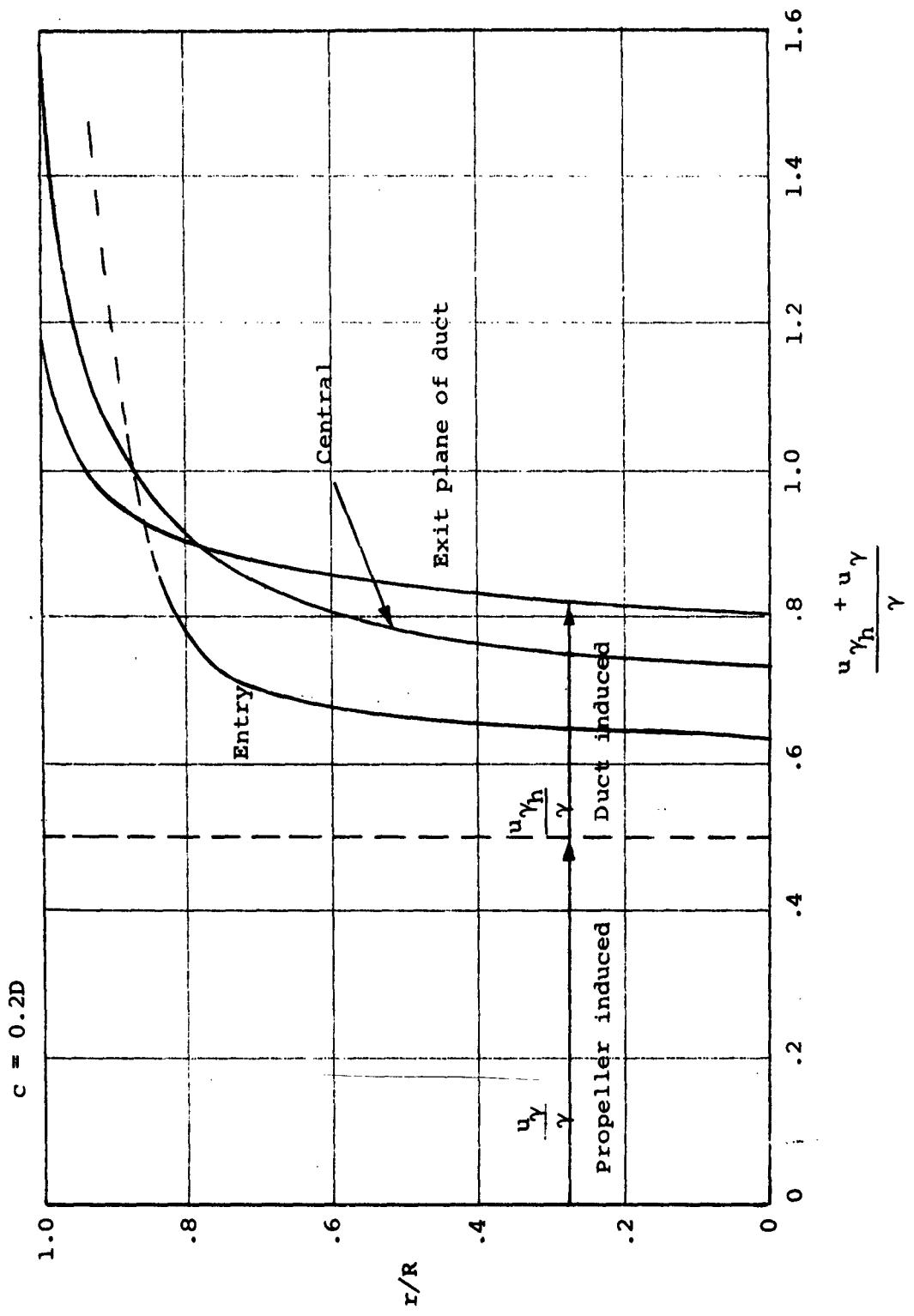
(a) Zero angle of attack (Eq. (42)).

Figure 3.- Induced velocity profiles at various locations of propeller in duct.

O Calculated value for c = 0.2D (Eq. (45))
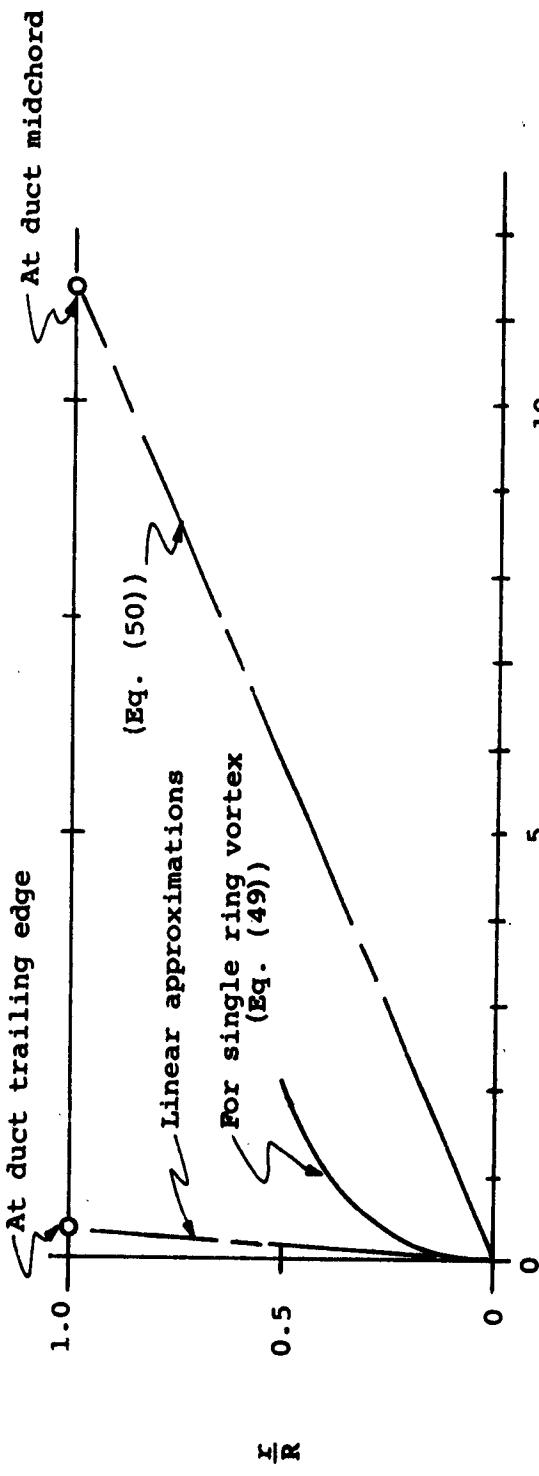
$$\frac{2\pi D}{\Gamma_\alpha} u_{\gamma_\alpha} = \frac{2D}{c \sin \alpha_o \cos \phi} \frac{u_{\gamma_\alpha}}{V_o}$$

(b) Additional velocity induced by duct at angle of attack.

Figure 3.- Concluded.

Assumed hull center of gravity at 0.4L
Hull centroid at 0.5L
Ducted propeller
Fins
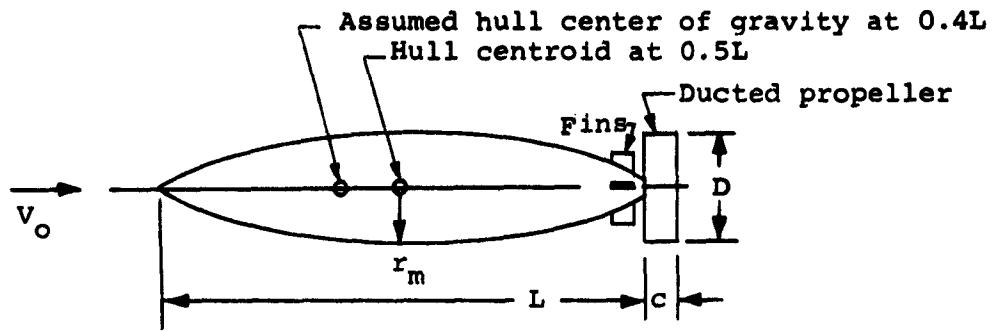
$V_o = 40$ ft./sec., $L = 10$ ft., $D = 2r_m = 1$ ft., $c = 0.2$ ft.

Figure 4.- Complete torpedo-like configuration.

$x_H/L = 1/2$ $x_H/L = -1/2$
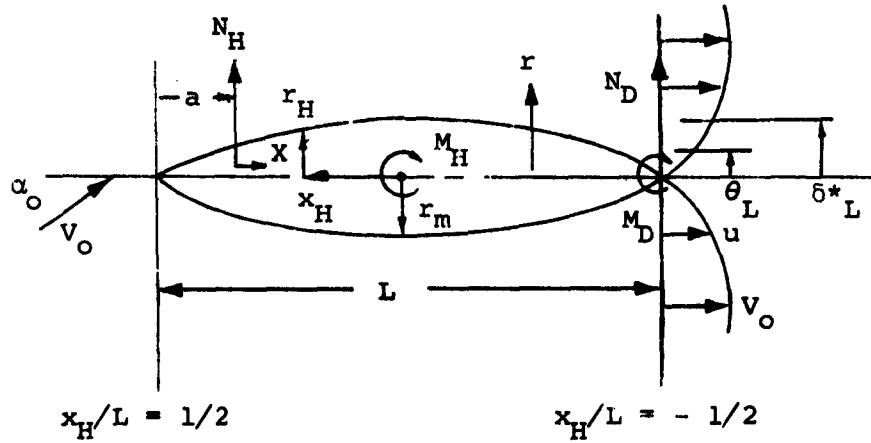
Figure 5.- Hull nomenclature.

Propeller swirl

Section j-j

Duct wake swirl

$V_o \sin(\alpha_o - \alpha_j)$
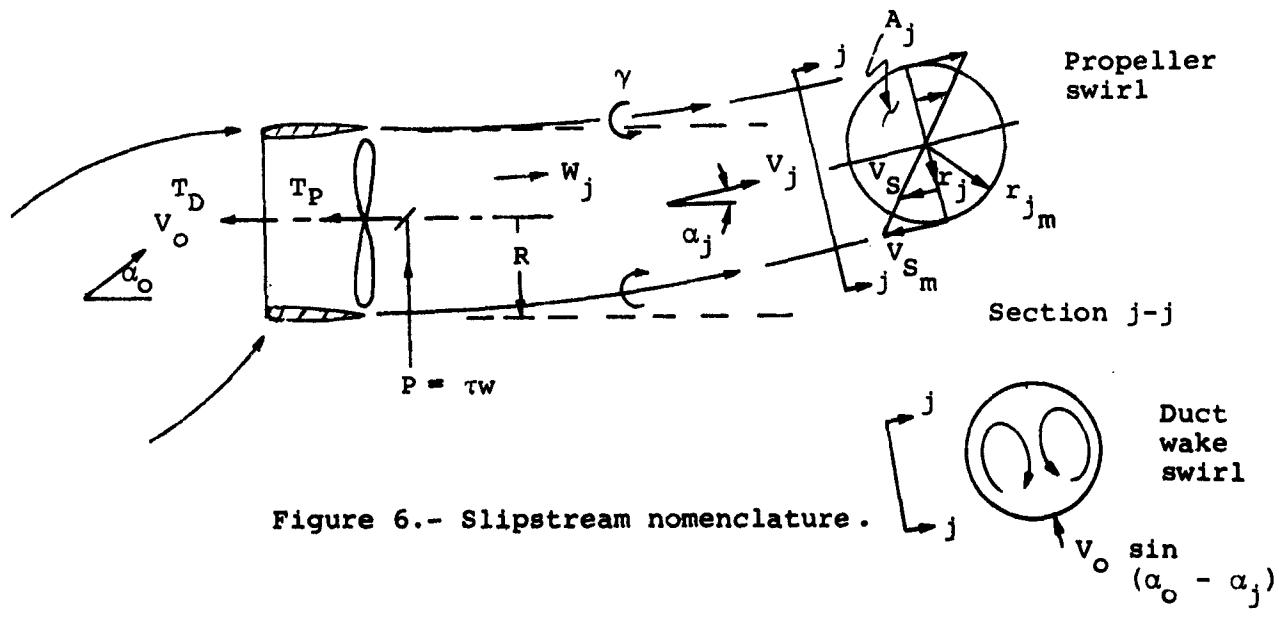
Figure 6.- Slipstream nomenclature.

Duct D_4P_3S

□ $\beta = 17°$ for max M_h

    = $18°$ for max η_h

Front prop plane

Rear prop plane

←3.6"→

1.5" (propeller spacing)

Duct D_2P_3S

△ $\beta = 18°$ for max M_h and η_h

←6"→

D/2 = 12"

1.5"

Duct D_1P_3S

○ $\beta = 15°$ for max M_h and η_h

←6"→

1.5"

Angles indicated are blade pitch setting β.

Asymptote

$\dfrac{T_{D(P)h}}{T_{P(D)h}}$ thrust ratio

c/D chord to diameter ratio
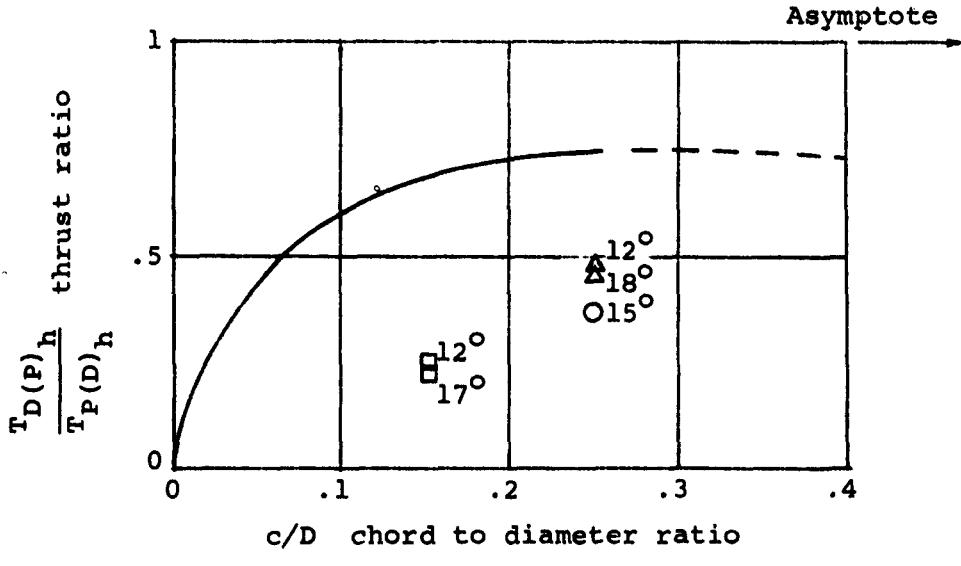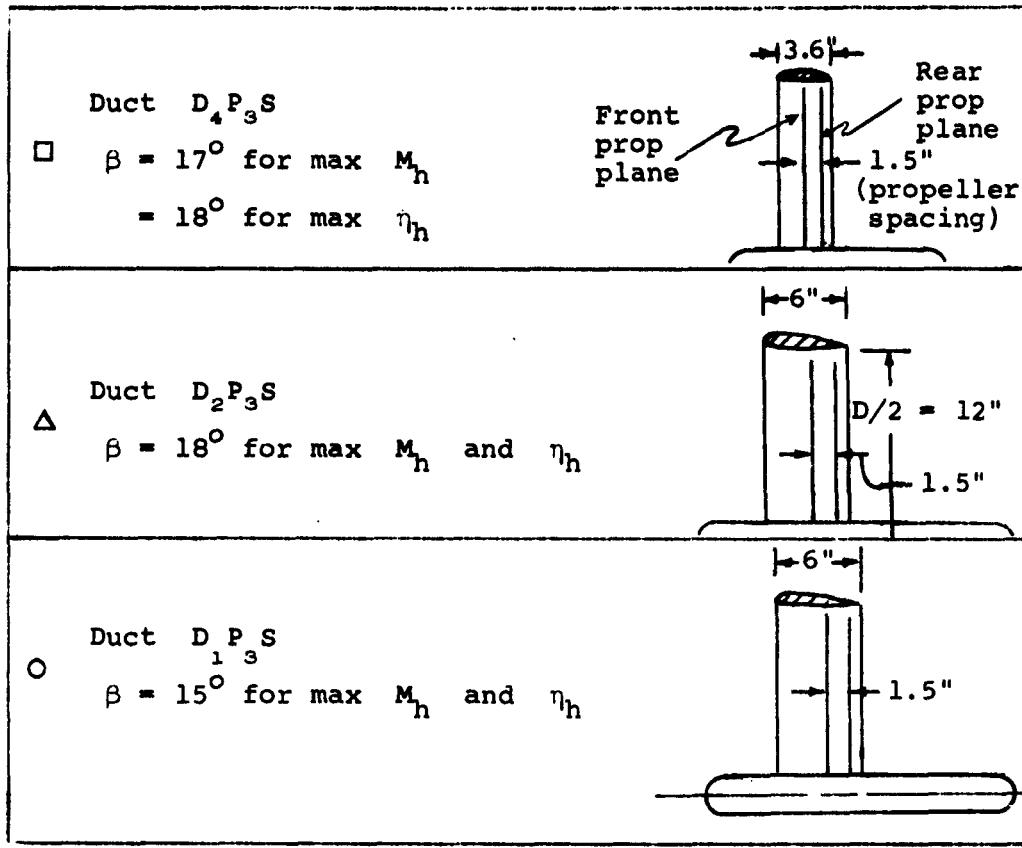
(a) Data by Gill, Reference 13.

Figure 7.- Comparison of theoretical and experimental thrust ratio in hovering flight.

Horn
Reference 17

Moser
Reference 18

$$0.33 \leq \frac{c}{D} \leq 0.89$$

Kruger
Reference 19
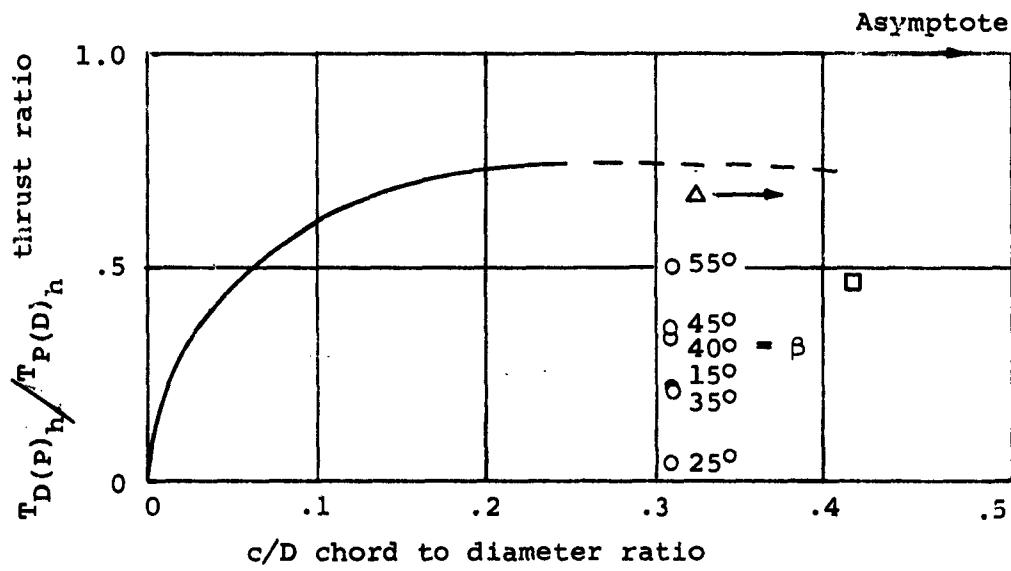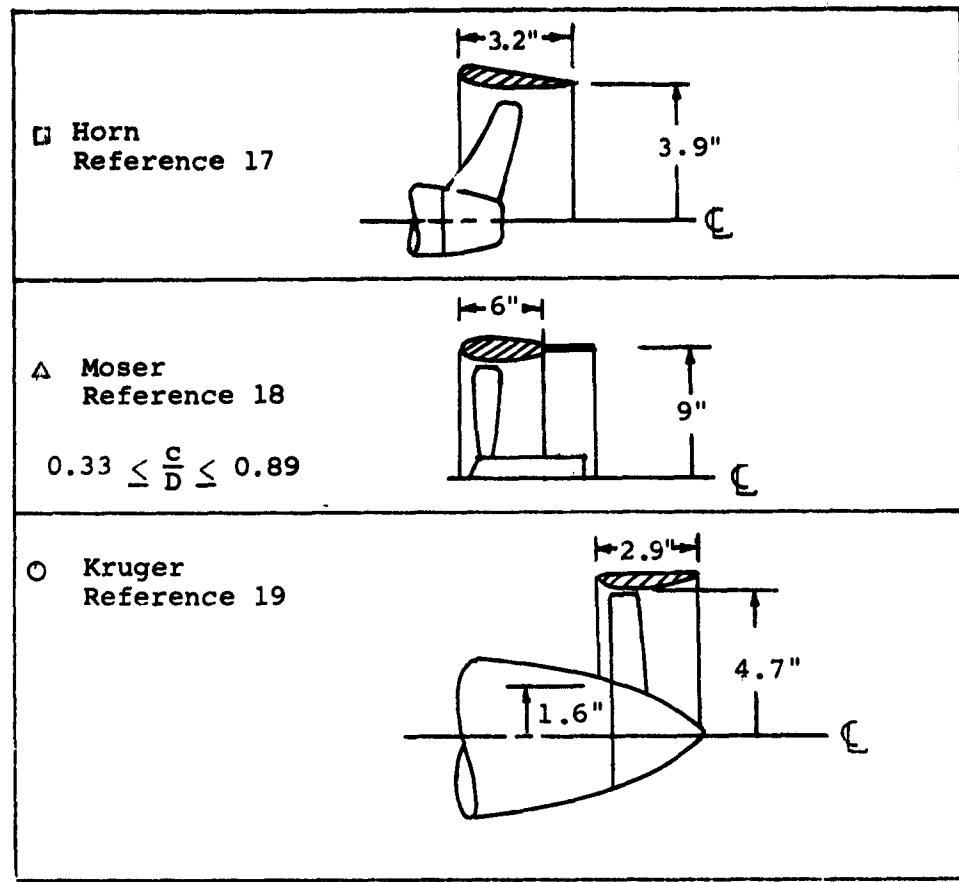
(b) Data by Horn, Moser, and Kruger.

Figure 7.- Continued.

□ Grose
   Reference 14

15"

15.7"

15"

∇

O Platt
  Reference 20

Long centerbody

32"

24"

∇

2.0

○45°
○35° = β
○40°

1.5

Asymptote

1.0

$T_{D(P)_h} / T_{P(D)_h}$ thrust ratio

.5

□ 15°
□ 35° = β
□ 10°

0

0   .2   .4   .6   .8

c/D chord to diameter ratio
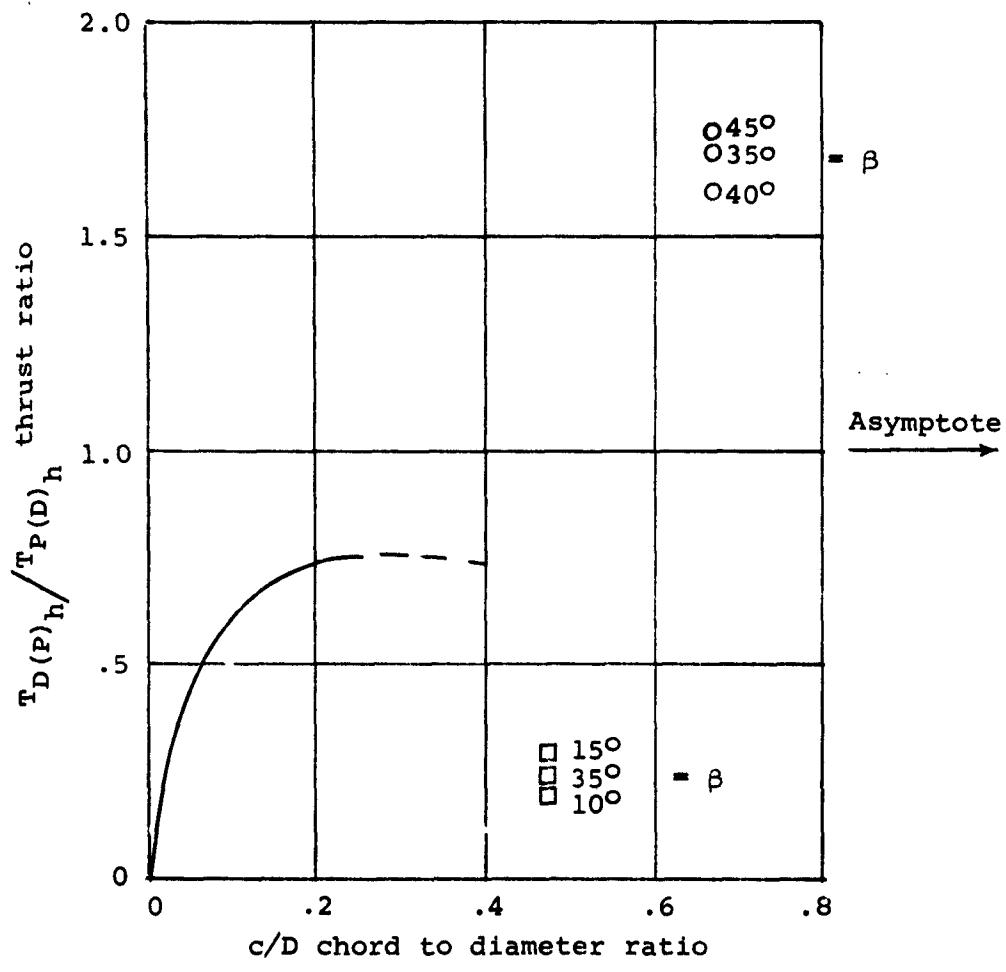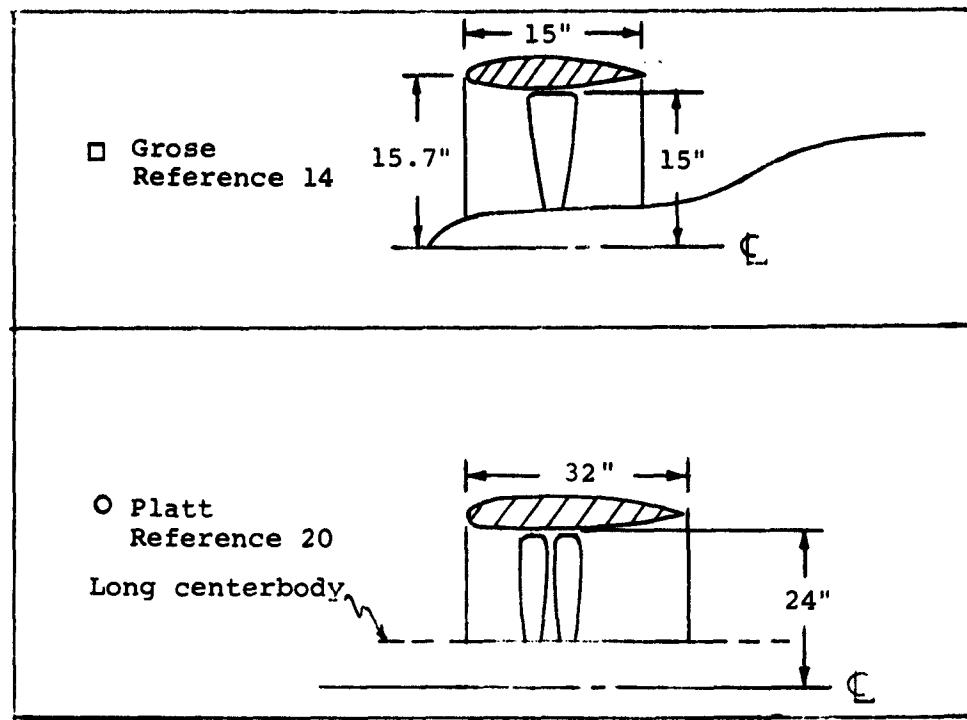
(c) Data by Grose and Platt.

Figure 7.- Concluded.
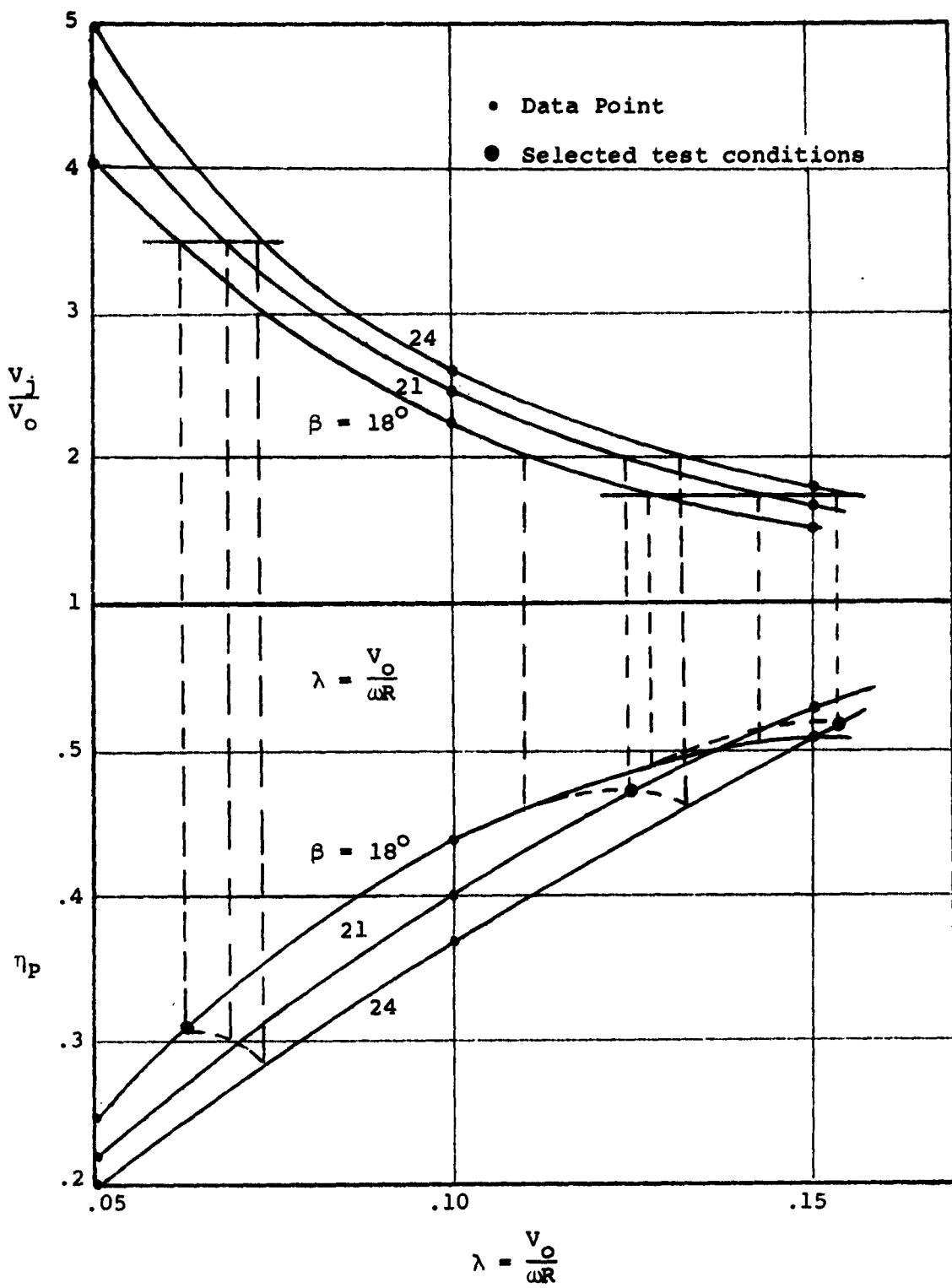
Figure 8.- Plots of data from Reference 13 for duct D_4P_3S at $\alpha_o = 0$.

Boundary-layer control
manifold (see DETAIL A)

Propellers

D = 24 in.

c = 0.2D = 4.8 in.

Duct

$\epsilon' = 0.1c = \frac{1}{2}$ in.

Duct
support

Wake velocity
rake

Motor housing

B.L.C. suction

Filler material

Steel
plate

$\epsilon = \frac{1}{2}$ in.

B.L.C. slot

Propeller spacing = $1\frac{1}{2}$ in.

DETAIL A
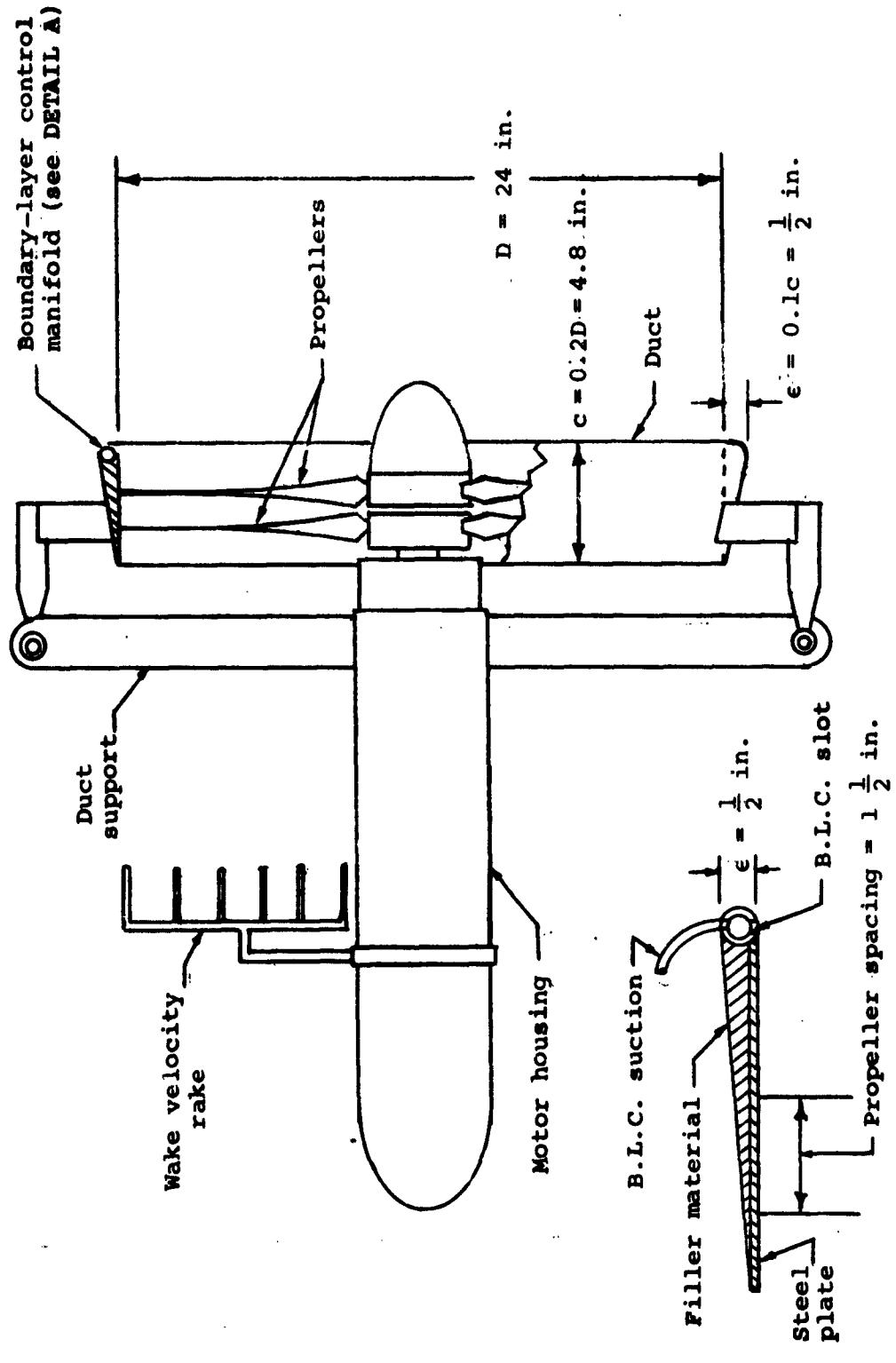
Figure 9.- Ducted-propeller configuration.

DISTRIBUTION LIST

NAVY

Chief, Bureau of Naval Weapons
Department of the Navy
Washington 25, D.C.
Attn: (Mail to Code DLI-3 for:)
      Code RRRE-4
      Code RAAD-3
      Code RUTO-32
      Code DLI-3   (2)

Commanding Officer and Director
David Taylor Model Basin
Carderock, Maryland
Attn: Hydromechanics Laboratory
      Aerodynamics Laboratory

Commander
Naval Missile Center
Point Mugu, California

Commander
Naval Ordnance Test Station
Inyokern, China Lake, California

Commander
Naval Ordnance Test Station
Pasadena Annex
Pasadena, California
Attn: Code P80
      Code P5006

Commander
Naval Ordnance Laboratory
White Oak, Silver Spring,
Maryland
Attn: Code H

Commanding Officer
Naval Underwater Ordnance Station
Newport, Rhode Island

Officer in Charge
Naval Aircraft Torpedo Unit
U.S. Naval Air Station
Quonset Point, Rhode Island
Attn: R. Crowell

Commanding Officer
Naval Torpedo Station
Keyport, Washington
Attn: J. Mason

Commander
Naval Weapons Laboratory
Dahlgren, Virginia
Attn: Technical Library

Chief of Naval Research
Department of the Navy
Washington 25, D.C.
Attn: Code 438
      Code 461
      Code 466

Chief, Bureau of Ships
Department of the Navy
Washington 25, D.C.
Attn: Code 421

AIR FORCE

Commander
Office of Aerospace Research
Washington 25, D.C.

Directorate of Aeromechanics
USAF Aeronautical Systems Division
Wright-Patterson Air Force Base,
Ohio

ARMY

Office of the Chief of Research
 and Development
Department of the Army
Washington 25, D.C.
Attn: Air Mobility Division

Commanding Officer
U.S. Army Transportation Research
 Command
Fort Eustis, Virginia

OTHER AGENCIES

Commander
Armed Services Technical Information
 Agency
Arlington Hall Station
Arlington 12, Virginia   (10)

National Aeronautics and Space
 Administration
1512 H Street N.W.
Washington 25, D.C.   (4)

EDUCATIONAL INSTITUTIONS

Alden Hydraulic Laboratory
Worcester Polytechnic Institute
Worcester 9, Massachusetts
Attn: L. J. Hooper

California Institute of Technology
Pasadena, California
Attn: Hydrodynamics Laboratory

Davidson Laboratory
Stevens Institute of Technology
711 Hudson Street
Hoboken, New Jersey
Attn: A. Suarez

Department of Aeronautical
 Engineering
Princeton University
Princeton, New Jersey
Attn: C. D. Perkins

Ordnance Research Laboratory
Pennsylvania State University
State College, Pennsylvania
Attn: G. F. Wislicenus

Massachusetts Institute of
 Technology
Department of Aeronautics and
 Astronautics (J. Bicknell)
Department of Naval Architecture
 and Marine Engineering
 (M. Abkowitz)
Cambridge 9, Massachusetts

INDUSTRY

Advanced Systems Engineering
Westinghouse Electric Corporation
Hendy Avenue
Sunnyvale, California
Attn: M. S. Macovsky

Aerojet General Corporation
6352 N. Irwindale Ave.
Azusa, California
Attn: C. A. Gongwer

Bell Aerosystems Company
Buffalo 5, New York
Attn: R. S. Postle

Ling-Temco-Vought Corporation
P.O. Box 1508
Dallas 22, Texas

Cornell Aeronautical Laboratory
4455 Genesee Street
Buffalo 21, New York
Attn: Dr. I. C. Statler

Douglas Aircraft Company, Inc.
Aircraft Division
3855 Lakewood Blvd.
Long Beach, California
Attn: Mr. A. M. O. Smith

Eastern Research Group
120 Wall Street
New York 5, New York

General Dynamics/Convair
P.O. Box 1950
San Diego 12, California
Attn: Chief of Hydrodynamics

General Dynamics
Electric Boat Division
Groton, Conn.

Goodyear Aircraft Corporation
Akron 15, Ohio
Attn: R. R. Fisher

Grumman Aircraft Engineering
 Corporation
Bethpage, Long Island, New York
Attn: Research Department

Hiller Aircraft Corp.
Palo Alto, California
Attn: S. S. Sherby

Hydronautics Inc.
Pindell School Road
Laurel, Maryland
Attn: P. Eisenberg

Lockheed Aircraft Corporation
Burbank, California
Attn: L. A. Rodert